T.R.
SAKARYA UNIVERSITY
GRADUATE SCHOOL OF NATURAL AND APPLIED SCIENCES

THEORETICAL INVESTIGATION OF CU BASED INTERMETALLIC COMPOUNDS AT NANOSCALE

PhD THESIS

Marefat FEIZI KHANGHAH

Nanoscience and Nanoengineering Department

APRIL 2025

T.R.
SAKARYA UNIVERSITY
GRADUATE SCHOOL OF NATURAL AND APPLIED SCIENCES

THEORETICAL INVESTIGATION OF CU BASED INTERMETALLIC COMPOUNDS AT NANOSCALE

PhD THESIS

Marefat FEIZI KHANGHAH

Nanoscience and Nanoengineering Department

Thesis Advisor: Prof. Dr. Süleyman Can KURNAZ

APRIL 2025

The thesis work titled “THEORETICAL INVESTIGATION OF CU BASED INTERMETALLIC COMPOUNDS AT NANOSCALE” prepared by Marefat FEIZI KHANGHAH was accepted by the following jury on …./…. /……. by unanimously/majority of votes as a PhD THESIS in Sakarya University Graduate School of Natural and Applied Sciences, Nanoscience and Nanoengineering department.

Thesis Jury

Head of Jury :	**Prof. Dr. Ali ÇORUH** Sakarya University
Jury Member :	**Prof. Dr. Süleyman Can KURNAZ** (Advisor) Sakarya University
Jury Member :	**Dr. Öğr. Üyesi Hacı Ahmet YILDIRIM** Sakarya University
Jury Member :	**Prof. Dr. Uğur ÖZSARAÇ** Sakarya University Of Applied Sciences
Jury Member :	**Prof. Dr. Ahmet ATASOY** Sakarya University Of Applied Sciences

STATEMENT OF COMPLIANCE WITH THE ETHICAL PRINCIPLES AND RULES

I declare that the thesis work titled " THEORETICAL INVESTIGATION OF CU BASED INTERMETALLIC COMPOUNDS AT NANOSCALE", which I have prepared in accordance with Sakarya University Graduate School of Natural and Applied Sciences regulations and Higher Education Institutions Scientific Research and Publication Ethics Directive, belongs to me, is an original work, I have acted in accordance with the regulations and directives mentioned above at all stages of my study, I did not get the innovations and results contained in the thesis from anywhere else, I duly cited the references for the works I used in my thesis, I did not submit this thesis to another scientific committee for academic purposes and to obtain a title, in accordance with the articles 9/2 and 22/2 of the Sakarya University Graduate Education and Training Regulation published in the Official Gazette dated 20.04.2016, a report was received in accordance with the criteria determined by the graduate school using the plagiarism software program to which Sakarya University is a subscriber, I have received an ethics committee approval document (if ethics approval is not required, this sentence is removed from the text), I accept all kinds of legal responsibility that may arise in case of a situation contrary to this statement.

(18/04/2025)

(signature)

Marefat FEIZI KHANGHAH

To my beloved wife and lovley children

ACKNOWLEDGMENTS

I would like to express my endless gratitude to my valuable advisor Prof. Dr. Süleyman Can KURNAZ, who helped and guided me in determining, conducting and finalizing this thesis topic; to the members of the jury, Prof. Dr. Ali ÇORUH and especially to my valuable teacher Assoc. Prof. Hacı Ahmet YILDIRIM.

I would like to express my profound thanks to the Nanoscience and Nanoengineering faculty members, all my department friends and finally my family for their generosity in providing me with information throughout my PhD.

I would like to extend my sincerest appreciation to Prof. Dr. Yusuf ATALAY and Prof. Dr. Ömer TAMER for their insightful and valuable contributions during the preparation and refinement of this thesis.

I would like to thank my friend, Dr. Ahmet Sefa ATALAY, for his endless help in preparing my thesis.

Marefat FEIZI KHANGHAH

TABLE OF CONTENTS

Page

ABBREVIATIONS

BCC : Body-Centered Cubic
BFGS : Broyden–Fletcher–Goldfarb–Shanno (optimization algorithm)
BZ : Brillouin Zone
CASTEP : Cambidge Serial Total Energy Package
DFT : Density Functional Theory
DOS : Density of States
EOS : Equation of State (e.g., Birch-Murnaghan EOS)
FCC : Face Centered Cubic
GGA : Generalized Gradient Approximation
HM : Half-Metallic (property in Heusler alloys)
IMCs : Intermetallic Compounds
LDA : Local Density Approximation
MM : Molecular Modeling
PBC : Periodic Boundary Condition
PBE : Perdew, Burke, Ernzerhof
PDOS : Partial Density of States
QM : Quantum Mechanic
SCF : Self-Consistent Field (method in DFT)
Sch.E : Schrödinger Equation (Sch.E)
TDOS : Total Density of States
VRH : Voigt–Reuss–Hill (approximation for elastic moduli)

SYMBOLS

∇^2	: Laplacian operator
A_0	: Lattice Constant at Minimum Energy [Å]
A^U	: Universal Anisotropy Index
B	: Bulk Module [GPa]
B/G	: Pugh's ratio (indicator of ductility/brittleness)
B′	: First derivative of bulk modulus with respect to pressure
B_H	: Hill Bulk Modulus [GPa]
B_V	: Voigt Bulk Modulus [GPa]
C_{ij}	: Elastic Stiffness Constants (Tensor Components) [GPa]
Cp	: Cauchy Pressure [GPa]
E	: Total energy of the system
E	: Modulus of Elasticity (Young's Modulus)
$E_{cut\text{-}off}$	: Plane-wave kinetic energy cutoff
EF	: Fermi Energy Level [eV]
E_{XC}	: Exchange-correlation energy
Fm3m (225)	: Space group notations
G	: Shear Modulus [GPa]
G_H	: Hill Shear Modulus [GPa]
G_R	: Reuss Shear Modulus [GPa]
G_V	: Voigt Shear Modulus [GPa]
h	: Planck's Constant [J·s]
$\hat{H}$	:Total energy operator which is also known as Hamiltonian operator.
$\hbar^2$	: Reduced Planck's constant (*ħ = h/2π*)
H_V	: Vickers hardness [GPa]
$\hat{H}\Psi = E\Psi$	: Time-independent Schrödinger equation
$i\hbar\, \partial\Psi/\partial t = \hat{H}\Psi$	: Time-dependent Schrödinger equation
$L1_2$, $D0_3$, $L2_1$	: Crystal structure types (Cu_3Al variants)
m	: Mass [Unit]
M	: Magnetic Moment [μB] (Bohr magneton)
N(A,B)	: Overlap population in bond A-B

$n \cdot h\nu$: Quantized energy levels (Planck's relation)

P(V) : Presser depended volum changing in Third-order Birch-Murnaghan equation of state (BM3-EOS)

$P_{\mu\nu}(k)$ **:** Density matrix

Pm3m (221) : Space group notations

q : Electron Charge or wave vector [C/1/m]

Q(A) : Mulliken charge of atom A

$S_{\mu\nu}(k)$ **:** Overlap matrix

S_{ij} : Compliance constants

$\hat{T}$: Kinetic energy operator

T : Time (in Time-Dependent Schrödinger Eq.) [s]

$\hat{V}$: Potential energy operator

V_0 : Initial volume

X : Atomic Species / Crystallographic Position

x : Molar Fraction / Stoichiometric Variable

α (↑), β (↓) : Spin states (up and down)

ε : Strain Tensor

ϵ_{xc} : Exchange-correlation energy density

μs : Magnetic moment

ν : Poisson's Ratio

ρ : Density [Unit]

ρ(r) : Electron Density Function [$e^{-}/Å^3$]

ρspin(r) : Spin density

σ : Uniaxial Stress

Ψ : Wave function

Ψ : Wave Function (Schrödinger Equation)

ψi(r) : Kohn-Sham orbitals

Ψ(r,t) : time-dependent wave function.

Ψ_{ele} : Electronic Wave Function

LIST OF TABLES

Page

LIST OF FIGURES

Page

THEORETICAL INVESTIGATION OF CU BASED INTERMETALLIC COMPOUNDS AT NANOSCALE

SUMMARY

Intermetallic compounds (IMCs), including transition metals and p-block metals, exhibit high resistance to oxidation and corrosion, low density, high conductivity, and magnetic polarizability. There is growing interest in intermetallic compounds (IMCs) consisting of transition metals and p-block elements, particularly aluminum (TM-Al IMCs). These alloys exhibit a unique combination of properties that make them well-suited for extreme thermal environments. Notably, they possess a favorable balance of low density and high melting temperatures, which contributes to their structural integrity and thermal stability. This thesis employs the first-principles computational approach grounded in Theory of Density Functional (DFT) to analyze the structural and electronic characteristics, charge density distribution, spin polarizability, and magnetic properties of $Cu_{(3-x)}Mn_xAl$ (x = 0, 1) intermetallic compounds. The study implemented the Perdew, Burke, Ernzerhof (PBE) exchange-correlation functional as part of the Approximation of Generalized Gradient (GGA) framework. The calculation of metallic and conductive nature and structural properties was performed simultaneously for all crystal lattices of $Cu_{(3-x)}Mn_xAl$ ($L1_2$, $D0_3$, and Heusler $L2_1$) with *221-Pm3m, 225-Fm3m* space groups. Notably, the study clarifies the stoichiometric similarity and difference between $L1_2$ and $D0_3$ type structures by presenting a detailed discussion of the $D0_3$ structure and its targeted properties for the first time. The lattice constant values obtained by performing various optimizations shows remarkable consistency with previously reported theoretical and experimental measurements. Density Functional Theory-DFT calculations were utilized to analyze the electronic structurethe electronic structure, including band structure, total density and partial density of states, Major and minor spin state densities, map of charge density distribution, and Mulliken bond population. Additionally, the study investigated the chemical bonding characteristics and mechanical properties of intermetallic compounds (IMCs), such as elastic constants, elastic moduli, Pugh's ratio, elastic anisotropy, Poisson's ratio, and Cauchy pressure. The directional dependence of each mechanical property (young, bulk, shear modulus) and the corresponding mechanical properties were calculated. The electron density distribution and population analysis are consistent and reveal the dominant bonding type in each IMC. Furthermore, a Spin Polarizability analysis has been carried out to demonstrate the magnetic nature of the Cu_2MnAl ($L2_1$) Full Heusler alloy upon the addition of the Mn atom.

CU ESASLI İNTERMETALİK BİLEŞİKLERİN NANO BOYUTLARDA TEORİK OLARAK İNCELENMESİ

ÖZET

Bu çalışmada, $Cu_{(3-x)}Mn_xAl$ (x=0, 1) intermetalik bileşiklerinin yapısal ve elektronik özellikleri, Yoğunluk Fonksiyonel Teorisi (Density Functional Theory, DFT) tabanlı hesaplamalar kullanılarak detaylı bir şekilde incelenmiştir. Çalışmada, Cu bazlı intermetalik bileşiklerin kristal yapılarını ve elektronik özelliklerini anlamak amacıyla Genelleştirilmiş Gradyan Yaklaşımı (Generalized Gradient Approximation, GGA) çerçevesinde Perdew-Burke-Ernzerhof (PBE) değişim-korelasyon fonksiyoneli tercih edilmiştir. Bu yöntem, özellikle metalik sistemlerde doğruluk oranı yüksek sonuçlar vermesi nedeniyle yaygın olarak kullanılmaktadır. Elektronik yapı analizleri kapsamında enerji bant yapısı (band structure), toplam ve kısmi durum yoğunluğu (density of states, DOS) ve yük yoğunluğu dağılım haritaları detaylı olarak incelenmiştir.

Kristal yapı modellemeleri, $Cu_{(3-x)}Mn_xAl$ (x=0, 1) bileşiklerinin farklı atomik düzenlemeleri ve fazlarını göz önünde bulunduracak şekilde $L1_2$, $D0_3$ ve Heusler L21 konfigürasyonları altında gerçekleştirilmiştir. Bu yapılar, 221-*Pm3m* ve 225-*Fm3m* uzay gruplarında analiz edilmiş olup, farklı kristal sistemleri arasındaki temel yapısal farklar karşılaştırılmıştır.

$L1_2$ ve $D0_3$ yapıları arasındaki stokiyometrik benzerlikler ve farklılıklar, bu çalışmada kapsamlı bir şekilde değerlendirilmiş olup, özellikle atomlar arasındaki bağ uzunlukları ve kafes parametreleri arasındaki ilişkiler detaylandırılmıştır. $L2_1$ Heusler yapısının ise manyetik özellikler açısından en baskın yapı olduğu görülmüştür.

Bu bağlamda, Mn elementinin katkısının sistemdeki rolü daha yakından incelenmiş ve manyetik moment değerlerinin belirlenmesinde etkili olduğu gösterilmiştir.

Mekanik özelliklerin analizi, Cu(3-x)MnxAl bileşiklerinin mühendislik malzemesi olarak kullanılabilirliği açısından büyük önem taşımaktadır. Bu amaçla elastik sabitler, elastik modüller ve diğer mekanik parametreler hesaplanmıştır.

Poisson oranı, elastik modüller, Pugh oranı, Cauchy basıncı ve elastik anizotropi parametreleri analiz edilerek bileşiklerin mekanik stabiliteleri hakkında detaylı bilgiler elde edilmiştir. Ayrıca, Young modülü, hacim modülü (bulk modulus) ve kayma modülü (shear modulus) gibi temel mekanik parametrelerin yön bağımlılığı incelenmiş ve bu bileşiklerin farklı yönlerde nasıl mekanik davranışlar sergilediği detaylı olarak değerlendirilmiştir.

Tablolar incelendiğinde, en yüksek sıkıştırılabilirliğin en düşük yığın modülüne sahip olan $L2_1$ bileşiğinde gözlemlendiği belirlenmiştir. En yüksek kayma dayanımı $L1_2$ bileşiğine ait olup, aynı zamanda en büyük sertlik değeri de bu bileşikte kaydedilmiştir. Bu durum, $L1_2$ bileşiğinin en yüksek Young modülüne sahip olmasıyla tutarlıdır.

Poisson oranı açısından değerlendirildiğinde, analiz edilen bileşikler arasında $L1_2$ bileşiği 0.33 değeri ile en yüksek kovalent bağlanma derecesini sergilemektedir. B/G

(Pugh's) oranı incelendiğinde, üç bileşiğin de sünek davranış gösterdiği açıkça görülmektedir. Young modülü ile paralel olarak, en yüksek sertlik değeri $L1_2$ bileşiğinde gözlemlenirken, en düşük sertlik değeri $D0_3$ bileşiğinde kaydedilmiştir. Elde edilen veriler, literatürdeki önceki çalışmalarla uyumlu olup, bu bulgularla desteklenmektedir.

Şekiller incelendiğinde, üç bileşiğin de tüm eksenleri boyunca küresellikten sapmalar sergilediği, dolayısıyla anizotropik özellikler taşıdığı görülmektedir. En belirgin sapma $L2_1$ bileşiğinde gözlemlenirken, en düşük sapma $L1_2$ bileşiğinde kaydedilmiştir. Bu sonuçlar, Evrensel Anizotropi İndeksi değerleriyle doğrudan örtüşmektedir.

Bu çalışma, mekanik ve anizotropik özelliklerin kapsamlı bir şekilde incelenerek bileşiklerin yapısal özellikleriyle ilişkili olarak değerlendirilmesine katkı sağlamaktadır.

DFT hesaplamaları sonucunda, $Cu_{(3-x)}Mn_xAl$ (x=0, 1) bileşiklerinin metalik özellikler sergilediği belirlenmiştir. Bant yapısı analizleri, bu bileşiklerin elektronik iletkenlik özelliklerini destekler nitelikte olup, Fermi seviyesinin üzerinde bulunan enerji seviyelerinde elektron yoğunluğunun belirgin olduğu görülmüştür.

Durum yoğunluğu analizleri, sistemin toplam ve kısmi durum yoğunluğu bileşenleri ile değerlendirilerek, elementler arasındaki elektronik etkileşimlerin detaylı bir şekilde ortaya konmasını sağlamıştır. Mulliken yük popülasyonu ve bağ uzunlukları analizleri, bileşiklerin kimyasal bağ yapılarının belirlenmesinde önemli bir araç olarak kullanılmış ve metal-metal ile metal-metaloid bağlanma türleri hakkında detaylı bilgiler sağlanmıştır. Elde edilen teorik sonuçlar, literatürde rapor edilen deneysel verilerle oldukça yüksek bir uyum göstermektedir.

Mekanik özellikler açısından yapılan analizler, bu bileşiklerin mekanik dayanımı hakkında önemli bulgular ortaya koymuştur. Elastik modüllerin hesaplanması sonucunda, bileşiklerin süneklik veya gevreklik özellikleri açısından belirgin farklar gösterdiği belirlenmiştir. Cauchy basıncı ve Pugh oranı analizleri, $Cu_{(3-x)}Mn_xAl$ (x=0, 1) bileşiklerinin sünek veya gevrek karakterde olup olmadığını belirlemek için kullanılmıştır. Ayrıca, elastik anizotropi parametreleri hesaplanarak bu yapıların farklı yönlerdeki mekanik stabiliteleri karşılaştırılmıştır.

Manyetik özelliklerin analizi, özellikle Cu_2MnAl ($L2_1$) Full Heusler bileşiği üzerinde yoğunlaşmıştır. Manyetik moment analizleri, Mn atomunun sistemdeki varlığının manyetik özellikleri belirlemede kritik bir rol oynadığını göstermektedir.

Manyetik moment değerlerinin belirlenmesi amacıyla Spin Polarizabilite Analizi gerçekleştirilmiş ve Mn atomlarının d-elektronları ile Cu ve Al atomları arasındaki etkileşimlerin manyetik özelliklere nasıl katkıda bulunduğu ortaya konmuştur. Özellikle Mn içeriğinin artışıyla birlikte manyetik moment değerlerinin belirgin şekilde yükseldiği gözlemlenmiştir.

$Cu_{(3-x)}Mn_xAl$ (x=0, 1) intermetalik bileşiklerinin farklı uzay gruplarında var olabilme ihtimali de bu çalışmada incelenmiştir. Cu_3Al bileşiği doğal olarak uzay grubu 221'de daha kolay oluşmasına rağmen, aynı stokiyometrik bileşimi koruyarak daha karmaşık bir yapıya sahip olan uzay grubu 225'te de var olabilir.

Literatürdeki mevcut çalışmaların büyük çoğunluğu uzay grubu 221 üzerine yoğunlaşmıştır. Bunun nedeni, uzay grubu 221'in daha düşük atom numarası gereksinimine sahip olması, daha kompakt bir yapı sergilemesi ve daha düşük oluşum

enerjisine sahip olmasıdır. Bununla birlikte, 225 numaralı uzay grubunun oluşumu daha karmaşık koşullar gerektirdiğinden, literatürde bu yapı üzerine yapılan araştırmalar sınırlı kalmıştır. 225 numaralı uzay grubunun doğal oluşumunu sağlayan veya engelleyen laboratuvar koşullarının belirlenmesi, gelecekteki deneysel çalışmalarda dikkate alınması gereken önemli parametrelerden biridir.

Bu bağlamda, Mn'nin dahil edilmesiyle $L2_1$ tipi bir yapı kazanan Heusler alaşımı Cu_2MnAl'in sentezi ve analizi yapılmıştır. Ancak, gelecekte gerçekleştirilecek deneysel çalışmaların, uzay grubu 225'te D03 yapısına sahip Cu_3Al bileşiğinin doğal oluşumunu desteklemek için laboratuvar koşullarının optimize edilmesine odaklanması gerekmektedir.

Deneysel ürünlerin, teorik hesaplamalarla sistematik olarak karşılaştırılması, elde edilen bulguların güvenilirliğini artıracak ve literatürdeki mevcut teorik öngörüleri doğrulamak açısından önemli bir katkı sağlayacaktır.

Sonuç olarak, bu tez çalışması, $Cu_{(3-x)}Mn_xAl$ (x=0, 1) intermetalikn bileşiklerinin ileri mühendislik uygulamaları için önemli malzeme adayları arasında yer aldığını göstermektedir. Özellikle elektronik ve manyetik özellikleri açısından bu bileşiklerin detaylı olarak analiz edilmesi, gelecekte yapılacak deneysel çalışmalar için önemli bir referans kaynağı oluşturacaktır.

Mn katkısının manyetik ve elektronik özellikler üzerindeki etkisinin daha kapsamlı bir şekilde araştırılması, bu bileşiklerin manyetik depolama, spintronik ve termoelektrik uygulamalarda kullanım potansiyelini ortaya koyacaktır. Ayrıca, kristal yapıların uzay grubu dönüşümlerinin detaylı olarak incelenmesi, bu bileşiklerin sentez süreçlerini optimize etmeye yönelik önemli bilgiler sağlayacaktır.

Bu bağlamda, deneysel ve teorik çalışmaların birlikte yürütülmesi, Cu bazlı intermetalik bileşiklerin mühendislik uygulamalarında daha yaygın olarak kullanılmasına olanak tanıyacaktır.

1. INTRODUCTION

In recent years, there has been a surge in research activities dedicated to the development of novel materials intended for utilization across diverse domains, including advanced electronics, energy storage, and biomedical applications [1].

Over the past two decades, the increasing demand for structural materials capable of withstanding severe oxidizing environments and high operating temperatures has led to extensive research on the feasibility of intermetallic compounds (IMCs) [1].

Driven by their unique material behaviors, intermetallic compounds (IMCs) have garnered substantial scientific interest across multiple disciplines. Their high modulus, resistance to environmental degradation, and anomalous strengthening behavior have been extensively documented [2], [3], [4], [5]. Within this class of materials, transition metal-aluminum (TM-Al) IMCs are of particular relevance for high-temperature applications. The combination of low density, high melting points, and enhanced elevated-temperature strength inherent in these alloys makes them highly attractive for structural components operating in extreme thermal environments [6], [7].

The compounds including transition metals and p-block metals, e.g. Aluminum, have garnered attention due to their relatively low density, high resistance to oxidation and corrosion, high melting points, elevated temperature strength, and high conductivity, making them suitable candidates for high-temperature structural applications [8], [9].

The utilization of intermetallic compounds, specifically those formed between Transition Metals and Aluminum (TM-Al), is increasingly recognized as a promising avenue for high-temperature structural applications. The intrinsic properties of these alloys, including a favorable balance of low density and high melting points, contribute to their suitability in extreme thermal environments [10] . Moreover, these compounds exhibit enhanced elevated-temperature strength, coupled with notable resistance to corrosive and oxidative degradation, and significant electrical conductivity, thereby solidifying their potential as viable candidates for demanding high-temperature applications [5]. As a result, intermetallic compounds formed between transition

metals and aluminum (TM-Al IMCs) play a crucial role in advancing materials tailored for these specialized applications.

Among these compounds, Cu-Al [11], with different structure types, has been widely investigated. Cu-Al–based intermetallic compounds (IMCs) are widely applied across multiple industries, such as the electrical sector, semiconductors, light, aircraft, machinery manufacturing, and construction, owing to their exceptional mechanical strength and reduced density in comparison to pure aluminum and pure copper, these alloys offer significant advantages [12]. In addition, these alloys demonstrate a range of advantageous elastic, electronic, and structural properties, including excellent ductility, high tensile strength, thermal stability, and superior resistance to corrosion [13]. The chemical, electronic, and atomic information of Copper and Manganese, two of the Transition Metals, and Aluminium, one of the elements called P-Block or post-transition metals, are shown in **Figure 1.1**, **Figure 1.2**, and **Figure 1.3** respectively.

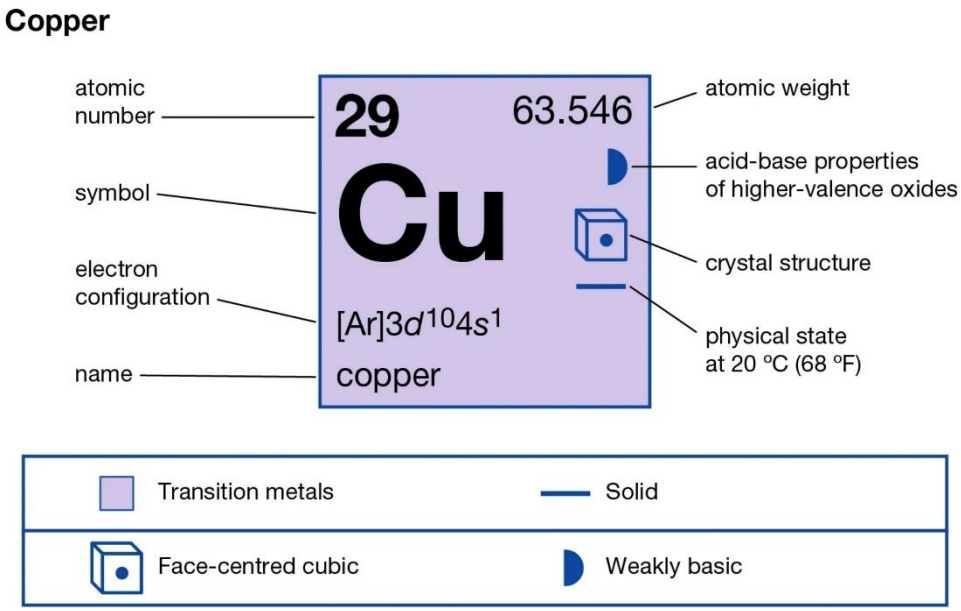

Figure 1.1. Properties of Copper [14].

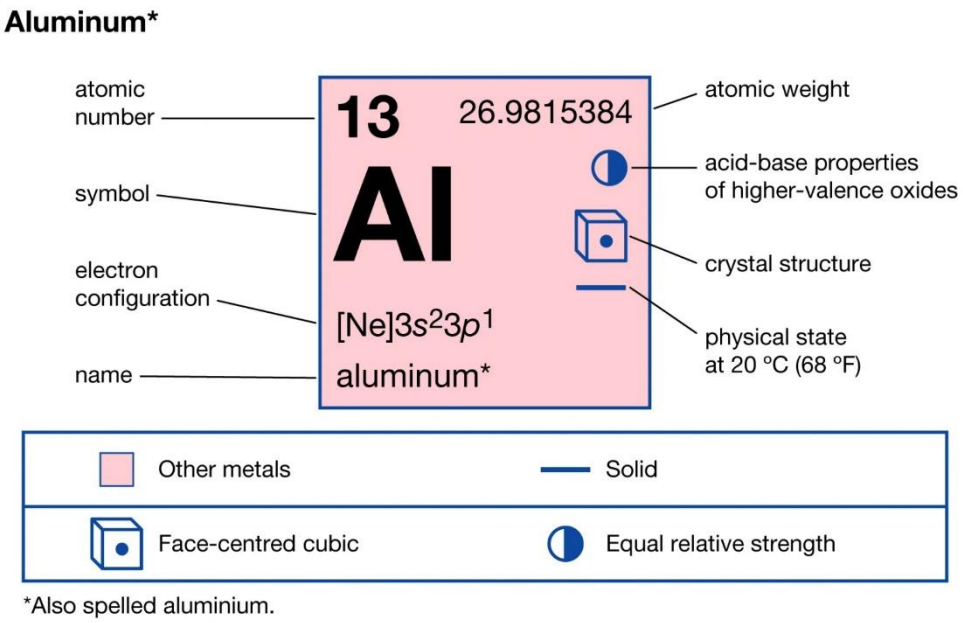

Figure 1.2. Properties of Aluminium [14].

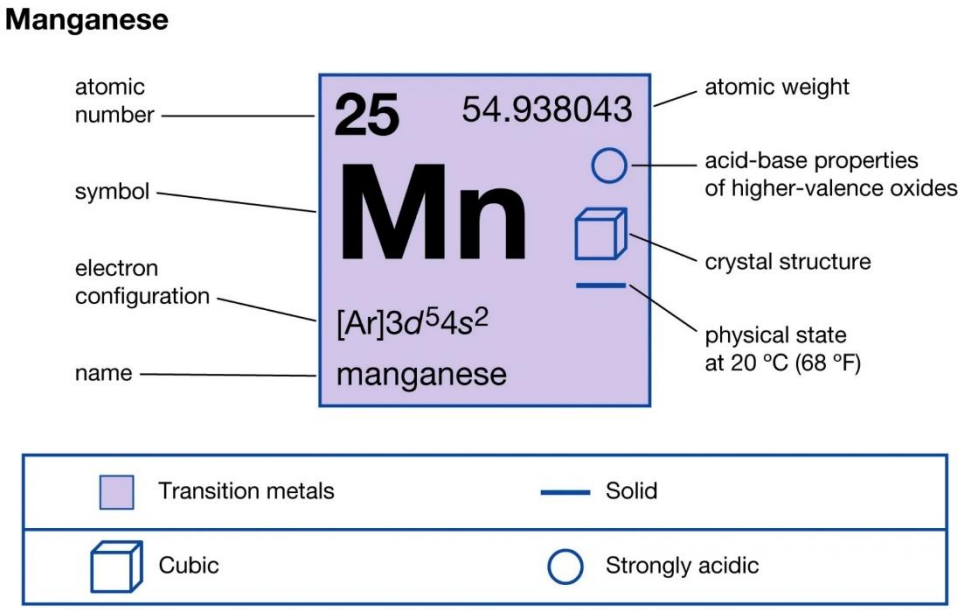

Figure 1.3. Properties of Manganese [14].

Cu-Al–based alloys possess various stable configurations, in particular Cu_3Al with $L1_2$ (*221-Pm3m)* and $D0_3$ (*225-Fm3m)* type structures [15], [16], [17] as well as the Cu_2MnAl ternary Heusler alloy [18], [19] with $L2_1$ type structure. Notably, the Heusler $L2_1$ type structure is partly different from the $D0_3$, despite both of them ($D0_3$ and $L2_1$) belonging to the cf16 Pearson symbol, and sharing the same space group No. of *225-Fm3m.* The $L2_1$ features one additional element in the same crystal lattice and can be doped in place of Cu atoms in the unit cell edges in the $D0_3$ structure type. Doping of

binary Cu–Al alloys with Mn reduces the decomposition speed of solid solution under aging and alters the mechanical and physical characteristics of the material [20]. Cu_2MnAl is also classified as a notable Heusler alloys [18].

Heusler alloys are three-component intermetallic compounds composed of distinct elemental constituents with conventional composition XYZ (Half-Heusler) and X_2YZ (Full-Heusler). Since their discovery a century ago, they have attracted significant interest [18], [21], mainly due to their versatile magnetic properties. The unique properties of ferromagnetic Heusler alloys have sparked a significant increase in scientific interest, driven by their potential applications in various technical fields. For instance, the development of spintronic materials relies heavily on ferromagnetic Heusler alloys with full spin polarization at the Fermi level [22], [23], [24], [25], [26], [27]. Figure 1 presents the periodic table highlighting the elements that constitute the full-Heusler alloys.

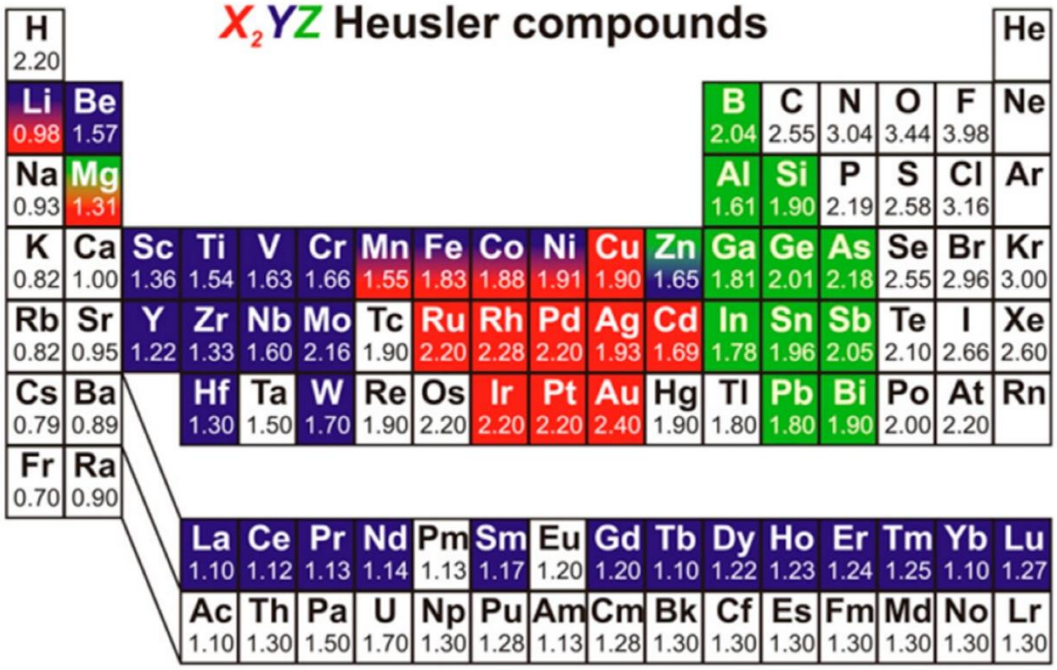

Figure 1.4. The periodic table highlights the diversity of Heusler materials achievable through various elemental combinations (adapted from Ref [28]).

First-principles computations based on density functional theory (DFT) have in recent years become a significant tool for the accurately studying the mechanical properties and crystalline and electronic structures of solids [29]. Hence, the structural and electronic as well as spin polarizability properties of Cu-Al IMCs and their structural study with space group of *221-Pm3m* ($L1_2$) for the Cu_3Al IMCs have recently been

investigated systemically [1], [16], [30], [31], [32]. Complementing these experimental approaches, Zhou et al. [33] utilized first-principles calculations to examine the electronic, structural, and elastic properties of a range of Al-Cu ICs, including Al_2Cu, I4/*mcm*; Al_3Cu_2, *P-3m1*; AlCu, *I12*/*m1*; $AlCu_3$, *Pm-3m*. Employing first-principles calculations, Yang et al. [34] conducted a comprehensive investigation into the interplay between mechanical behavior and electronic structures within a series of Al-Cu intermetallic compounds, specifically Al_2Cu, *I4*/*mcm*; Al_3Cu_2, *P-3m1*; $AlCu_3$, *Pm-3m*. Using a first-principles method, R. Parvin et al. theoretically investigated the band structure of Cu_3Al IMCs. However, studies on electronic and spin polarizability properties, particularly for the other structure types of Cu_3Al IMCs with *225-Fm3m* ($D0_3$) are still very limited due to computational complexities and testing method limitations.

1.1. $Cu_{(3-x)}Mn_xAl$ (x = 0, 1) IMCs

As mentioned before $Cu_{(3-x)}Mn_xAl$ (x = 0, 1) IMCs for x = 0 crystallize into two cubic Cu_3Au (Cu_3Al compound) prototype structures, referred to as $L1_2$ and $D0_3$ [15], [16], [17]. The first type structure of Cu_3Al is $L1_2$ with space group No. 221 (*Pm-3m*), consisting of Al atoms at the corners and Cu atoms at the face centers of the cube, and can be defined by Wyckoff positions: Al @ 1a (0, 0, 0) and Cu @ 3c (0, 1/2, 1/2). The second structure, $D0_3$, has a space group of No. 225 (*Fm-3m*) and consists of Aluminium atoms at the corners and Cu atoms at the edges of the cube and inside the cell, which can be defined by Wyckoff positions: Al @ 4a (0, 0, 0), Cu @ 4b (1/2, 1/2, 1/2) & 8c (1/4, 1/4, 1/4).

The ternary ordered Cu_2MnAl (For x = 1) Heusler alloy (space group No. 225: Fm-3m), in which Al atoms are located in the 4a Wyckoff positions (0,0,0), Cu atoms occupy the 8c site (1/4,1/4,1/4) and Mn atoms occupy the 4b site (1/2,1/2,1/2). From a structural point of view, the Heusler family can be categorized into two types: Full-Heusler X_2YZ phases where X and Y belong to the transition metal elements and Z is the main group s-p element (p-block) [21], [35]. This type structures typically crystallize in the Cu_2MnAl ($L2_1$) type structure, and the Half-Heusler XYZ phases with $C1_b$ structure. In Full-Heusler alloys, the Cu_2MnAl-type is obtained when the X atom is more electronegative than Y, and the Hg_2CuTi-type is obtained when the valance electron of Y atom is larger than X. To date, numerous Ti_2, Sc_2, and Mn_2 - Heusler

alloys with the Hg_2CuTi structure have been reported to exhibit Half-metallic (HM) magnetic behavior or even spin gapless semiconductor properties [36]. The cubic phase atomic occupancies of all $Cu_{(3-x)}Mn_xAl$ (x = 0, 1) IMCs with $L1_2$, $D0_3$, and Heusler $L2_1$ type structures are illustrated in **Figure 1.5** (a), (b), and (c), respectively.

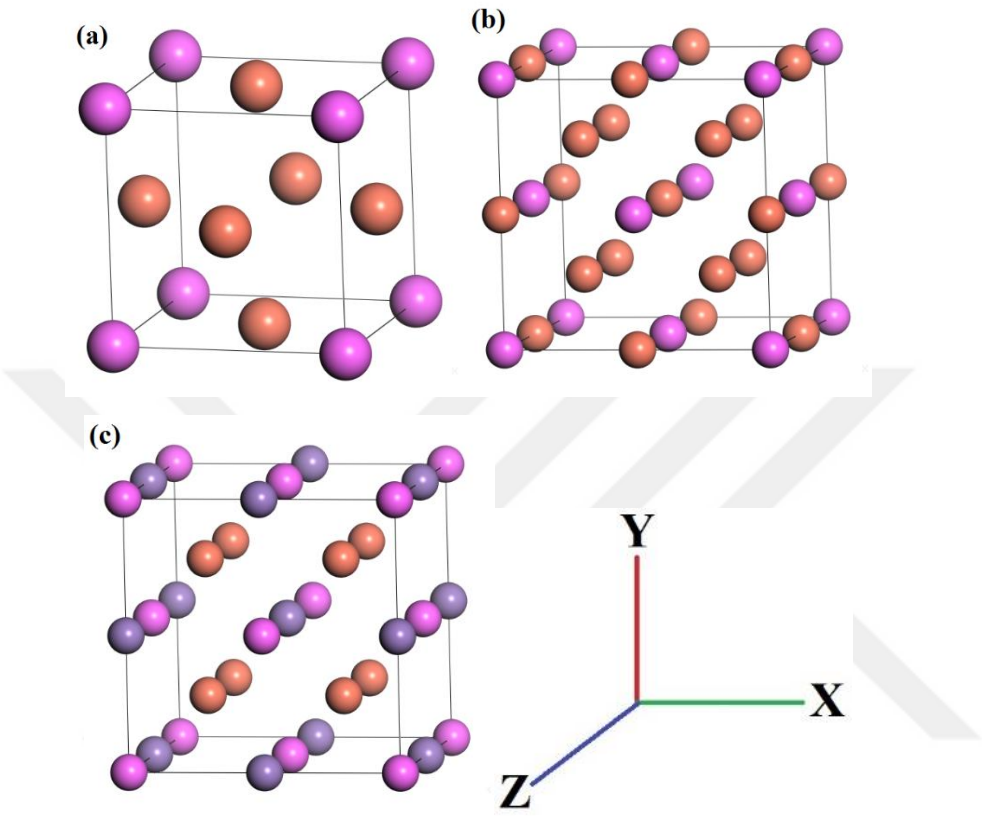

Figure 1.5. The cubic phase atomic occupancies of the all $Cu_{(3-x)}Mn_xAl$ (x = 0, 1) IMCs with $L1_2$ (a), $D0_3$ (b), and Heusler $L2_1$ (c) type structures. Lilac colors are representative of Al atoms and orange ones represent Cu atoms.

1.2. Scope of the Thesis

A review of the literature reveals a limited number of studies have simultaneously reported on different space groups and structure types of Cu_3Al IMCs, as well as Cu_2MnAl ternary Heusler [37], [38], [39], while the theoretical modeling of these studies has been largely overlooked [11], [16], [40]. To the best of our knowledge, only a limited number of studies have been conducted to simulate the optimized geometry and calculate the structural, electronic, and spin polarizability behavior, specifically for the $D0_3$ and $L2_1$ structure types of Cu_3Al intermetallic compounds, relative to other structure types [16], [40]. The studies in question have also focused on a separate set of properties than those focused on in the present thesis.

In this thesis, we present a theoretical model based on first-principales calculations in the frame of Density Functional Theory (DFT) [41], [42] using the CASTEP code [43], to study structural, electronic, and polarizability of different phases ($L1_2$, $D0_3$, and Heusler $L2_1$), of Cu_3Al IMCs compounds. The findings demonstrate an agreement between experimental and other theoretical results.

The subsequent sections of this thesis are structured as follows: Section 3 outlines the computational methodologies employed in this study. Section 4 delves into the results and discussion, encompassing its respective subsections. Lastly, Section 5 encapsulates the key conclusions derived from the research findings.

The organization of this thesis is as follows: Chapter 2 explores the theoretical foundation and surveys the pertinent literature. Chapter 3 provides a comprehensive account of the computational methodologies and parameter selections. Chapter 4 presents and analyzes the findings related to structural, electronic, mechanical, and magnetic properties, respectively. Chapter 5 summarizes the key findings and compares them with existing literature and concludes the thesis and proposes directions for future research. This work builds upon existing research on Cu-based IMCs [12], [17], [33], [37], [38], [44], [45], [46], [47], [48], [49], [50], [51], [52], [53] and expands the understanding of these materials at the nanoscale. The findings are anticipated to play a crucial role in advancing the design and development of novel nanomaterials with enhanced properties for various technological applications.

1.3. Purpose of Thesis

This doctoral thesis aims to conduct a comprehensive theoretical investigation of Cu-based intermetallic compounds for all crystal lattices of $Cu_{(3-x)}Mn_xAl$ ($L1_2$, $D0_3$, and Heusler $L2_1$) with *221-Pm3m*, *225-Fm3m* space groups at the nanoscale using DFT-based first-principles calculations. The primary objective of this study is to explore the structural, electronic, mechanical, and magnetic properties of these intermetallic compounds (IMCs) at the nanoscale. The specific objectives of the research are as follows:

1. Determining the equilibrium crystal structures of selected Cu-based IMCs at various sizes and shapes.

2. Calculating and analyzing the electronic band structures and density of states (TDOS/PDOS) of these IMCs at nanoscale.
3. Investigating the magnetic properties (magnetic moments, spin polarizability) of the nanoscale Cu-based IMCs.
4. Elucidating the influence of nanoscale effects (surface energy, quantum confinement, size dependence) on the overall properties.
5. Comparing theoretical findings with experimental data and previous theoretical studies.
6. Exploring the potential applications of these nanomaterials based on the calculated properties.

Also, one can find the following highlights in these:

- $Cu_{(3-x)}Mn_xAl$ (x = 0, 1) intermetallic compounds have been modelled using first-principles based on density functional theory (DFT).
- All computations were performed utilizing the pseudo-potential technique as implemented in CASTEP (Cambridge Serial Total Energy Package).
- The Geometric optimization & Structural properties, Electronic Band Structure & DOS, Charge Density Distribution & Population Analysis, Spin Polarizability & Magnetic Behavior of the title compounds were explored using DFT/ GGA/- PBE method.
- Physical properties of the $Cu_{(3-x)}Mn_xAl$ (x = 0, 1) intermetallic compounds with different type structure: $L1_2$ (*221-Pm3m)* and $D0_3$ (*225-Fm3m)* and also Cu_2MnAl Heusler alloy (Nuber of space group: *225: Fm-3m*) were investigated and analyzed simultaneously for the first time in this study.
- The bonding nature of the title compound were further evaluated through charge density distribution and Mulliken population analysis.
- Spin Polarizability analysis demonstrates the magnetic nature of the Cu_2MnAl ($L2_1$) Heusler alloy upon the addition of the Mn atom.
- Mechanical Properties of all type strtures reveal the anisotrpic nature of compunds"The study examined the mechanical properties of intermetallic

compounds (IMCs), including elastic constants, moduli, Pugh's ratio, and Cauchy pressure.

- Elastic anisotropy and Poisson's ratio were analyzed to assess the structural behavior of IMCs.
- Directional dependence of Young's modulus, bulk modulus, and shear modulus was evaluated through detailed calculations.

2. THE THEORETICAL BASICS AND QUANTUM MECHANICS (QM)

QM is a subset of theoretical chemistry that mathematically describes matter at the microscopic and nano scale [54] . The foundations of quantum theory emerged in the early 20th century when experimental observations revealed that the behavior of atomic and subatomic particles could not be sufficiently described by classical mechanics, originally formulated by Isaac Newton in the 17th century. However, the limitations of classical mechanics became evident only when applied to extremely small-scale systems, such as atoms, nuclei, and electrons, and when dealing with minimal energy exchanges.

Notably, experimental studies on black-body radiation, the photoelectric effect, heat capacities, and atomic and molecular spectra revealed that energy exchanges occur in discrete units rather than continuously. The concept of energy quantization was first proposed in 1900 by German physicist Max Planck, who demonstrated that the energy of an electromagnetic oscillator with frequency ν is confined to integral multiples of hν, where h represents Planck's constant ($h=6.626 \times 10^{-34}\ J{\cdot}s$) and n is a non-negative integer ($E = n{\cdot}h\nu$). This insight established that energy cannot assume arbitrary values but must adhere to specific quantized levels.

A particularly compelling confirmation of energy quantization arose from observations of spectral lines in atomic and molecular spectra. These experiments showed that atoms and molecules absorb and emit radiation only at specific, discrete frequencies, reinforcing the idea that energy levels within these systems are quantized.

Further experimental evidence, including studies on the photoelectric effect and diffraction, demonstrated the dual nature of both matter and light. This "wave-particle duality" suggested that while light exhibits both particle-like and wave-like behaviors, microscopic particles such as electrons also possess wave-like properties. The concept of wave-particle duality was formally introduced in 1924 by physicist Louis de Broglie. His hypothesis was confirmed when experiments demonstrated that electrons could produce diffraction patterns similar to those of light waves when passed through a double slit. Additionally, the photoelectric effect revealed that electromagnetic

radiation could behave as particles (photons), ejecting electrons from metal surfaces when exposed to ultraviolet radiation.

By 1926, quantum mechanics had been firmly established with the formulation of fundamental equations that describe these quantum phenomena.

2.1. The Schrödinger Equation (Sch.E)

The Sch.E builds upon the hypothesis proposed by Louis de Broglie in year of 1924, which describes microscopic particles—such as electrons, protons, and atoms—as possessing wave-like characteristics. Based on this idea, scientists theorized that a wave equation could effectively describe the behavior of these atomic particles.

In 1926, Austrian physicist Erwin Schrödinger formulated a wave equation to mathematically describe systems of electrons and atomic nuclei.

The time-independent Schrödinger equation is mathematically expressed as:

$$\hat{H}\Psi = E\Psi \tag{2-1}$$

Here, the total energy operator is represented by $\hat{H}$ which is also known as Hamiltonian operator. The symbol Ψ denotes the wave function, describing the quantum state of the system, while E signifies the system's total energy.

The Hamiltonian operator itself is composed of two major terms:

1. Kinetic energy operator ($\hat{T}$) – accounts for the kinetic energy contributions from both electrons and atomic nuclei.
2. Potential energy operator ($\hat{V}$) – represents the various electrostatic interactions occurring within the system, including:

- Attractive forces between atomic nuclei and electrons
- Repulsive forces between electrons
- Repulsive interactions between atomic nuclei

Thus, the Schrödinger equation can be rewritten as:

$$(-\hbar^2/2m\ \nabla^2 + \hat{V})\Psi = E\Psi \tag{2-2}$$

where ħ (h-bar) is the reduced-Planck's constant, m represents the particle mass, and ∇^2 is the Laplacian operator describing spatial variations in the wave function.

In cases where the system evolves over time, then the time-dependent Schrödinger equation should be used as follows:

$$i\hbar\, \partial\Psi/\partial t = \hat{H}\Psi \tag{2-3}$$

or equivalently,

$$i\hbar\, \partial\Psi(r,t)/\partial t = \Psi(r,t).\ (-\hbar^2/2m\ \nabla^2 + V(r,t)) \tag{2-4}$$

where $\Psi(r,t)$ denotes the time-dependent wave function.

The wave function Ψ represents the probability distribution associated with locating a particle at a specific position within a given system.

The probability density, which determines the likelihood of the particle's position, is given by Ψ^2.

By solving the Schrödinger equation, we can determine the discrete energy levels in quantum mechanical systems, including atoms and molecules.

The solutions yield discrete energy values, known as eigenvalues, of the Hamiltonian operator $\hat{H}$.

However, a precise analytical solution to the Schrödinger equation can only be obtained for relatively simple systems, such as the hydrogen atom.

For larger, multi-electron systems such as polyatomic molecules, various approximations must be employed to derive meaningful solutions.

2.2. The Approximation of Born-Oppenheimer

In 1927, Max Born and Julius Robert Oppenheimer introduced a crucial simplification for solving the many-body Schrödinger equation. This simplification, termed the Born-Oppenheimer approximation, enables the decoupling of nuclear and electronic motion in quantum mechanical systems, significantly simplifying their analysis [55], [56].

The primary assumption behind this approximation is that atomic nuclei are significantly more massive than electrons. Due to this large difference in mass, nuclei move at much slower speeds compared to electrons. Consequently, from the perspective of electronic motion, the nuclei can be regarded as being stationary. As a result, the wave function describing the electronic state depends solely on the fixed positions of the nuclei.

Applying this approximation simplifies the Hamiltonian operator by removing the kinetic energy contribution of the nuclei (since they are assumed stationary) and treating the nucleus-nucleus repulsion energy as a constant. The total Hamiltonian can subsequently be represented as:

$$\hat{H}_{ele} = \hat{T} + \hat{V}_{ee} + \hat{V}_{ext} \tag{2-5}$$

where:

- $\hat{T}$ signifies the kinetic energy associated with the electrons.
- $\hat{V}_{ee}$ accounts for the repulsive interactions between electrons
- $\hat{V}_{ext}$ describes the attractive potential that arises between electrons and nuclei.

Because the motion of the electrons is now independent of the nuclei, solving the **electronic Schrödinger equation** provides the electronic wave function:

$$\hat{H}_{ele}\, \Psi_{ele} = E_{ele}\, \Psi_{ele} \tag{2-6}$$

This approximation greatly simplifies quantum mechanical calculations and is widely employed in computational chemistry and solid-state physics. By decoupling **electronic** and **nuclear** motions, it enables efficient modeling of molecular structures, reaction mechanisms, and surface interactions.

2.3. DFT (The Density Functional Theory)

Density Functional Theory (DFT) is another widely utilized method for solving the Schrödinger equation in first-principles calculations [56], [57]. This method serves as a powerful ab initio computational tool in quantum chemistry, used extensively to determine geometric structures and total energy of systems. Compared to other

quantum mechanical methods, such as the **Hartree-Fock method**, DFT is computationally more efficient while maintaining a comparable level of accuracy.

A significant advancement in DFT occurred in 1964, when Hohenberg and Kohn formulated two fundamental theorems that laid its theoretical foundation [58]. These theorems define how electron density governs the total energy and other ground-state properties of a system.

2.3.1.1. First Theorem: Hohenberg-Kohn

The first theorem asserts that the total energy of an electronic system is a unique functional of its electron density. Mathematically, this relationship can be expressed as:

$$E[\rho(x)] = T[\rho(x)] + V[\rho(x)] + E_{xc}[\rho(x)] \tag{2-7}$$

where:

- $T[\rho(x)]$ represents the kinetic energy of a **non-interacting** electron system,
- $V[\rho(x)]$ denotes the **electrostatic energy** from Coulomb interactions,
- $E_{xc}[\rho(x)]$ accounts for **exchange-correlation** effects.

According to this theorem, all ground-state properties, such as the wave function, Hamiltonian, and potential energy, can be expressed as functionals of $\rho(x)$ (the electron density).

2.3.1.2. Second Theorem: Hohenberg-Kohn

This theorem states that the ground-state electron density of a system can be precisely determined through the variational principle. This principle states that for any given trial electron density ρ' satisfying physical constraints:

$$E[\rho'] \geq E_0[\rho_0] \tag{2-8}$$

where $E_0[\rho_0]$ is the actual ground-state energy, and $E[\rho']$ is any trial energy approximation.

This principle is crucial in computational quantum chemistry, as it allows researchers to optimize the **electron density** to find the system's minimum energy configuration.

2.3.2. Kohn-Sham Equation

An advanced method for employing density functional theory (DFT), which received a Nobel Prize, was put forward by Kohn and Sham in 1965 [42]. Their approach introduced the concept of a system consisting of non-interacting particles, which ultimately led to the derivation of a series of single-electron Schrödinger-like equations within an effective potential field:

$$\hat{H}\psi_n = E_n\psi_n \tag{2-9}$$

$$\hat{H} = -\hbar^2/2m\ \nabla^2 + V_{eff} \tag{2-10}$$

Here, ψ_n represents the wave functions corresponding to individual electrons, while V_{eff} signifies an effective potential encompassing three key contributions: the potential due to ionic cores, the Coulombic electron-electron interactions, and the exchange-correlation potential.

The total energy within this framework can be mathematicaly expressed as:

$$E[\rho(r)] = \int Vext(r)\rho(r)dr + F[\rho(r)] = Vext[\rho(r)] + F[\rho(r)] \tag{2-11}$$

where V_{ext} represents the external potential exerted by the nuclei, while $F[\rho]$ denotes the functional describing the total system energy.

Within the Kohn-Sham method, the electronic density is determined as a summation over the squared wave functions of non-interacting electrons:

$$\rho(r)=\sum i\ |\psi_i(r)|^2 \tag{2-12}$$

Where $\psi i(r)$ are commonly referred to as Kohn-Sham orbitals.

The total energy functional, denoted as F, is separated into distinct components as follows

$$F[\rho(r)] = T[\rho(r)] + V_{ee}[\rho(r)] + E_{xc}[\rho(r)] \tag{2-13}$$

where $T[\rho]$ donates the kinetic energy of non-interacting electrons, $V_{ee}[\rho]$ accounts for the electron-electron interactions, and $E_{xc}[\rho]$ encapsulates exchange and correlation effects, including terms not explicitly accounted for in the previous components, such as exchange interactions, electron correlation, kinetic energy corrections, and self-interaction corrections.

Since the explicit formulation of E_{xc} remains unknown, it necessitates approximation. However, its contribution is relatively small in comparison to other energy terms. The subsequent section explores the methods used to approximate the exchange-correlation energy.

2.3.3. The Exchange-Correlation Functional

Various methods have been formulated to approximate the exchange-correlation energy. Among these, **the Local Density Approximation (LDA)** [42] stands out as one of the simplest and most commonly utilized methods.

The Local Density Approximation (LDA) is based on the assumption that the electron density behaves similarly to that of a uniform electron gas.

The functional form of LDA is expressed as:

$$E_{xc}[\rho(r)] = \int \epsilon_{xc}[\rho(r)]\rho(r)dr \tag{2-14}$$

where ϵ_{xc} represents the exchange-correlation energy density, which depends solely on the electron density at a given point. Despite its simplicity, LDA provides relatively accurate results for bulk materials. However, its accuracy diminishes when applied to molecular systems, as the electron density varies significantly in the vicinity of atoms, leading to a dependence of the exchange-correlation energy on the gradient of the electron density.

To address this limitation, the **GGA (Generalized Gradient Approximation)** was developed [56]. This approach incorporates the electron density gradient, improving the accuracy of exchange-correlation calculations:

$$Exc\,[\rho(r)] \;=\; \int\; f[\rho(r), \nabla\rho(r)]\,.\,\rho(r)dr \tag{2-15}$$

Within GGA, several functionals have been proposed, including PW91 by Perdew and Wang [59], PBE by Perdew et al. [60], and RPBE, a refined version of PBE introduced by Hammer et al. [61]. The PW91 functional is particularly suitable for analyzing chemical surface interactions, which is why it has been employed in the present work. The PBE functional, on the other hand, is recommended for studying bulk materials and molecules interacting with metallic surfaces.

2.4. CASTEP Packet and DFT Implementation

In this research, calculations employing the plane-wave pseudopotential method have been conducted using the Cambridge Sequential Total Energy Package (CASTEP) [43]. CASTEP is a commercially available software designed for *ab initio* quantum mechanical computations based on Density Functional Theory (DFT). The simulations are carried out on three-dimensional periodically repeating unit cells, commonly referred to as "supercells," which makes this approach particularly well-suited for analyzing bulk materials and surfaces, aligning with the objectives of this study.

The electronic wave functions are expressed as a series of plane waves, while the influence of core electrons is modeled using an effective potential, known as a pseudopotential. The exchange-correlation component of the total energy is calculated using the local density approximation (LDA) or the generalized gradient approximation (GGA). To determine the ground-state energy, a self-consistent field (SCF) approach is employed to iteratively refine the electron density. Furthermore, to investigate electronic interactions between surfaces and adsorbed molecules, Mulliken charge transfer calculations were performed following the methodology outlined by Segall et al. [62] A detailed explanation of CASTEP's implementation is provided in the subsequent sections.

2.4.1. The Plane-Wave Basis

The plane-wave method, applied to three-dimensional periodic systems in CASTEP, is grounded in Bloch's theorem [63], [64]. This theorem posits that, due to translational symmetry, each electronic wave function can be represented as a product of a periodic component $u_i(r)$ and a plane-wave term $e^{ik \cdot r}$ where k is the wave vector:

$$\psi_i = u_i(r).e^{ik.r} \tag{2-16}$$

The periodic component u_i is represented as a linear combination of plane waves, defined by reciprocal lattice vectors G:

$$u_i(r) = \sum_G C_{i,G} \,.\, e^{iG.r} \tag{2-17}$$

where $C_{i,G}$ are the expansion coefficients, resulting in an electronic wave function composed of plane-wave sums:

$$\psi_i(r) = \sum_G C_{i,k+G} \,.\, e^{i(k+G)r} \tag{2-18}$$

The plane-wave term $e^{(ik\cdot r)}$ represents a wave with wave vector k. Bloch's theorem simplifies the computation of numerous plane waves across an infinite set of k-points[k] by reducing it to a finite set over reciprocal lattice vectors, achieved through k-point sampling (or k-point mesh). This method assumes that wave function variations become negligible for closely spaced k-points, allowing a discrete plane-wave basis set to suffice. This basis set is truncated to include only plane waves with kinetic energies below a specified cutoff:

$$E_{cut-off} = \frac{\hbar^2(G+k)^2}{2m} \tag{2-19}$$

Plane waves with lower kinetic energies contribute more significantly than those with higher energies. In this work, the plane-wave basis set was truncated at 500 eV for IMCs analyses and investigations.

2.4.2. Pseudo-Potential Approximation

The foundation of the pseudopotential method dates back to Harrison's studies in 1966 [65]. This section provides a brief explanation of the pseudopotential method and highlights several important characteristics relevant to this approach [66], [67], [68]. An atom is composed of three fundamental components: the nucleus, valence electrons, and core electrons. Core electrons are strongly bound to the nucleus and

remain largely unaffected by chemical interactions. In contrast, valence electrons are essential for chemical bonding and significantly influence the electronic properties of materials. While core electrons occupy fully filled orbitals near the nucleus, valence electrons are more loosely bound and actively participate in bonding and other electronic processes.

For example, consider a carbon atom with an electronic configuration of $1s^2 2s^2 2p^2$. In a carbon atom, electrons in the $1s^2$ and $2s^2$ orbitals are core electrons [66]. Valence electrons, on the other hand, are positioned farther from the nucleus and move within a field created by the nucleus and core electrons. **Figure 2.1** schematically illustrates a system consisting of the nucleus, core electrons, and valence electrons of an atom.

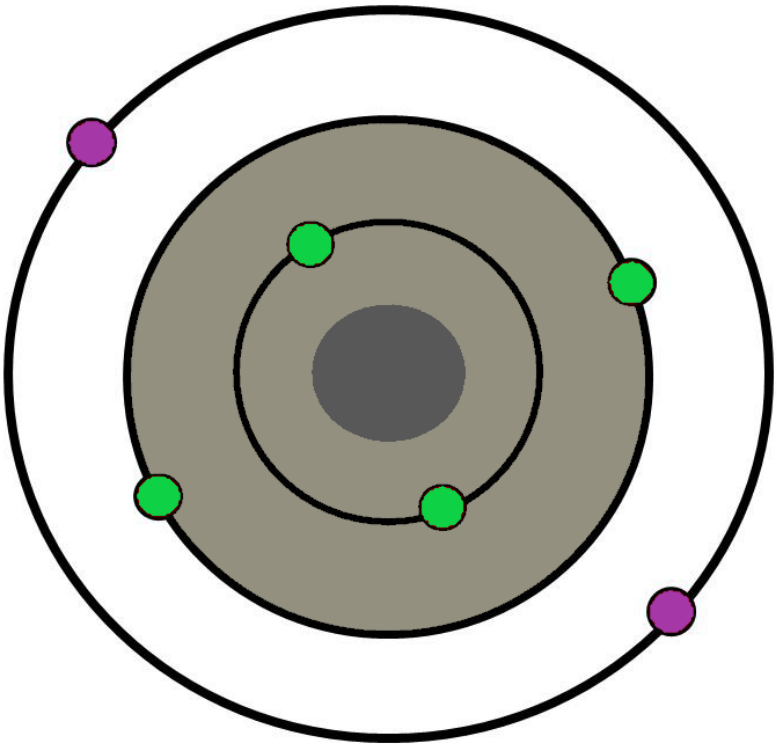

Figure 2.1. An atom composed of a nucleus, core electrons, and valence electrons. The shaded region indicates the core region.

Now, let us consider a system composed of core and valence electrons, schematically represented in Figure 3.2. In such a system, the wave functions of valence electrons are orthogonal to those of core electrons. As mentioned earlier, according to the pseudopotential approach, valence electrons play a role in determining the electronic properties of a crystal, whereas ionic cores do not contribute in any way [89].

The pseudopotential approximation differentiates between valence and core electrons, substituting the ionic potential of the nucleus and core electrons with an effective pseudopotential. This reduces computational demand by focusing calculations on valence electrons, approximating core electrons with a pseudo-wave function, as depicted in **Figure 2.2**. CASTEP implements two pseudopotential types: ultra-soft and norm-conserving. Ultra-soft pseudopotentials, used in this thesis per Vanderbilt's formulation [34], enable calculations at lower cutoff energies (E_cut), while norm-conserving pseudopotentials require higher E_cut values, increasing computational cost. Thus, all calculations herein employed the ultra-soft approach for efficiency.

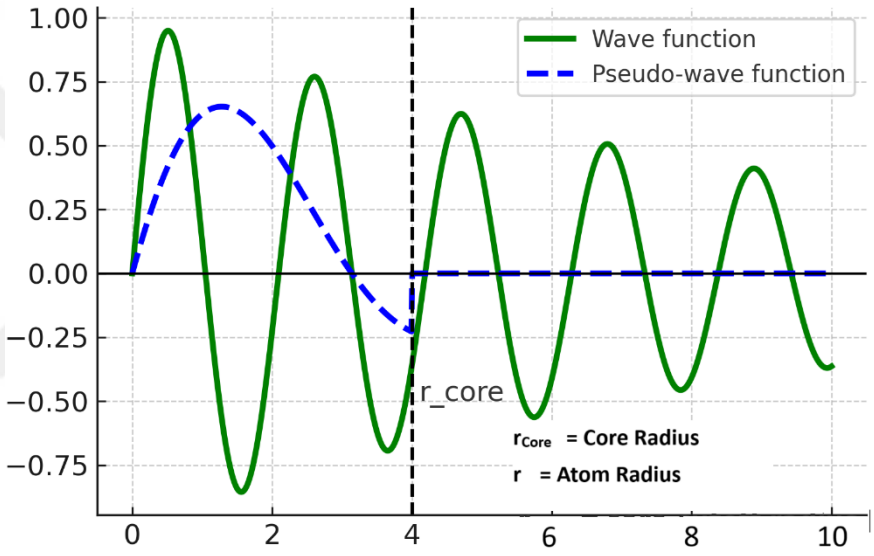

Figure 2.2. The pseudo-potential approximation.

2.4.3. Brillouin-Zone Sampling

Complementing the plane-wave method, Brillouin-zone sampling utilizes a k-point mesh in reciprocal space. Per Bloch's theorem, infinite real-space integrals are replaced by finite integrals over the Brillouin zone. To optimize k-point numbers, CASTEP adopts the Monkhorst-Pack scheme [69], generating a uniform k-point grid in three-dimensional reciprocal space. BZ figure

2.4.4. Mulliken Charge Analysis

The Mulliken charge Brillouin-Zone analysis [70] is among the most widely utilized population analysis methods for determining partial atomic charges in a molecule. This method is particularly useful for evaluating the net electron transfer between a surface

and an adsorbed species, as well as for assessing charge distribution during surface reactions.

Electron density distribution plays a crucial role in understanding surface chemical processes. For instance, in a system where multiple adsorbates coexist, each adsorbate competes for the available charge density of the surface. Consequently, the net electron transfer varies depending on the adsorbate's chemical nature and surface coverage.

Several methodologies have been proposed to partition total electron density into atomic charges. In CASTEP, Mulliken charges are computed using the formalism described by Segall et al. [62].

2.5. Calculation of Magnetic Moment

Electrons exhibit an inherent type of angular momentum called spin, which is defined by their rest mass m_0, charge $q=-e$, orbital angular momentum l, and spin quantum number s. The spin quantum number is directly associated with a magnetic moment μ_s, which interacts with external magnetic fields.

Spin can adopt two orientations: clockwise or counterclockwise, corresponding to values of +1/2 and −1/2, respectively. These states are commonly represented using symbols such as ***α\alpha (↑)*** and ***β\beta (↓)***. Pauli's exclusion principle states that if two electrons occupy the same orbital, they must have opposite spin orientations.

As a result, the total spin in a fully occupied orbital is zero, since the opposing spins effectively cancel each other out.

However, in systems containing unpaired electrons, such as radicals or molecules with an odd number of electrons, the net spin deviates from zero, leading to a nonzero magnetic moment.

To determine the magnetic moment based on spin density, electron charge densities for both spin states ($\rho_\alpha(r)$ and $\rho_\beta(r)$) are computed using a spin-unrestricted version of the Generalized Gradient Approximation (GGSA) functional. The spin density is then evaluated as follows:

$$\rho_{spin}(r)=\rho_\alpha(r)-\rho_\beta(r) \tag{2-20}$$

The total electron density of the supercell is determined by integrating the spin density over all space:

$$\rho_{\ total\ spin} = \int \rho_{spin}(r) dr \tag{2-21}$$

Similarly, the local spin density is obtained by integrating over a specific region:

$$\rho_{\ Local\ spin} = \int |\rho_{spin}(r)| dr \tag{2-22}$$

Local electron spin density serves as an indicator of spin polarization within a given system. If both local and total spin densities are zero, the system is considered non-spin-polarized. A more detailed discussion of spin effects on calculations is provided in **Chapter 4**.

2.6. Calculation of Electronic Properties

The electronic properties of materials are parameters and representations that fully describe the behavior and energy states of the compound's electrons. This encompasses concepts such as electronic energy band structure, partial density of states (PDOS), total density of states (TDOS), and others. The spectrum of energy eigenvalues in a periodic system defines the band structure. Calculating the band structure aids in understanding the shape of the Fermi surface. The electronic and optical properties of a compound can be comprehended by determining the dominant bands near the Fermi level, their energies, and other relevant characteristics. One of the most crucial aspects of the band structure is the band gap, as it significantly influences the electrical and optical properties of a material [71].

The electronic density of states (DOS) of a material is defined as the number of available electronic energy states per unit energy at which electrons can be accommodated.

The electronic density of states (DOS) of a material refers to the number of available electronic energy states per unit energy interval that can be occupied by electrons.

DOS illustrates the distribution of electrons at specific energy levels in a material. It is typically measured experimentally or calculated theoretically to understand the structural and electronic properties of a material. This information is essential for analyzing and predicting the electronic characteristics of a material [72].

Charge density distribution serves as a critical tool in the analysis of chemical bonding. The nature of bonding between various atoms is represented through charge density distribution. Charge density maps assist in visualizing the distribution of electron density around a molecule or an atomic nucleus, as well as the types of bonds formed between different atoms. For instance, covalent bonds are generally characterized by high-density regions that indicate the shared electron density between two atoms. In addition to charge density maps, Mulliken population analysis is also utilized to examine the bonding nature of atoms within a crystal. A positive population value indicates a bonding state, whereas negative values signify an antibonding state [72], [73], [74].

Alloying can often modify or enhance certain properties of a pure metal while generally preserving its fundamental physical characteristics. However, the introduction of foreign atoms may influence electron transport, thereby leading to changes in conductivity and other electronic properties [75].

2.7. Calculation of Mechanic Properties

The elastic constant is a crucial physical quantity used to describe the elasticity of a material in engineering applications. It provides critical information regarding the elastic deformation behavior of a material. The propagation of elastic waves through a medium depends on the elastic constants of that material. Additionally, elastic constants are closely associated with the melting temperature of a solid. Therefore, understanding and predicting the behavior of elastic waves necessitates knowledge of a material's elastic constants.

Elastic constants are directly associated with elastic properties and serve as numerical values used to characterize a material's elastic behavior under different conditions. These constants determine how a material will respond to various stress and strain conditions. The elastic properties, in turn, describe how a material reacts to deformation based on these constants. Consequently, the values of elastic constants define the elastic properties of a material and aid in predicting its mechanical behavior [71], [72], [76], [77].

According to **Hooke's Law**, when a uniaxial stress σ (sigma σ) is applied to an isotropic wire, a longitudinal strain ε\varepsilonε is induced along the direction of the

wire [78]. The relationship between the stress tensor σ_{ij}, the elastic (stiffness) tensor C_{ijkl}, and the strain tensor ε_{kl} is given by Equation (2-23):

$$\sigma_{ij} = C_{ijkl}\varepsilon_{kl} \tag{2-23}$$

Since the elastic tensor is a four-dimensional matrix with three components in each of the four directions, it comprises **3^4=81** components C_{ijkl}. The compliance tensor S_{ijkl}, which is defined as the inverse of the elastic tensor, is calculated using Equation (2-24):

$$\varepsilon ij = S_{ijkl}\,\sigma_{kl} \tag{2-24}$$

According to the symmetry of the system, the number of independent components of Cij decreases. For crystals with a **cubic** structure, there are three elastic constants;

$$C_{ij} = \begin{bmatrix} C_{11} & C_{12} & C_{12} & & & \\ C_{12} & C_{11} & C_{12} & & & \\ C_{12} & C_{12} & C_{11} & & & \\ & & & C_{44} & & \\ & & & & C_{55} & \\ & & & & & C_{66} \end{bmatrix}$$

Therfore;

$$C_{22}=C_{33}=C_{11} \tag{2-25}$$

$$C_{13}=C_{23}=C_{12}$$

$$C_{55}=C_{66}=C_{44}$$

For others $Cij=0$ can be an independent elastic constant.

Therefore, the cubic crystal system possesses the most straightforward form of the elastic matrix, characterized by only three independent elastic constants: C_{11}, C_{12} and C_{44} [79].

$$C_{ij} = \begin{bmatrix} C_{11} & C_{12} & C_{12} & & & \\ C_{12} & C_{12} & C_{12} & & & \\ C_{12} & C_{12} & C_{11} & & & \\ & & & C_{44} & & \\ & & & & C_{44} & \\ & & & & & C_{44} \end{bmatrix}$$

The mechanical stability of a cubic crystal, as dictated by the Born stability criteria, imposes the following constraints on its elastic constants [80], [81] :

$$C_{11} - C_{12} > 0;\ C_{12} > 0;\ C_{44} > 0;\ C_{11} + 2C_{12} > 0. \quad (2\text{-}26)$$

These conditions are both necessary and sufficient for stability. Notably, the first two constraints inherently imply that $C_{11} > 0$, eliminating the need to state it separately, as is sometimes done. Additionally, the first condition can be equivalently expressed as[79] ; $C_{11} > |C_{12}|$.

Furthermore, these stability criteria impose a restriction on the bulk modulus B also known as cubic stability, which must satisfy [82]:

$$C_{12} < B < C_{11} \quad (2\text{-}27)$$

According to the Born stability criterion[80], a stable crystal must be mechanically stable and the elastic constants must be positive. These criteria for all crystal lattices are given in **Table 2.1** [83].

Table 2.1. Born mechanical stability criteria according to all crystal lattices.

Crystal Lattice	Born Mechanical Stability Criteria [80]
Cubic	$C_{11} - C_{12} > 0$; $C_{11} > 0$; $C_{44} > 0$; $C_{11} + 2C_{12} > 0$.
Hexagonal	$C_{11}>0$, $C_{11} – C_{12}> 0$, $C_{44}>0$, &$(C_{11}+C_{12})C_{33}-2C_{12}^2>0$
Tetragonal	$C_{ii}>0$ (i=1, 3, 4, 6), $C_{11}-C_{12}> 0$, $C_{11}–2C_{13}+C_{33}> 0$, $2C_{11}+2C_{12}+4C_{13}+C_{33}>0$
Trigonal (Rhombohedral)	$C_{11}–\|C_{12}\| > 0$, $(C_{11}+C_{12})C_{33}–2C_{13}^2 > 0$, $(C_{11}–C_{12})C_{44} –2C_{14}^2> 0$.
Orthorhombic	$C_{ii}>0$ (i=1–6), $(C_{11}+C_{22}–2C_{12}>0)$, $(C_{11}+C_{33}–2C_{13}> 0)$, $(C_{22}+C_{33}–2C_{23}> 0)$
Monoclinic	$C_{ii}>0$ (i=1–6), $[C_{11}+C_{22}+C_{33}+2(C_{12}+C_{13}+C_{23})]>0$, $(C_{33}C_{55}–C_{35}^2)>0$, $(C_{44}C_{66}–C_{46}^2)>0$, $(C_{22}+C_{33}–2C_{23})>0$.

Materials that provide this stability are mechanically stable.

Elastic (stiffness) constants define the response of a material to applied external forces. Elastic constants are used to define the mechanical properties of solids. The bulk

modulus, Young modulus, shear modulus and Poisson's ratio, which determine the hardness and strength of the material, are calculated from single crystal elastic constants [72].

Figure 2.7 provides a schematic showing the applied stress direction and the measured deformation direction of mechanical properties such as shear modulus, Young's modulus, and Poisson's ratio.

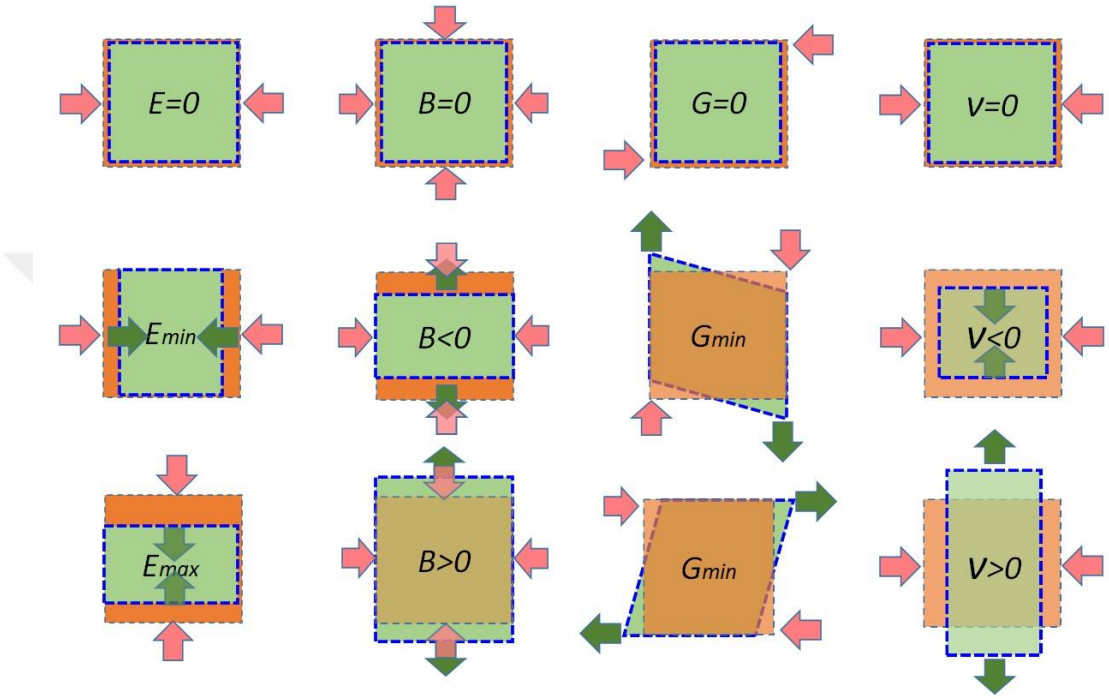

Figure 2.3. A schematic illustration depicting the directional properties of (a) Young's modulus (E), (b) linear compressibility (β), (c) shear modulus (G), and (d) Poisson's ratio (ν). The pink arrows indicate the direction of the applied stress, whereas the green arrows denote the axis along which the resulting strain is measured [84].

The elastic properties of CulAl, including Young's modulus (E), bulk modulus (B), shear modulus (G), Cauchy pressure ($C_{11} - C_{44}$) in units of GPa, and Poisson's ratio (ν), were determined using the Voigt–Reuss–Hill (VRH) approximation method [85]. The Voigt and Reuss models provide theoretical upper and lower bounds for both B and G, where the Voigt approximation defines the maximum and minimum limits, while the Reuss approximation establishes the median and lower boundaries. To achieve a more accurate estimation, Hill proposed calculating the effective bulk and shear moduli as the arithmetic mean of the Voigt and Reuss limits. The VRH averaging method was employed to derive the elastic moduli using the specific formulations applicable to the cubic structure of CuAl IMCs [52].

$$B_V = B_R = (C_{11} + 2C_{12})/3 \quad (2\text{-}28)$$

$$G_R = [5(C_{11} - C_{12})C_{44}] / [4C_{44} + 3(C_{11} - C_{12})] \quad (2\text{-}29)$$

$$G_V = (C_{11} - C_{12} + 3C_{44}) / 5 \quad (2\text{-}30)$$

$$C_p = C_{12} - C_{44} \quad (2\text{-}31)$$

$_V$ and $_R$ denote the moduli determined using the Voigt and Reuss approximations, respectively. The Hill approximation, which provides an effective estimate by averaging the Voigt and Reuss limits, is calculated using the following equations [85], [86]:

$$B_H = (B_V + B_H) / 2 \quad (2\text{-}32)$$

$$G_H = (G_V + G_R) / 2 \quad (2\text{-}33)$$

The bulk modulus (B) quantifies a material's resistance to volumetric deformation under uniform hydrostatic pressure, providing critical insights into its incompressibility, bond strength, and ability to withstand external stress[76], [86]. A schematic view of the bulk modulus is given in Figure 2.9.

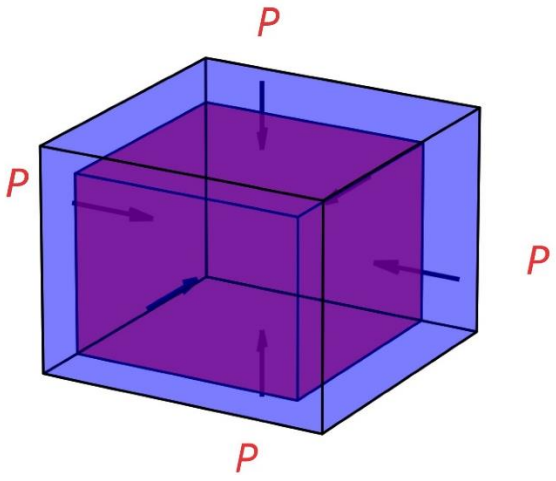

Figure 2.4. Schematic view of the bulk modulus of a system, where P is the applied pressure [71].

The shear modulus shows the deformation resistance of a material against shear stresses caused by extension and bending [87]. The schematic view of the shear modulus is given in **Figure 2.5**.

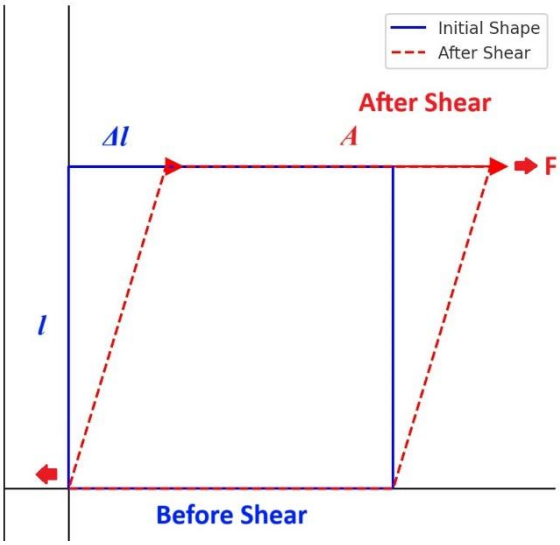

Figure 2.5. In the schematic view of the shear modulus of a body, Δl represents the change in length in the field A exerted by the force F, and l represents the initial height [71].

When a force is applied to a material (for example: pressure), it is called the stress/strain ratio, or known as Young modulus. In other words, Young's modulus (E) represents a material's resistance to uniaxial tension and serves as an indicator of its stiffness. A higher E value corresponds to a greater degree of material rigidity. So the higher the Young modulus of a solid, the lower its deformability [76], [88]. The schematic view of the Young modulus is given in Figure 2.11.

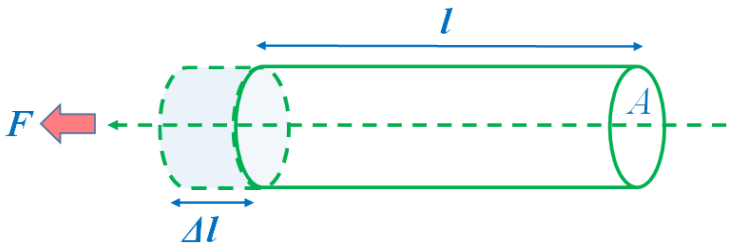

Figure 2.6. Schematic view of the Young modulus of a body, where *l* represents the initial length and *Δl* represents the change in length caused by the force (F) applied on the cross-sectional area (A) [71].

Using B_H and G_H, Young's modulus (E) and Poisson's ratio (ν) of the material can be determined. The corresponding calculation formulas are as follows:

$$E=9B_HG_H / (3B_H +G_H) \tag{2-34}$$

$$v=(3B_H - 2G_H) / [2(3B_H + G_H)] \quad (2\text{-}35)$$

Poisson's ratio (v) represents the ratio of transverse strain to longitudinal strain in a material subjected to uniaxial stress and is closely linked to its internal chemical bonding characteristics.

In general, metal-bonded materials exhibit a Poisson's ratio of approximately 0.3 and above, while covalently bonded materials have a lower value of about 0.1, while metallic bonds have a value of 0.25 [86]. The schematic view of the Poisson ratio is given in **Figure 2.7**.

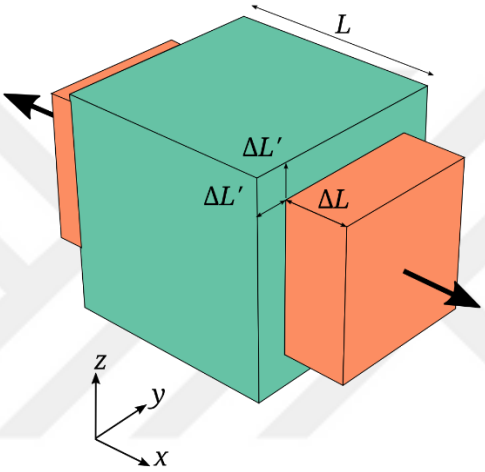

Figure 2.7. A schematic representation of Poisson's ratio in a system:

A cube with side length L made of an isotropic, linearly elastic material is subjected to tensile stress along the x-axis, exhibiting a Poisson's ratio of 0.5. The unstrained state is represented by the green cube, while the red cube illustrates expansion in the x-direction by ΔL due to tension and contraction in the y- and z-directions by $\Delta L'$.

Hardness can be defined as the resistance of engineering materials to plastic deformations such as scratching, wear, and indentation. Theoretically, the Vickers hardness (HV) value is calculated using Equation 3.8 based on the BH and GH values[71]. A higher Vickers hardness value also signifies the presence of stronger covalent bonds.

$$Hv = 2 \times \left(\frac{G_H^3}{B_H^2}\right)^{0.585} - 3 \quad (2\text{-}36)$$

3. MATERIAL AND METHODE (COMPUTATINAL DETAILS)

3.1. Computatinal Details

All calculations were performed utilizing the pseudo-potential technique based on plane-wave density functional theory (DFT) [41], [42] as implemented in **Ca**mbridge **S**erial **T**otal **E**nergy **P**ackage (CASTEP) [43] computer program. The generalized gradient approximation (GGA) in the form of Perdew–Burke–Ernzerhof (PBE) was used as the exchange–correlation potential [60]. This program appraises the total energy of periodically (PBC[1]) repeating geometries within the frame of density-functional theory and the pseudo-potential approximation [41], [42], [89]. The interaction of the valence-core electrons was represented by Vanderbilt-type ultrasoft pseudopotential [90], while the valence electrons are represented explicitly in the calculations; therefore, the potential of the constituent atoms was estimated under the assuming the neutral atomic configurations of $3s^2\ 3p^1$ and $3d^{10}\ 4s^1$ as valence electrons for Al and Cu, respectively. The Monkhorst-Pack scheme was employed to sample the Brillouin zone [69]. The number of k-point grids and cutoff energy were systematically increased until the computed total energy stabilized within the specified tolerance, ensuring a total energy difference of less than 1 meV (total energy difference < 1 meV). After convergence, the optimal k-point grids with mesh parameters 16×16×16 and plane-wave cutoff energy of 500 eV were chosen to obtain equilibrium lattice parameters and calculate the band structure, and the polarizability properties of Cu_3Al intermetallic with space group of 225-Fm3m ($D0_3$). For other Cu_3Al intermetallics belonging to the space group 221-Pm3m ($L1_2$), a k-point grid of 18×18×18 and a plne-wave energy cutoff of 500 eV were utilized. Similarly, for the Heusler alloy ($L2^1$), the electronic wave function was expanded in plane waves up to a cutoff energy of 500 eV, while a 12×12×12 k-point mesh was applied for Brillouin zone sampling.

[1] Periodic Boundary Condition

The structural parameters of Cu_3Al intermetallics were obtained through the Broyden-Fletcher-Goldfarb-Shanno (BFGS) optimization algorithm [91] with the following convergence criteria: energy change per atom below 10^{-5} eV, maximum force below 0.03 eV/ Å, maximum stress below 0.05 GPa, maximum displacement of atoms less than 1.0×10^{-3}Å and self-consistent field tolerance during the geometry optimization fixed to 1.0×10^{-6} eV/atom.

3.2. Methods of Molecular Modeling (MM)

Modeling Methods of Molecular Modeling (MM) are given below.

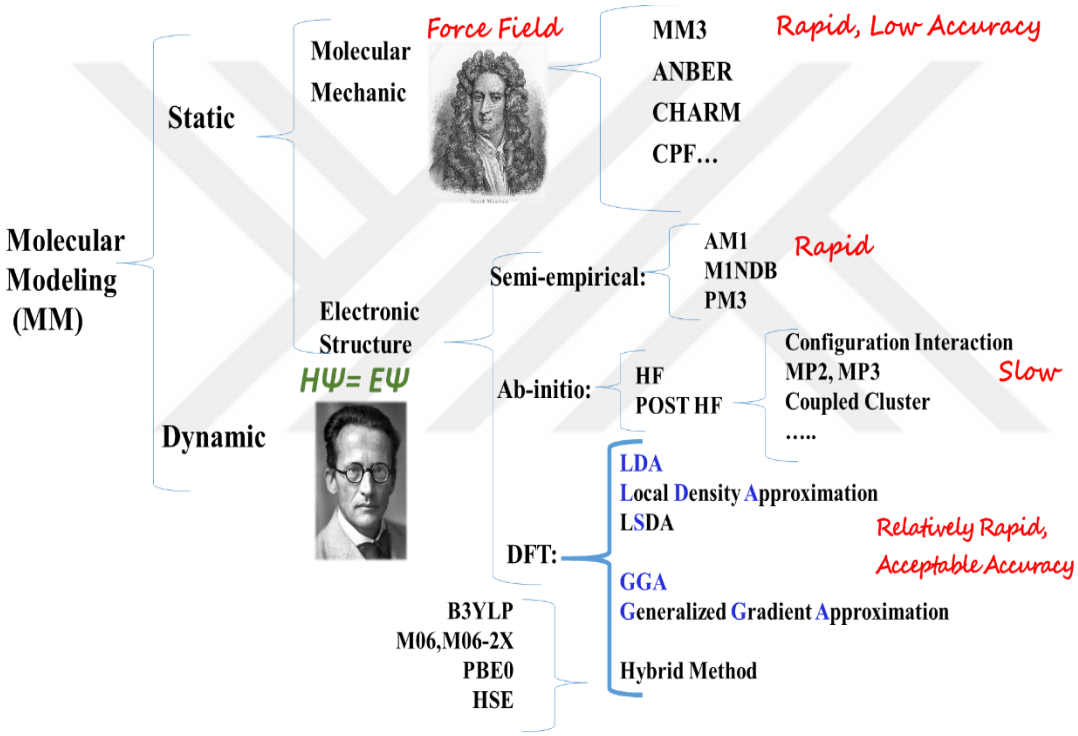

Figure 3.1. Techniques of Molecular Modeling (MM)

In this thesis, we chose the electronic structure method in static molecular modeling and performed the calculations using the DFT technique, which is the fastest and most accurate of the existing methods. Also, in the DFT sub-methods, we employ the Perdew–Burke–Ernzerhof (PBE) exchange-correlation functional, which belongs to the GGA Methods for all investigations.

There exist seven distinct lattice systems, each of which can be categorized into four types of centering: primitive, base-centered, body-centered, and face-centered. However, not all possible combinations of lattice systems and centering types are

unique, as some are equivalent, while others are infeasible due to symmetry constraints. Consequently, the number of unique lattice structures is reduced to 14, known as the Bravais lattices [92].

The classification of these 14 Bravais lattices within the seven lattice systems is summarized in the following figure:

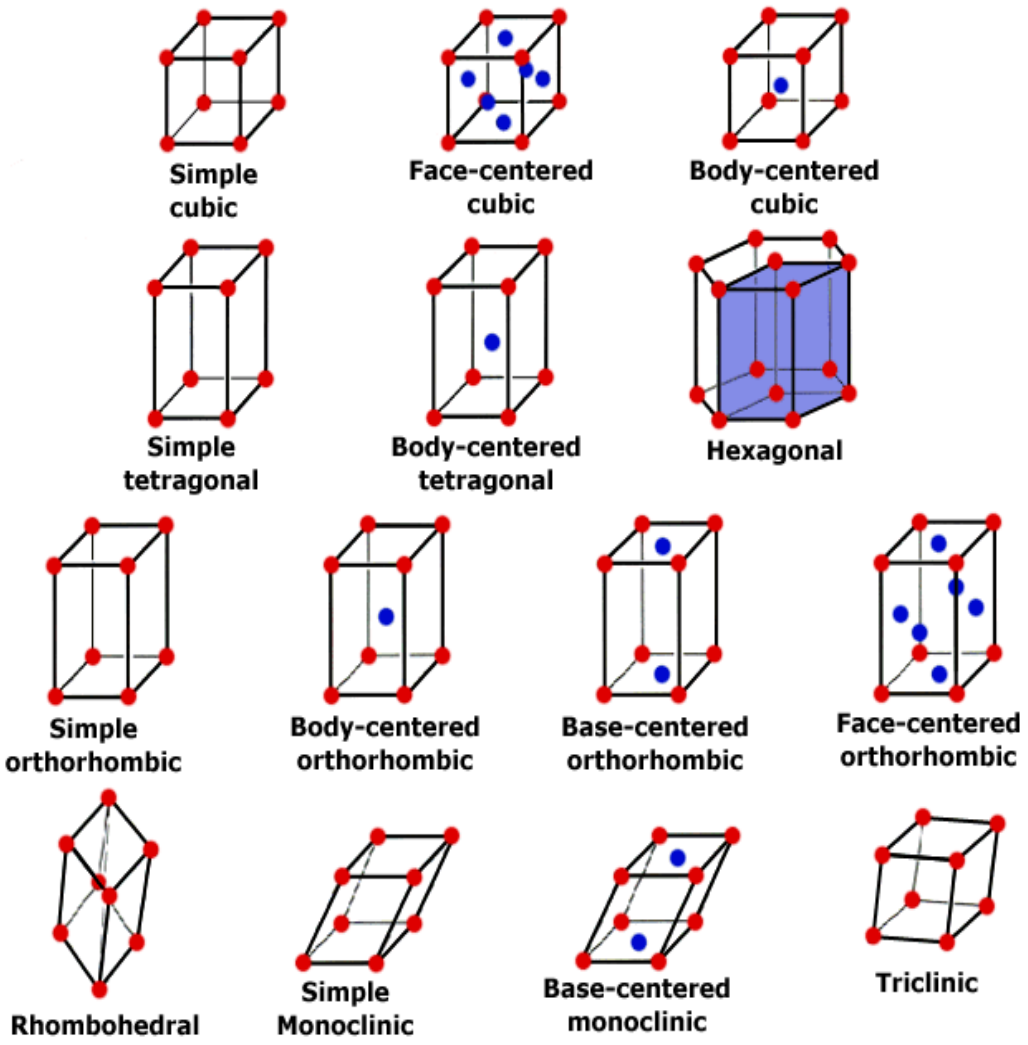

Figure 3.2. Crystal lattice systems.

The crystallographic data of IMCs is shown in **Table 3.1**

Table 3.1. The crystallographic data of $Cu_{(3-x)}Mn_xAl$ (x = 0, 1) IMCs.

Stoichiometry	Crystal system	Space groups (International short symbol)	Pearson symbol	Prototype	SBS	Sp No.
Cu_3Al	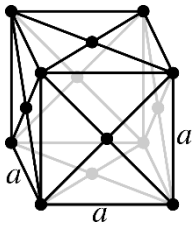	$Pm\bar{3}m$	cP4	$AuCu_3$	$L1_2$	221
Cu_3Al		$Fm\bar{3}m$	cF16	BiF_3	$D0_3$	225
Cu_2MnAl		$Fm\bar{3}m$	cF16	$AlCu_2Mn$ (Heusler)	$L2_1$	225

As shown in **Table 3.1** all of Cu(3-x)MAl (x = 0, 1) IMCs have FCC (Face Centered Cubic) Cubic lattice system. As mentioned in Section 1 Cu_3Al can be formed in two different space groups with the same stoichiometry. These are space groups 221 (with $L1_2$ Type structure) and 225 (with $D0_3$ Type structure). Although the Cu_3Al compound is more easily formed in nature in space group 221, it can also occur in the more complex space group 225 (with $D0_3$ Type structure) while maintaining the same stoichiometry. That is why studies in the literature always focus on space group 221, and space group 225 has rarely been studied or is very rare. The reason why space group 221 is formed more in nature is because the Cu_3Al compound can be formed with less atomic number, more compact and smaller dimensions, and even less formation energy. In addition, after passing to space group 225, different stoichiometries, or rather different phases, can form in the same space group. In this study, the Heusler (Cu_3MnAl) structure, which is a $L2_1$ type structure with the addition of Mn, was investigated.

4. RESULTS AND DISCUSSION

4.1. Geometric Optimization & Structural Properties

The optimal lattice constant is the value at which the total energy is minimized [93], [94]. To determine the stable optimal value and the equilibrium lattice constant, the total energy was computed for various lattice constants. The corresponding results are presented in **Figure 4.1**, **Figure 4.2**, and **Figure 4.3**. The data obtained were fitted with a third-ordered cubic polynomial equation, revealing the minimum energy at a lattice constant of ***a_0=0.3691 nm*** (3.691 Å), ***0.5860 nm*** (5.860 Å), ***0.5955 nm*** (5.955 Å) for $L1_2$, $D0_3$, and Heusler $L2_1$), respectively. As evident from **Table 4.1**, the lattice constant exhibits strong consistency with both previous theoretical predictions and experimental measurements [1], [16], [17], [19], [45], [49], [95], [96], [97].

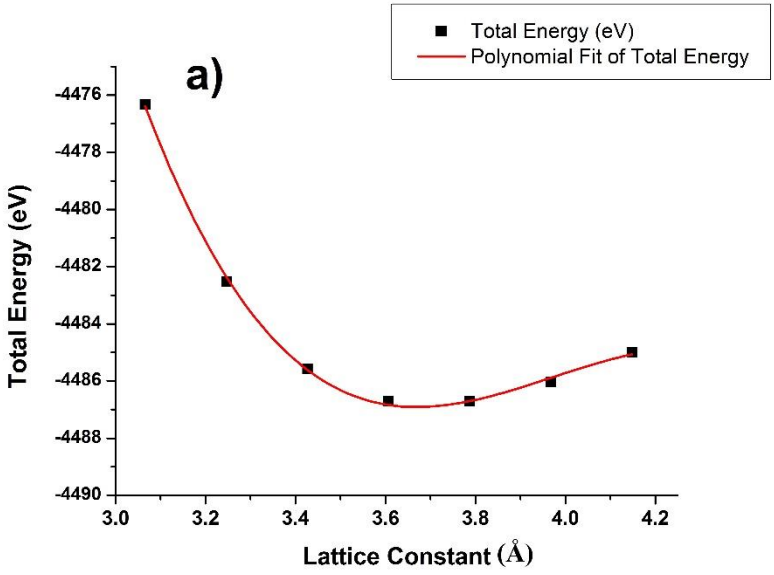

Figure 4.1. The total energy of Cu3Al IMCs with different crystal structures under different lattice constants. (a) $L1_2$ type structure.

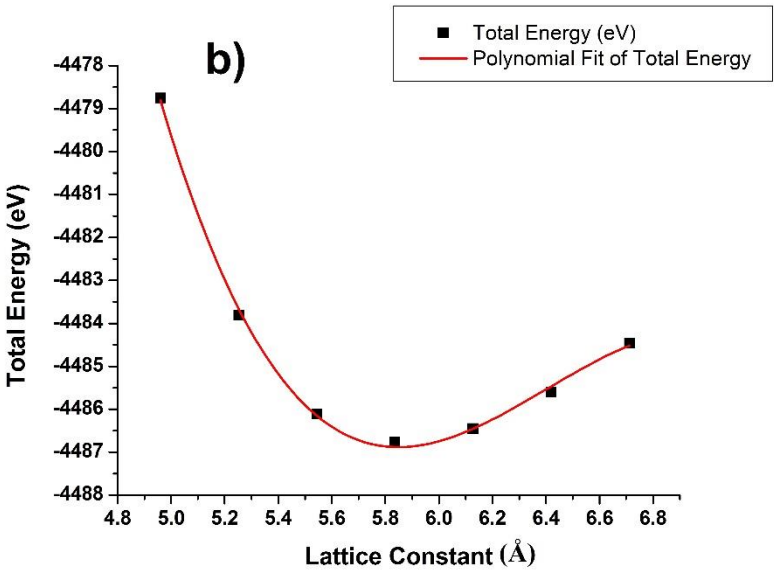

Figure 4.2. The total energy of Cu3Al IMCs with different crystal structures under different lattice constants. (b) $D0_3$ type structure.

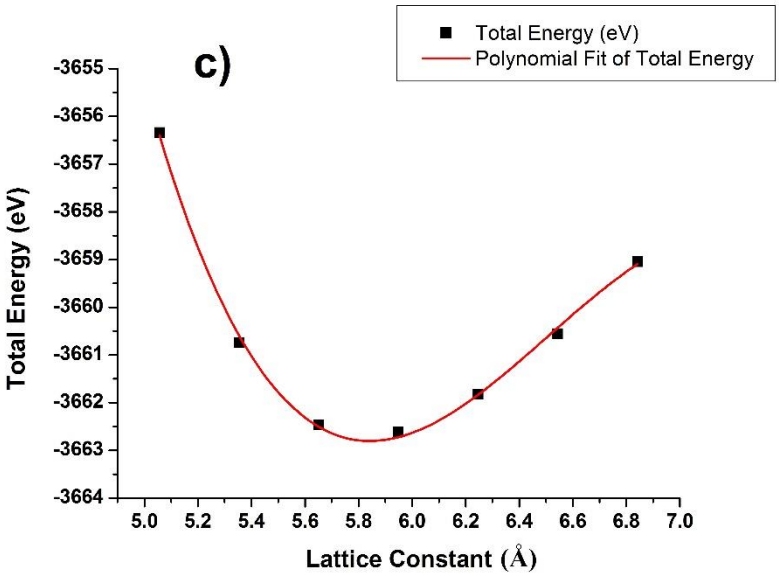

Figure 4.3. The total energy of Cu_3Al IMCs with different crystal structures under different lattice constants. (c) Heusler $L2_1$ type structure.

Furthermore, the volume (lattice parameter^3) at zero pressure, bulk modulus, and the first derivative of bulk modulus were obtained by fitting the *pressure (P)−volume (V)* curve with the results presented in **Table 4.1**. The bulk modulus characterizes a material's ability to resist deformation when subjected to external pressure. For solid materials, the bulk modulus indicates the compressibility of the materials, which is associated with their impact sensitivity [98], [99]. A well-known method for

characterizing the behavior of solid materials under pressure is the third-order Birch-Murnaghan equation of state (BM3-EOS) (formula 1) [83], [100].

$$P(V) = \frac{3B_0}{2}\left[\left(\frac{V}{V_0}\right)^{-7/3} - \left(\frac{V}{V_0}\right)^{-5/3}\right]\left\{1 + \frac{3}{4}(B' - 4)\left[\left(\frac{V}{V_0}\right)^{-2/3}\right] - 1\right\} \quad (4\text{-}1)$$

Here, P represents the pressure, B_0 denotes the bulk modulus, V is the deformed volume, V_0 corresponds to the initial volume, and B' signifies the first derivative of the bulk modulus with respect to pressure.

A comparison of our results reveals reasonable agreement with both theoretical and experimental values. All the values determined in this stage are used in the subsequent calculations to enhance convergence, accelerate computation, and ultimately improve the accuracy of the results.

Table 4.1. Calculated lattice constants including cubic lattice parameter (a), bulk modulus (B), and its pressure derivative (B′) for different crystal structures.

Compound	Type Structure	References	a [Å]	B_0 [GPa]	B′
Al	FCC-A1	**This work**	**4.0488**	**76.672**	**4.590**
		Calc. [16]	4.05	75.937	4.588
		Exp. [49]	4.0496	76.866	-
Cu	FCC-A1	**This work**	**3.641**	**133.521**	**4.881**
		Calc. [16]	3.65	131.82	4.983
		Exp. [49]	3.615	137.8	-
Cu_3Al	$L1_2$	This work (from Cubic fit)	3.669	-	-
		This work (from EOS)	**3.691**	**129.205**	**4.709**
		Calc. [1]	-	130.15	-
		Calc. [16]	3.7	126.72	4.675
		Exp. [17]	3.607	-	-
	$D0_3$	This work (from Cubic fit)	5.849	-	-
		This work (from EOS)	**5.860**	**129.11**	**4.741**
		Calc. [16]	5.877	126.23	4.117
		Exp.	5.83[45]	-	-
		Exp.	5.80[95]	129.6[16]	-
Cu_2MnAl	$L2_1$	This work (from Cubic fit)	5.842	-	-
		This work (from EOS)	**5.955**	**125.654**	**4.048**
		Calc. [96]	5.927	126.689	4.066
		Exp. [19]	5.949	-	-
		Exp. [97]	5.984	-	-

The lattice constant determined for all IMCs in this study exhibits a discrepancy of approximately 2% compared to the experimental value. Furthermore, slight differences are observed between these results and other theoretical values, which can

be attributed to the utilization of different calculation methods. These findings highlight the reliability of our current DFT-based first-principles calculations. The observed discrepancy can be attributed to the fact that the computed data were obtained under simulation conditions at 0 Kelvin, whereas the experimental data are obtained at room temperature, which introduces variations in parameters.

The observed discrepancy can be attributed to the fact that the computed data were obtained under simulation conditions at 0 Kelvin.

4.2. Electronic Band Structure & DOS

The spectrum of energy eigenvalues in a periodic system is referred to as the band structure. Band structure calculations provide valuable insights into the form of the Fermi surface. By analyzing the dominant electronic bands in the vicinity of the Fermi level, their energy status, etc. one can understand the electronic and optical properties of materials. One of the most useful parameters of the band structure is the band gap, which has a profound impact on the optical and electrical properties of the material [72], [101]. The electronic band structure of all $Cu_{(3-x)}Mn_xAl$ (x = 0, 1) type structures along the high symmetry points (X-R-M-G-R) for $L1_2$ and (W-L-G-X-Y-K) for $D0_3$ and Cu_2MnAl ($L2_1$) in the Brillouin zones are shown in **Figure 4.4**. (a), **Figure 4.5** (b) and **Figure 4.6** (c), respectively. The band structure of Cu_3Al IMCs was computed at equilibrium volume (zero pressure, P=0). The Fermi level is set at zero energy value.

Figure 4.4. (a), **Figure 4.5** (b) and **Figure 4.6** (c) reveal the conductive and metallic nature of both Cu_3Al IMCs and Cu_2MnAl due to the overlap of valence and conduction bands at the Fermi level. The band structures of all crystals are reasonably consistent with previous studies. The valence region of $L1_2$ extends from -10.28 eV up to the Fermi level EF = 0 eV, and similar trends are observed for other type structures ($D0_3$, and Heusler $L2_1$). The conduction regions span from the Fermi level EF = 0 eV up to 18.5 eV and 23.2 eV for $L1_2$ and both $D0_3$ and Heusler $L2_1$ type structures.

From **Figure 4.4** (a) and **Figure 4.5** (b) it is evident that $L1_2$ and $D0_3$ type structures exhibit no spin polarizability, as the spin-up (alpha) bands (depicted in blue) coincide with the spin-down (beta) bands (depicted in red), resulting in identical electron paths illustrated on the band structure. In contrast, **Figure 4.4** (c) reveals that for the $L2_1$ type structure, both alpha (up-spin) and beta (down-spin) electrons originating from

Mn atoms follow distinct paths, indicating magnetic and spin polarizability in this structure.

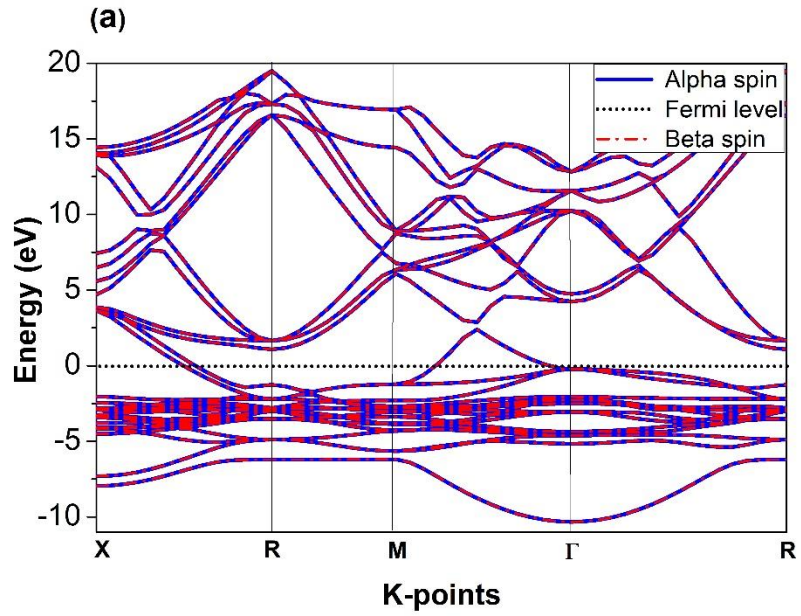

Figure 4.4. The Calculated band structures of (a) $L1_2$ type structure.

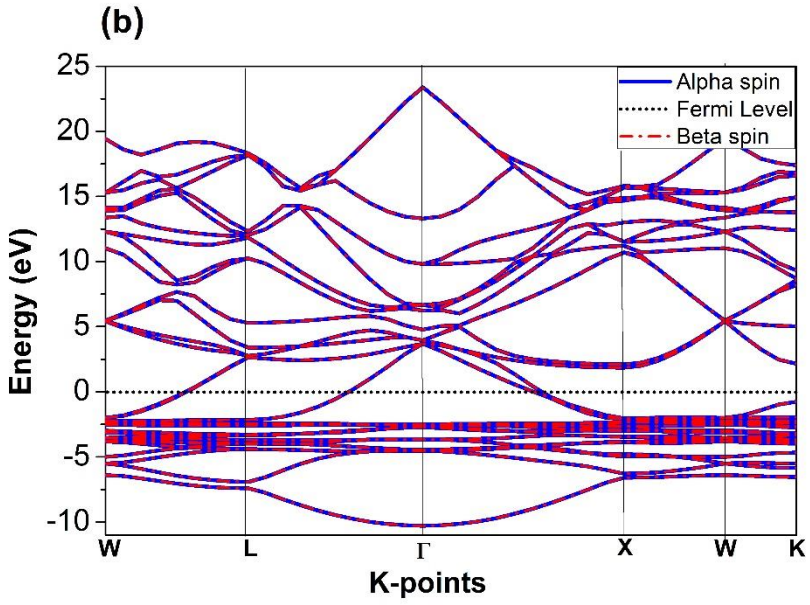

Figure 4.5. The Calculated band structures of (b) $D0_3$ type structure.

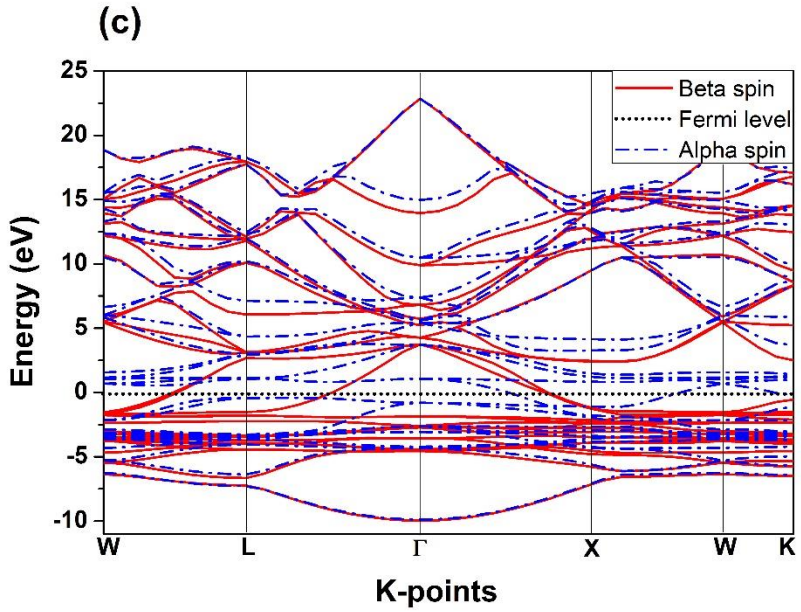

Figure 4.6. The Calculated band structures of (c) and Heusler $L2_1$ type structure.

The density of states (DOS) study provides crucial insights into the physical properties of materials. The total density of states (TDOS) and the partial density of states (PDOS) of Cu, Al, and Mn atoms are depicted in **Figure 4.7** (a), **Figure 4.8**(b), and **Figure 4.9** (c). It is evident that all the type structures of $Cu_{(3-x)}Mn_xAl$ IMCs possess a metallic character, as indicated by the presence of a finite density of states (DOS) at the Fermi level. The fundamental characteristics of these compounds are primarily governed by the d bands of Cu. For $L1_2$, in the range of −11 and 0 eV, the total density of states is predominantly attributed to the Cu-3^d states.

Beyond the Fermi level, the total density of states (TDOS) is predominantly dominated by the Cu-p and Cu-s orbitals, with contributions from the Al-s and Al-p states. Additionally, a significant hybridization is observed between the Al-p, Al-s, Cu-p, and Cu-s states at energies exceeding -2eV and below -5eV. The Cu-d and Al-p states exhibit strong hybridization in the range of −5 to −3 eV. The DOS of the $D0_3$ type structure in **Figure 4.8** (b) is closely resembles that of $L1_2$ (**Figure 4.7** (a)), with the notable difference that the conduction band of $D0_3$, extending up to +17 eV, primarily arises from Al-s and p states. The strong hybridizations are observed near -4 eV and on -2.5 eV arises from Al-p and Cu-d states and arises from Al-s and Cu-p states, respectively. Additionally, beyond the Fermi level, Al and Cu states exhibit collective contributions.

The TDOS and PDOS of $L2_1$ type structure have also been studied as shown in **Figure 4.9** (c). As illustrated in **Figure 4.9** (c), no energy gap is observed around the Fermi level, thereby confirming the metallic nature of the $L2_1$ structure. The undermost valence bands below -6 eV in Cu_2MnAl are entirely attributed to Al-s states, whereas the bands ranging from -5.5 eV to 3 eV are primarily attributed to states of Cu-^{3d} and Mn-^{3d}.

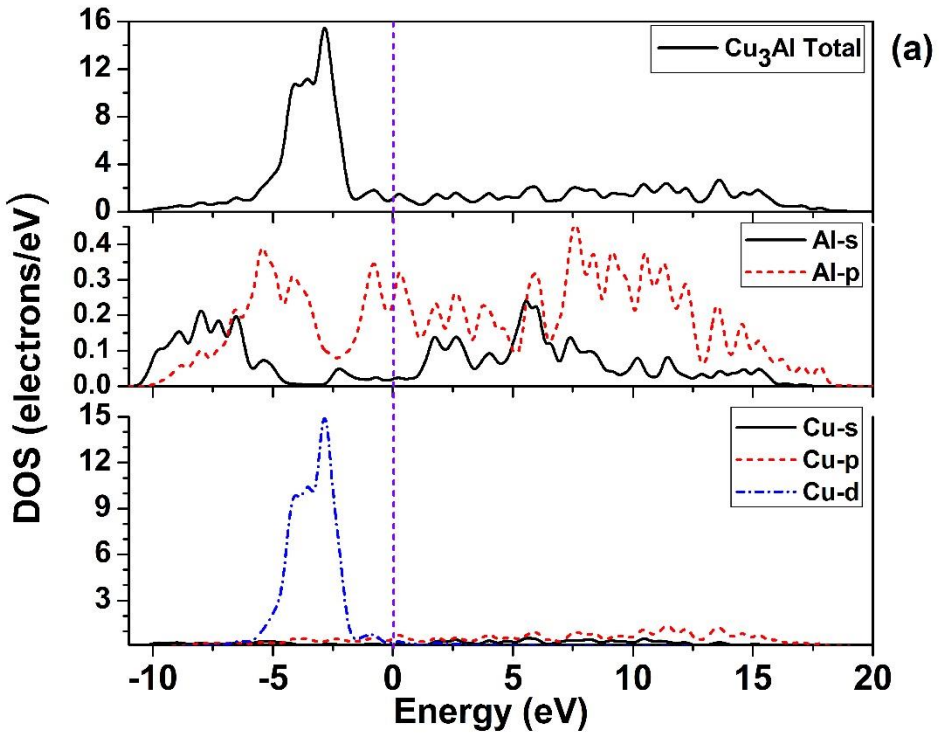

Figure 4.7. The DOS (Total and partial density of states) of (a) $L1_2$, and the Fermi level is defined at zero energy and is indicated by vertical lines.

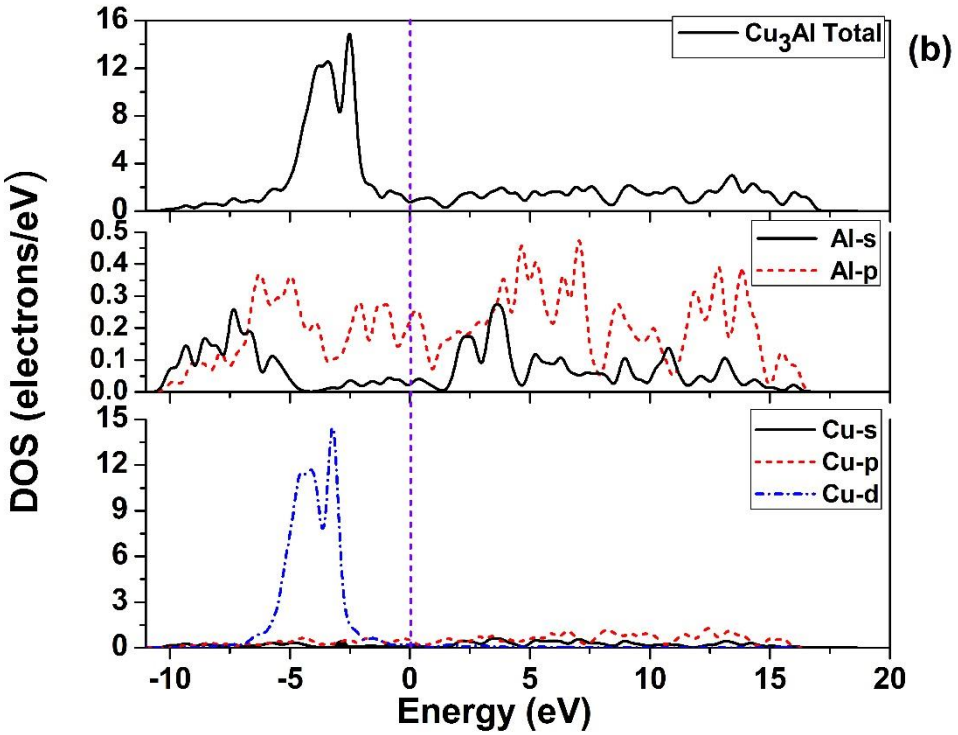

Figure 4.8. The DOS (Total and partial density of states) of (b) $D0_3$, and the Fermi level is defined at zero energy and is indicated by vertical lines.

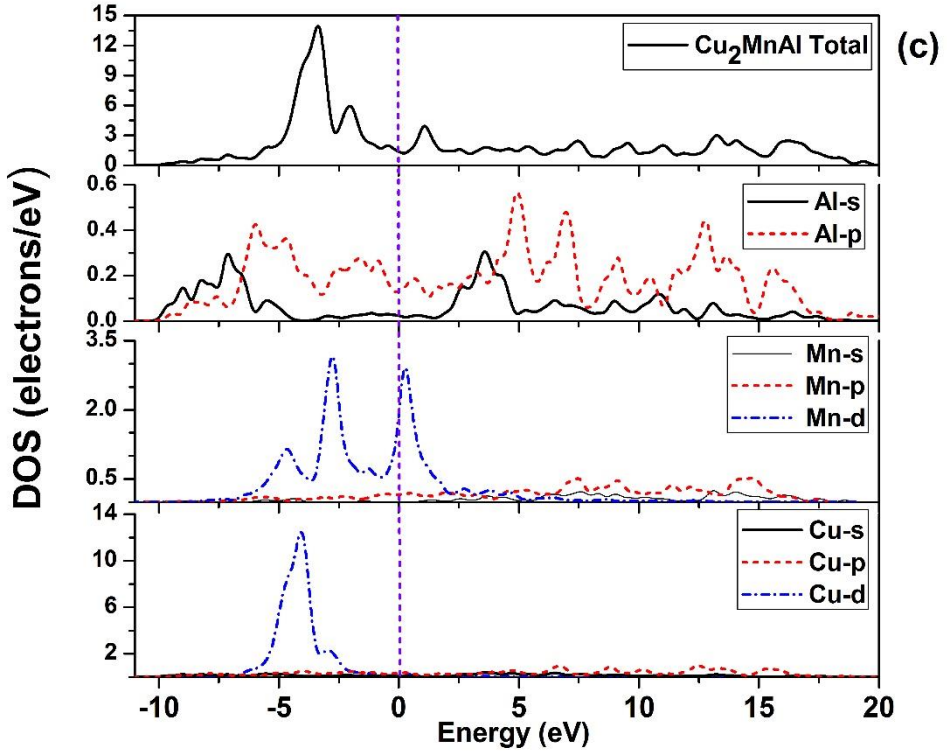

Figure 4.9. The DOS (Total and partial density of states) of (c) $L2_1$, and the Fermi level is defined at zero energy and is indicated by vertical lines.

Our results for the $L2_1$ type structure exhibit excellent consistency with previously reported studies by B. Benichou et al. [96], Rai et al. [102], and Kulkova et al. [103].

4.3. Charge Density Distribution & Population Analysis

Charge Density Distribution is a valuable feature for examining bonding behaviors [104]. Fig 5. presents the charge density distribution maps on the (0 0 1) plane for all type structures. The contour lines in **Figure 4.10** (a) $L1_2$, **Figure 4.11** (b) $D0_3$, **Figure 4.12** (c) $L2_1$ are plotted from 0 to 1 e/A^3 with 0.2 e/A^3 intervals. The region with higher density corresponds to the distribution of core electrons within the atoms, which contributes minimally to bonding. In **Figure 4.10** (a) ($L1_2$), the red color represents the Cu atom, while the nearest neighbors are Al atoms. The charge density distribution maps primarily demonstrate ionic bonding between Cu and Al atoms, resulting from the gain and loss of free electrons. On the other hand, there is an overlap between the orbitals of Al atoms, despite their distance from each other, suggesting covalent Al-Al bonds. In contrast, no such overlap is observed between Cu-Cu atoms, indicating that copper atoms form metallic bonds.

Figure 4.11 (b) ($D0_3$) also reveals metallic bonding between Cu-Cu atoms, characterized by the absence of orbital overlap and the presence of an electron cloud around them. For Al, it can be deduced that the aluminum atom primarily forms ionic bonding with adjacent Cu atoms and covalent bonding with the farther Cu atoms. Moreover, the overlap between Al-Al atoms is evident, suggesting covalent bonding between them.

In **Figure 4.12** (c) ($L2_1$), metallic bonding between Cu-Cu atoms is also observed. For Al, it can be deduced that the Al atom exhibits covalent bonding with adjacent Cu atoms and is strongly covalent with the Mn atoms. Furthermore, the overlap between Al-Al atoms is evident, suggesting covalent bonding between them. Additionally, Mn-Cu bonding appears to be a combination of ionic and covalent bonding.

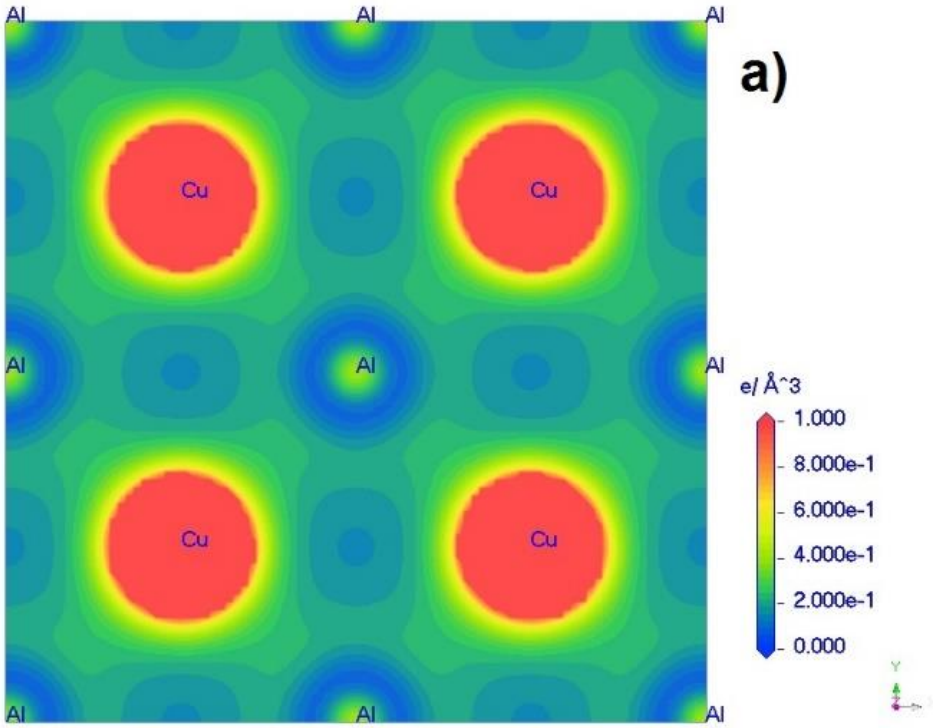

Figure 4.10. Contour plot of the electronic charge density in (0 0 1) plane: (a) $L1_2$.

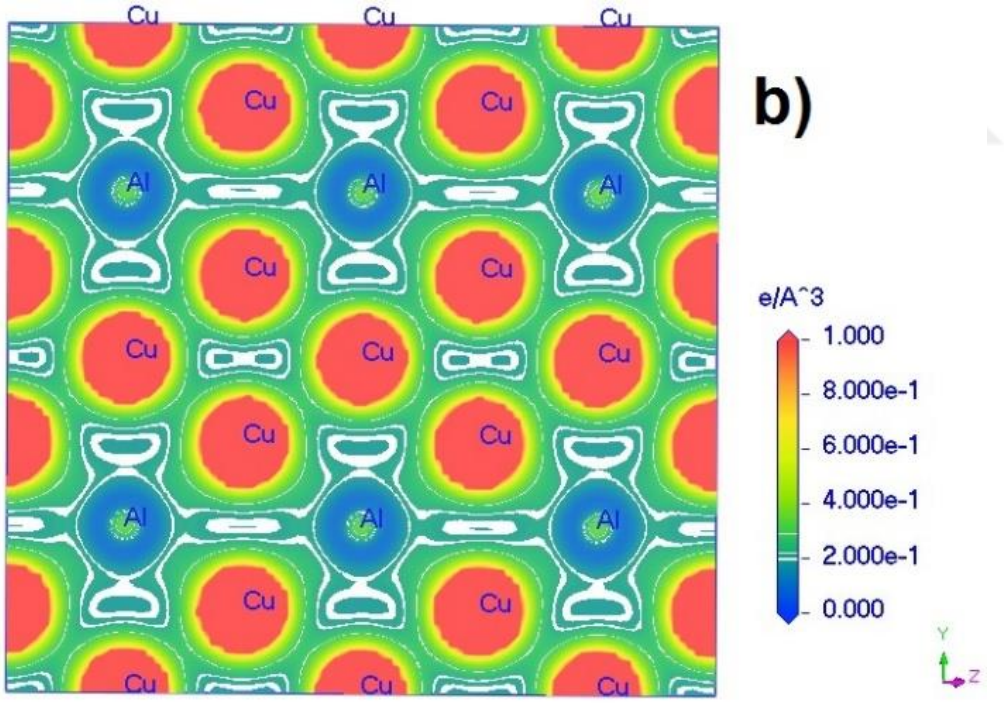

Figure 4.11. Contour plot of the electronic charge density in (0 0 1) plane: (b) $D0_3$.

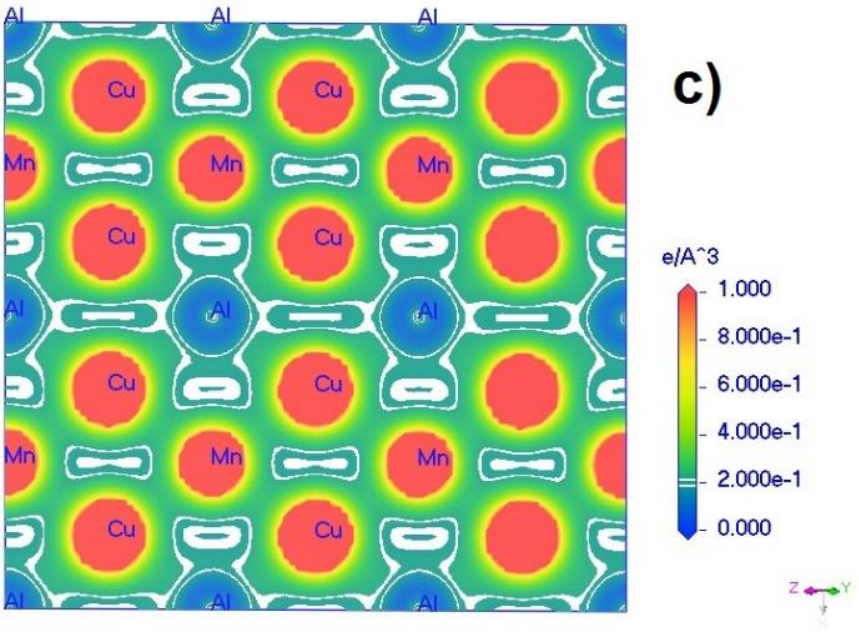

Figure 4.12. Contour plot of the electronic charge density in (0 0 1) plane: (c) $L2_1$.

To gain further insight into the bonding properties of all IMCs, we performed a Mulliken population analysis [70]. This analysis can explain the distribution of electrons in various fractional ways between formed chemical bonds. As observed by Segall et al. [105] there is a strong correlation between covalency [98], bond strength, and ionicity of bonds, which can be quantified by overlap population and Mulliken charge values.

In this analysis, the Mulliken charge *Q(A)* of one atom coupled with a particular atom-A (equation (4-2)), and overlap population *N(A, B)* in a typical A-B bond (equation (4-3)) can be defined as:

$$Q(A) = \sum_{k} W(k) \sum_{v}^{A} P_{\mu v}(k)\, S_{\mu v}(k) \tag{4-2}$$

$$N(A,B) = \sum_{k} W(k) \sum_{\mu}^{A} \sum_{v}^{B} P_{\mu v}(k)\, S_{\mu v}(k) \tag{4-3}$$

Here, $P_{\mu v}(k)$ and $S_{\mu v}(k)$ represent the density matrix and the overlap matrix, respectively. The indices μ and v correspond to the orbitals of atoms A and B, respectively. Additionally, $W(k)$ denotes the weight assigned to the k-points within the Brillouin zone.

As evident from **Table 4.2** electrons are transferred from the Aluminum atom to the Copper atoms in all phases, as indicated by the total charges of 0.47 and -0.48, 0.49 and -0.48, and 0.35 and -0.34 for Al and Cu atoms in $L1_2$, $D0_3$, $L2_1$ type structures, respectively. Loss and gain of electrons indicate that charge transfer occurs in $Cu_{(3-x)}Mn_xAl$, imparting ionic characteristics to these crystals.

The charge transfer in $Cu_{(3-x)}Mn_xAl$ phases accounts for their ionic nature in chemical bonding, indicating that these crystals exhibit some degree of ionic character.

Table 4.2. Atomic Mulliken charge & bond populations for all phases

Compound	Type Structure	Atoms (Species)	*s*	*p*	*d*	Total	(e) Charge	Bond	Population
Cu_3Al	$L1_2$	Al	0.77	1.76	-	2.53	0.47	Al-Cu Cu-Cu	0.82
		Cu_1	0.54	0.90	9.72	11.16	-0.16		0.04
		Cu_2	0.54	0.90	9.72	11.16	-0.16		
		Cu_3	0.54	0.90	9.72	11.16	-0.16		
	$D0_3$	Al	0.78	1.74	-	2.51	0.49	$Al-Cu_1$	0.70
		Cu_1	0.44	0.79	9.72	10.94	0.06	$Al-Cu_{2,3}$	0.99
		Cu_2	0.53	1.01	9.73	11.27	-0.27	$Cu_1-Cu_{2,3}$	0.35
		Cu_3	0.53	1.01	9.73	11.27	-0.27	Cu_2-Cu_3	0.35
Cu_2MnAl	$L2_1$	Al	0.79	1.87	-	2.65	0.35	Al-Mn	0.38
		Mn	0.13	0.26	5.64	6.02	0.98	$Mn-Cu_{1,2}$	0.16
		Cu_1	0.69	1.26	9.71	11.66	-0.66	$Al-Cu_{1,2}$	1.19
		Cu_2	0.69	1.26	9.71	11.66	-0.66	Cu_1-Cu_2	0.42

4.4. Spin Polarizability & Magnetic Behavior

To investigate the magnetic nature of all $Cu_{(3-x)}Mn_xAl$ (x = 0, 1) IMCs, the spin polarizability, and total and partial magnetic moments were calculated, compared and depicted in **Figure 4.13**. The figures reveal that the majority and minority spin states of the (a) $L1_2$ and (b) $D0_3$ type structures exhibit symmetry, indicating the absence of magnetic behavior and polarizability in these structures. In contrast, the (c) L21 type structure, which contains Mn atoms and exhibits a Heusler orientation, displays asymmetry between the major and minor spin states, resulting in an asymmetric DOS for the Cu2MnAl Heusler alloy.

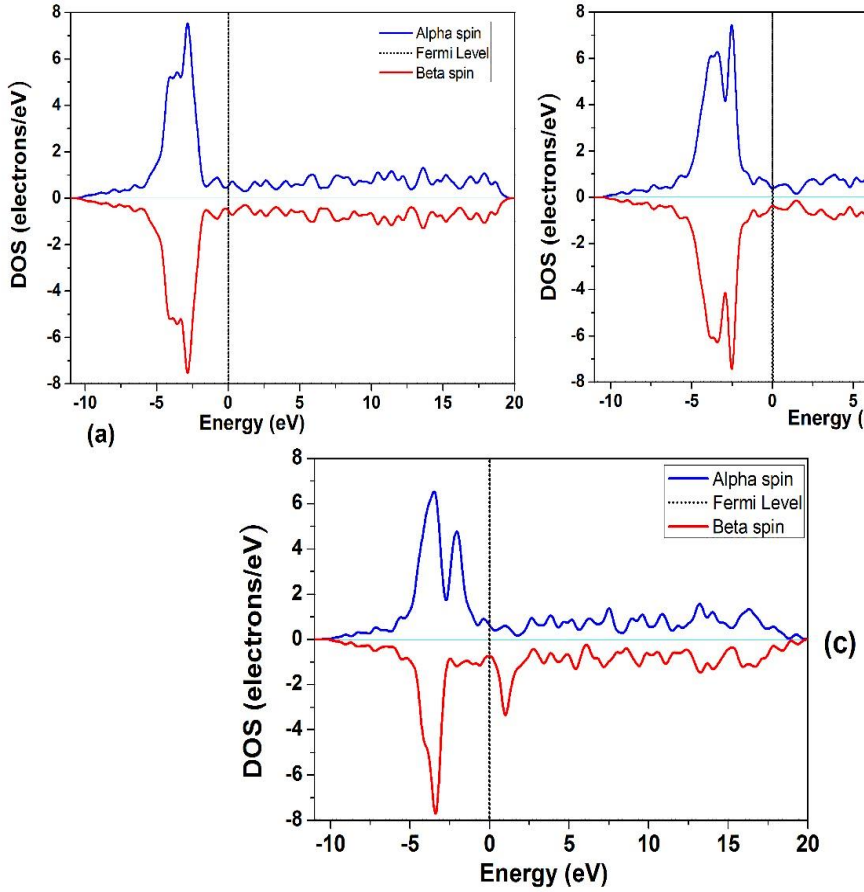

Figure 4.13. Spin polarizability for major and minor spin for (a) $L1_2$, (b) $D0_3$, and (c) $L2_1$ type structures.

Table 4.3 lists the total and partial magnetic moments of all type structures. From this table, it is evident that Cu and Al don't have any contribution to magnetization in $L1_2$ and $D0_3$ type structures, implying that Cu and Al are nearly non-ferromagnetic due to their equal *Alpha (Up)* and *Beta (Down)* spin density. In the case of $L2_1$ type structure,

Cu and Al have a small contribution of magnetic moment -0.17 and -0.4 μB respectively. The presence of the unoccupied minority spin states, identified as Mn *3d* states, leads to the exclusions of minority-spin electrons, resulting in the localization of the Mn *3d* moment. Consequently, the local magnetic moment of Mn is determined to be 3.87 μB independently, indicating increased magnetization of the corresponding compound, which is the basic characteristic of Heusler alloys. Our calculated total magnetic moment of Cu_2MnAl shows remarkable consistency with both experimental values reported by H. Okumura et al. and the theoretical values obtained by Kulkova et al. as well as other researchers [50], [96], [103], [106], [107], [108], [109], [110].

Table 4.3. Calculated partial and total magnetic moment of $Cu_{(3-x)}Mn_xAl$ (x = 0, 1) in μB unit.

Compound	Type Structure	Species	*Alpha*	*Beta*	Partial μB	Total μB	Ref.
Cu_3Al	$L1_2$	Al	1.20	1.20	0	0	-
		Cu	16.3	16.3	0		
		Sum	17.50	17.50	-		
		Interstitial	-	-	-		
	$D0_3$	Al	1.22	1.22	0	0	-
		Cu	16.3	16.3	0		
		Sum	17.52	17.52	-		
		Interstitial	-	-	-		
Cu_2MnAl	$L2_1$	Al	1.2	1.37	-0.17	**3.4**	**This work**
		Mn	4.96	1.09	3.87	3.6	Exp.
		Cu	11.1	11.5	-0.4	3.6	Exp.
		Sum	17.26	13.96	-	3.2	Exp.(298 K)
		Interstitial	-	-	0.1	3.7	Exp. (77K)
						4	Exp. (4K)
						3.502	Calc.
						3.47	Calc.
						3.6	Calc.
						3.50	Calc.

4.5. Mechanic Properties

In this study, the mechanical properties of $Cu_{(3-x)}Mn_xAl$ (x = 0, 1) intermetallic compounds with a cubic crystal structure, were calculated. As a result of the calculations, the elastic (Stiffnes) constants (Cij) and compliance constants (Sij) of the

IMCs were obtained. Based on the elastic constants, various mechanical properties were derived, including the bulk modulus (B), which is the inverse of linear compressibility, the shear modulus (G), Young's modulus (E), and Poisson's ratio (ν). Additionally, the theoretical Vickers hardness (H_V), Pugh's ratio (B/G), Cauchy pressure (P), and elastic anisotropy were determined. As is well known in the literature[79], [80], [88], [111] and as mentioned in Section 2, cubic materials have three specific independent elastic constants: C_{11}, C_{12}, and C_{44}. Among these, C_{11} defines the longitudinal elastic behavior of a cubic material, while C_{12} represents the off-diagonal elastic interaction, and C_{44} characterizes the shear elastic properties of the material [88].

The calculated elastic constants of the IMCs are presented in **Table 4.4**.

Table 4.4. The calculated elastic (Stiffnes) constants (Cij) and compliance constants (Sij) of the IMCs

Type	C_{11}	C_{12}	C_{44}	S_{11}	S_{12}	S_{44}
$L1_2$	154.14270	116.39455	87.2113	0.018522	-0.007969	0.011466
Ref. [1]	155.02	120.57	82.10	-	-	-
Ref. [16]	140.42	118.41	74.69	-	-	-
Ref. [52]	157.5	120.7	91.6	0.01892	- 0.00820	0.01091
$D0_3$	138.8081	124.1452	99.02630	0.046327	-0.021872	0.010098
$L2_1$	132.17720	117.46315	106.09965	0.046216	-0.021746	0.009425

As seen in **Table 4.4** the calculated elastic constants (Cij) of three intermetallic compounds have shown a remarkably high agreement with the values reported in the literature [1], [16], [52], [53] . Elastic constants of all IMCs satisfy the mechanical stability criteria associated with Cubic crystal-structured materials, indicating that they are mechanically stable. Additionally, in all IMCs, the C_{11} value is observed to be greater than the C_{12} and C_{44} values. Consequently, it is expected that all IMCs will exhibit higher resistance to pressure applied along the a-axis compared to the b- and c-axes.

4.5.1. Elastic Tensors

After calculating the elastic tensors of the all $Cu_{(3-x)}Mn_xAl$ (x = 0, 1) intermetallic compounds, the corresponding pattern matrix and its value for the material's cubic crystal lattice are presented below.

The elastic tensors matrix of the Cu_3Al ($L1_2$-221 type structure) with coefficients expressed in GPa.

$$Cij = \begin{bmatrix} 154.14270 & 116.39455 & 116.39455 & 0 & 0 & 0 \\ 116.39455 & 154.14270 & 116.39455 & 0 & 0 & 0 \\ 116.39455 & 116.39455 & 154.14270 & 0 & 0 & 0 \\ 0 & 0 & 0 & 87.2113 & 0 & 0 \\ 0 & 0 & 0 & 0 & 87.2113 & 0 \\ 0 & 0 & 0 & 0 & 0 & 87.2113 \end{bmatrix}$$

The elastic tensors matrix of the Cu_3Al ($D0_3$-225 type structure) with coefficients expressed in GPa.

$$Cij = \begin{bmatrix} 138.8081 & 124.1452 & 124.1452 & 0 & 0 & 0 \\ 124.1452 & 138.8081 & 124.1452 & 0 & 0 & 0 \\ 124.1452 & 124.1452 & 138.8081 & 0 & 0 & 0 \\ 0 & 0 & 0 & 99.02630 & 0 & 0 \\ 0 & 0 & 0 & 0 & 99.02630 & 0 \\ 0 & 0 & 0 & 0 & 0 & 99.02630 \end{bmatrix}$$

And finaly the elastic tensors matrix of the Cu_2MnAl ($L2_1$-225 type structure) with coefficients expressed in GPa.

$$Cij = \begin{bmatrix} 132.1772 & 117.46315 & 117.46315 & 0 & 0 & 0 \\ 117.46315 & 132.1772 & 117.46315 & 0 & 0 & 0 \\ 117.46315 & 117.46315 & 132.1772 & 0 & 0 & 0 \\ 0 & 0 & 0 & 106.09965 & 0 & 0 \\ 0 & 0 & 0 & 0 & 106.09965 & 0 \\ 0 & 0 & 0 & 0 & 0 & 106.09965 \end{bmatrix}$$

As shown in the matrices, only three elastic tensors of Cubic systems, C_{11}, C_{12}, and C_{44}, have values and satisfy the stability criteria.

As mentioned in sction 2 by using the Voigt–Reuss–Hill (VRH) approximation method the calculated elastic values of $L1_2$ $D0_3$, and $L2_1$ type Structures is given in **Table 4.5**, **Table 4.6**, and **Table 4.7** respectively.

Table 4.5. The calculated elastic values of $L1_2$ Type Structure.

Methods	***B* modulus**	***E* modulus**	***G* modulus**	***v* ratio**
Voigt	K_V = 128.98 GPa	E_V = 155.56 GPa	G_V = 59.876 GPa	v_V = 0.29899
Reuss	K_R = 128.98 GPa	E_R = 97.856 GPa	G_R = 35.621 GPa	v_R = 0.37355
Hill	K_H = 128.98 GPa	E_H = 127.51 GPa	G_H = 47.749 GPa	v_H = 0.33523

Table 4.6. The calculated elastic values of $D0_3$ Type Structure.

Methods	***B* modulus**	***E* modulus**	***G* modulus**	***v* ratio**
Voigt	K_V = 128.98 GPa	E_V = 155.56 GPa	G_V = 59.876 GPa	v_V = 0.29899
Reuss	K_R = 128.98 GPa	E_R = 97.856 GPa	G_R = 35.621 GPa	v_R = 0.37355
Hill	K_H = 128.98 GPa	E_H = 127.51 GPa	G_H = 47.749 GPa	v_H = 0.33523

Table 4.7. The calculated elastic values of $L2_1$ Type Structure.

Methods	***B* modulus**	***E* modulus**	***G* modulus**	***v* ratio**
Voigt	K_V = 128.98 GPa	E_V = 155.56 GPa	G_V = 59.876 GPa	v_V = 0.29899
Reuss	K_R = 128.98 GPa	E_R = 97.856 GPa	G_R = 35.621 GPa	v_R = 0.37355
Hill	K_H = 128.98 GPa	E_H = 127.51 GPa	G_H = 47.749 GPa	v_H = 0.33523

In order to compare elastic properties and mechanical parameters together and to evaluate them with a deeper perspective, **Table 4.8**. presents the computed data encompassing various mechanical properties of IMCs, including the bulk modulus (B_{VRH}), shear modulus (G_{VRH}), Young's modulus (E), Poisson's ratio (ν), Pugh's ratio (B_H/G_H), and theoretical Vickers hardness (H_V).

Table 4.8. The calculated elastic modulus values (B, G, and E) for IMCs (in GPa), Poisson's ratio (ν), Pugh's ratio (B/G), and theoretical Vickers hardness (H_V) (in GPa).

Type	B_V	B_R	B_H	G_V	G_R	G_H	E	ν	B/G	H_V
$L1_2$	128.97727	128.97727	128.97727	59.87641	35.62150	47.74895	127.51144	0.33523	2.7011	4.59011
Ref. [1]	-	-	132.05	-	-	44.45	-	0.34	2.9	-
Ref. [52]	132.9	132.9	132.9	62.3	35.4	48.9	130.6	0.336	2.41	4.6
Ref . [33]	136.9	136.9	136.9	67.1	49.6	58.4	153.4	0.31	-	-
$D0_3$	129.03283	129.03283	129.03283	62.34836	16.49662	39.42249	107.33625	0.36136	3.2730	3.22158
$L2_1$	122.36783	122.36783	122.36783	66.60260	16.65976	41.63118	112.17266	0.34722	2.9393	3.78388

When examining **Table 4.8**, the highest compressibility is observed in the $L2_1$ compound, which possesses the lowest bulk modulus. The highest shear strength is attributed to the $L1_2$ compound. Similarly, the greatest stiffness corresponds to the $L1_2$ compound, which exhibits the highest Young's modulus.

Regarding Poisson's ratio, among the analyzed compounds, $L1_2$, with a value of 0.33, demonstrates the highest degree of covalent bonding. The assessment of the *B/G* (Pugh's) ratio clearly indicates that all three compounds exhibit ductile behavior. In parallel with Young's modulus, the highest hardness value is observed in the $L1_2$ compound, whereas the lowest hardness is recorded in the $D0_3$ compound. The data we obtained are further validated as they align with and support the findings reported in the references [1], [33], [52].

Table 4.9 presents the computed values of Cauchy Pressure (Cp) and the Universal Anisotropy Index (AU) for intermetallic compounds IMCs.

Table 4.9. The calculated Cauchy Pressure (Cp) and Universal Anisotropy Index (A^U) for IMCs.

Type	***Cauchy Pressure (Cp)***	***Cauchy State***	***Universal Anisotropy Index (A^U)***
$L1_2$	66.9314	***Positive***	3.404530
Ref. [1]	72.92	***Positive***	4.77
Ref. [33]	83.6	***Positive***	3.15
$D0_3$	39.7818	***Positive***	13.89731
$L2_1$	26.07755	***Positive***	14.98906

Examining **Table 4.9**., it is evident that all three Cauchy pressure values are positive, indicating that all three compounds exhibit ductile behavior. These findings are consistent with the results derived from the Pugh's ratio.

The highest anisotropy index is observed in the $L2_1$ compound, whereas the lowest value is found in the $L1_2$ compound. Consequently, the greatest directional deviation

in mechanical properties is expected in $L2_1$. Following this trend, anisotropy decreases progressively from $D0_3$ to $L1_2$.

4.5.2. Elastic Anisotropy of Young's Modulus

Elastic Anisotropy of a material is illustrated by three-dimensional (3D) diagrams showing the directional Young moduli and two-dimensional (2D) diagrams representing the Young moduli in (XY), (XZ), and (YZ) planes. With the help of Anovis software, the Young modulus of $L1_2$-221, $D0_3$-225 $L2_1$-225 type structures are 127.511 (E_{Hill}), 107.336 (E_{Hill}), and 112.172 (E_{Hill}) respectively while the directional dependence of these moduli and the anisotropic behavior in different crystal planes are visualized in both two-dimensional (2D) and three-dimensional (3D) domains as follows. In the three-dimensional representation of the directional Young modulus, the degree of anisotropy is proportional to the degree of deviation from a perfect sphere. In other words, the more the perfect sphere representation exists, the more the material is isotropic and the degree of anisotropy increases as it deviates from the spherical shape [71], [98]. The three-dimensional representation of the directional Young moduli for $L1_2$, $D0_3$, and $L2_1$ type structures are shown in **Figure 4.14**. respectively. According to our calculations, the anisotropy degree of the $L1_2$, $D0_3$, and $L2_1$ type structures are 3.40453, 13.89731, and 14.98906 respectively.

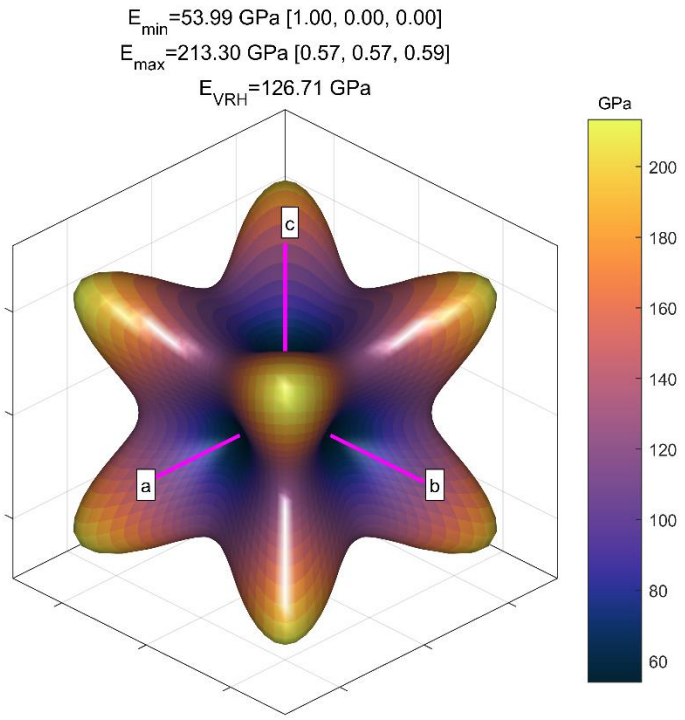

Figure 4.14. Three-dimensional direction-dependent Young modulus of the $L1_2$ type structure.

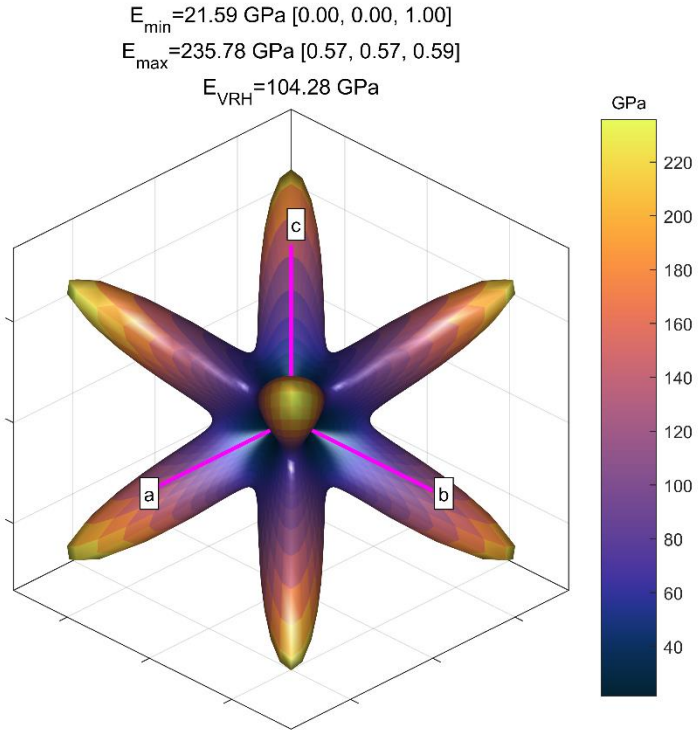

Figure 4.15. Three-dimensional direction-dependent Young modulus of the $D0_3$ type structure.

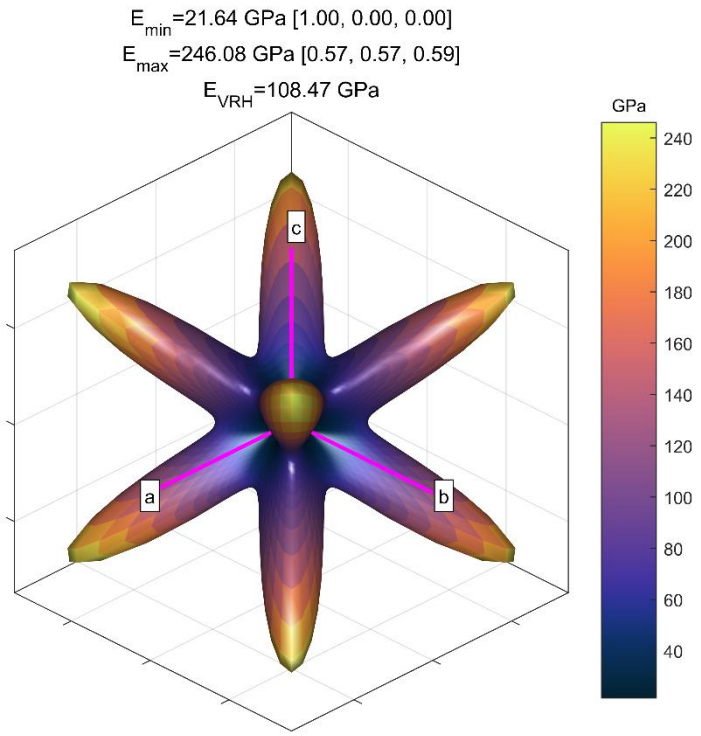

Figure 4.16. Three-dimensional direction-dependent Young modulus of the $L2_1$ type structure.

From **Figure 4.14**, **Figure 4.15**, and **Figure 4.16**. one can see that deviations from sphericity are observed along all three axes in each of the three compounds, indicating their anisotropic nature. The most significant deviation from sphericity is identified in the $L2_1$ compound, while the least deviation is found in the $L1_2$ compound. These findings are in direct agreement with the values of the Universal Anisotropy Index.

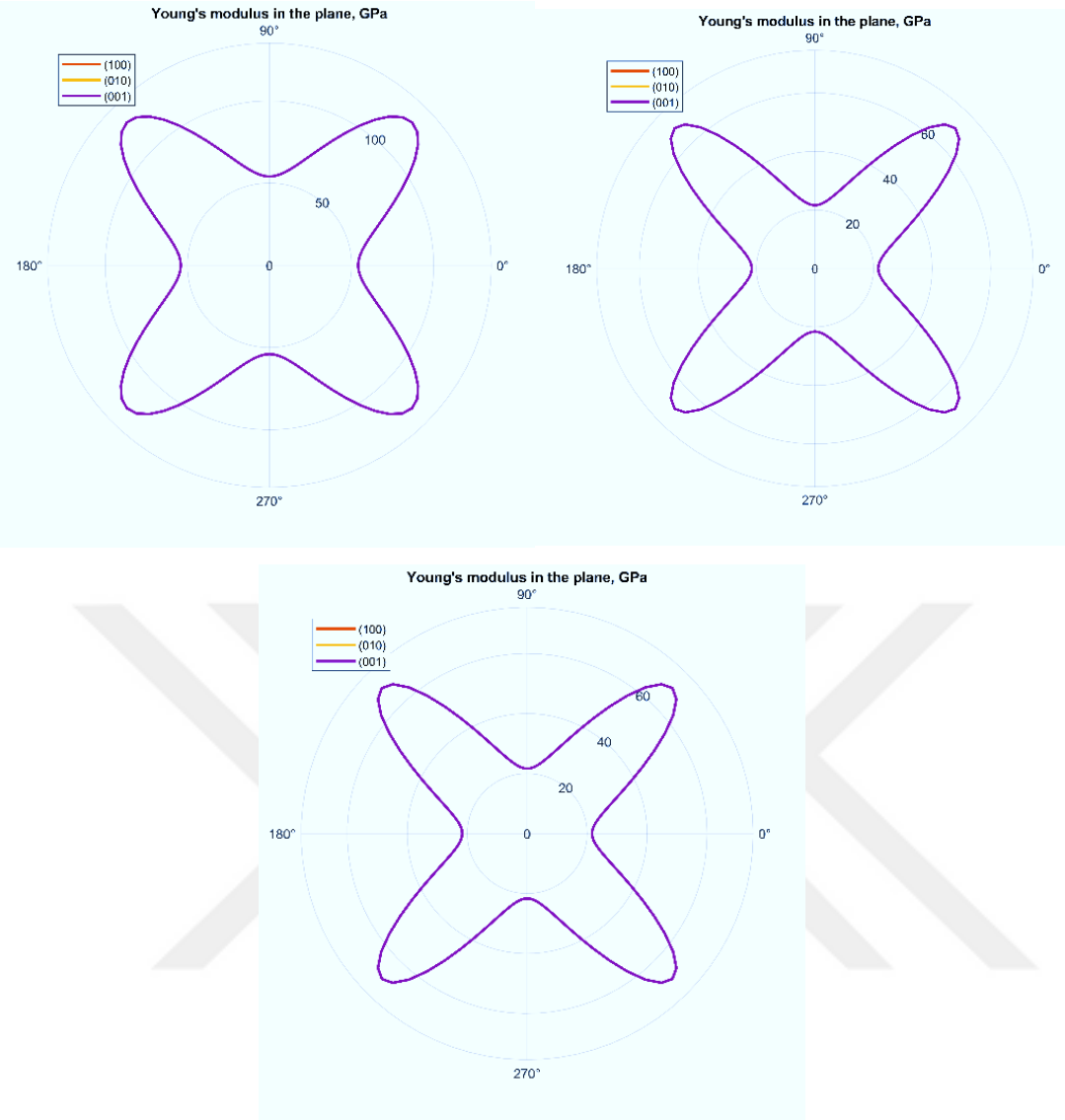

Figure 4.17. Two-dimensional direction-dependent Young modulus of the all type strutures.

The two-dimensional representation of the directional Young moduli all type structure s are also shown in **Figure 4.17**. In this figure significant deviations from sphericity are observed along all three axes, indicating pronounced elastic anisotropy in compounds belonging to the 225 space group. When compared to the 221 space group, a substantial increase in the degree of anisotropy is evident. Three-dimensional direction-dependent Young modulus of the $L1_2$ type structure. In the following study, all three intermetallic compounds along with their three-directional dependence of shear modulus, bulk modulus, Poisson's ratio, and mechanical properties are fully given in Appendix A.

5. CONCLUSION AND RECOMMENDATIONS

In conclusion, the first-principles calculations based on GGA approximations were used to predict the structural parameters, electronic properties, charge density distribution, and spin polarizability of the $Cu_{(3-x)}Mn_xAl$ (x = 0, 1) IMCs. Our results show that the lattice constants shows remarkable consistency with both experimental and theoretical values reported in the literature. Notably, this study provides the first prediction and discussion of the physical properties of Cu_3Al with the space group $D0_3$ (*225-Fm3m*) for the targeted properties. The analysis of the density of states and the electronic band structures shows that Cu_3Al IMCs are metallic and conductive compounds. Furthermore, our findings confirm that Cu_2MnAl Heusler alloy is a ferromagnetic and metallic compound by nature. Charge density distribution shows the dominant bonding type of each IMC and, demonstrating that the interior bonding of metallic alloys can include a complex interplay of metallic, ionic, and covalent bonding.

In the mechanical properties, we studied structural and elastic properties. By the approximations (DFT- GGA: PBE) of the $Cu_{(3-x)}Mn_xAl$ (x = 0, 1) IMCs in three structures. The calculated lattice constants and bulk modulus agree well with the experimental data and other calculations. The variations of lattice constants and bulk modulus as a function of composition are discussed. The results show also that the elastic constants (C_{11}, C_{12}, and C_{44}) calculated in this work, conform to the elastic stability criteria. The values of the polycrystalline elastic properties including bulk B and shear moduli G, Young's modulus E, Poisson's ratio ν, and B/G ratio, for each type structure are also presented. Additionally, the study of mechanical properties of intermetallic compounds (IMCs), such as elastic constants, elastic moduli, Pugh's ratio, elastic anisotropy, Poisson's ratio, and Cauchy pressure were demonstrated the strength and elastic properties of the material one by one, showing that they were in full consistency with the other properties obtained. The directional dependence of each mechanical property (young, bulk, shear modulus) and the corresponding mechanical

properties revealed the direction-dependent anisotropy degrees of the related intermetallic compounds by computational methods.

Although the Cu_3Al compound naturally forms more readily in space group 221, it can also exist in the more complex space group 225 while maintaining the same stoichiometric composition, specifically in the $D0_3$-type structure. Consequently, most studies in the literature primarily focus on space group 221, whereas research on space group 225 remains limited. The preference for space group 221 in nature is attributed to its lower atomic number requirement, more compact and smaller structural dimensions, and lower formation energy. Additionally, when transitioning to space group 225, different stoichiometries or phases can emerge within the same space group. In this study, the Heusler alloy Cu_3MnAl, which adopts an $L2_1$-type structure through the incorporation of Mn, is investigated. However, Future studies, particularly experimental investigations, should focus on optimizing laboratory conditions to facilitate the natural formation of the Cu_3Al compound with the $D0_3$ structure in space group No: 225. The parameters that should be considered for the natural formation of the space group No 225 or the laboratory conditions that will prevent the formation of this space group should be emphasized. Moreover, once synthesized, the experimental product should be systematically compared with the data we obtain and present in the literature through density functional theory (DFT) calculations to validate the theoretical predictions.

REFERENCES

[1] T. Tian, X. F. Wang, and W. Li, “Ab initio calculations on elastic properties in L12 structure Al3X and X3Al-type (X=transition or main group metal) intermetallic compounds,” *Solid State Commun*, vol. 156, pp. 69–75, 2013, doi: 10.1016/j.ssc.2012.10.021.

[2] F. R. Eshelman and J. F. Smith, “Single-crystal elastic constants of Al2Cu,” *J Appl Phys*, vol. 49, no. 6, pp. 3284–3288, 1978, doi: 10.1063/1.325278.

[3] S. Ganeshan, S. L. Shang, H. Zhang, Y. Wang, M. Mantina, and Z. K. Liu, “Elastic constants of binary Mg compounds from first-principles calculations,” *Intermetallics (Barking)*, vol. 17, no. 5, pp. 313–318, 2009, doi: https://doi.org/10.1016/j.intermet.2008.11.005.

[4] C. Wolverton and V. Ozoliņš, “Entropically favored ordering: The metallurgy of Al 2 Cu revisited,” *Phys Rev Lett*, vol. 86, no. 24, pp. 5518–5521, Jun. 2001, doi: 10.1103/PhysRevLett.86.5518.

[5] H. Chen, L. Yang, and J. Long, “First-principles investigation of the elastic, Vickers hardness and thermodynamic properties of Al–Cu intermetallic compounds,” *Superlattices Microstruct*, vol. 79, pp. 156–165, 2015, doi: https://doi.org/10.1016/j.spmi.2014.11.005.

[6] V. Vaithyanathan and L. Q. Chen, “Coarsening kinetics of δ′-Al3Li precipitates: phase-field simulation in 2D and 3D,” *Scr Mater*, vol. 42, no. 10, pp. 967–973, 2000, doi: https://doi.org/10.1016/S1359-6462(00)00323-7.

[7] M. D. Rossell, R. Erni, M. Asta, V. Radmilovic, and U. Dahmen, “Atomic-resolution imaging of lithium in ${\text{Al}}_{3}\text{Li}$ precipitates,” *Phys Rev B*, vol. 80, no. 2, p. 24110, Jul. 2009, doi: 10.1103/PhysRevB.80.024110.

[8] R. W. Cahn, “Combining metals and sciences: Ways of investigating intermetallics,” *Intermetallics (Barking)*, vol. 6, no. 7–8, pp. 563–566, 1998, doi: 10.1016/s0966-9795(98)00027-2.

[9] S. Javaheri, M. Babaeipour, A. Boochani, and S. Naderi, “Electronic and optical properties of V doped AlN nanosheet: DFT calculations,” *Chinese Journal of Physics*, vol. 56, no. 6, pp. 2698–2709, 2018, doi: 10.1016/j.cjph.2018.10.021.

[10] M. D. Rossell, R. Erni, M. Asta, V. Radmilovic, and U. Dahmen, “Atomic-resolution imaging of lithium in Al3×Li precipitates,” *Phys Rev B*, vol. 80, no. 2, p. 24110, Jul. 2009, doi: 10.1103/PhysRevB.80.024110.

[11] F. Lanzini, P. H. Gargano, P. R. Alonso, and G. H. Rubiolo, “First-principles study of atomic ordering in bcc Cu-Al,” *Model Simul Mat Sci Eng*, vol. 19, no. 1, 2011, doi: 10.1088/0965-0393/19/1/015008.

[12] F. Apostol and Y. Mishin, “Interatomic potential for the Al-Cu system,” *Phys Rev B Condens Matter Mater Phys*, vol. 83, no. 5, pp. 1–8, 2011, doi: 10.1103/PhysRevB.83.054116.

[13] Y. Liu, J. Wang, Q. nan Gao, and Y. Du, “Structural, elastic and electronic properties of Cu-X compounds from first-principles calculations,” *J Cent South Univ*, vol. 22, no. 5, pp. 1585–1594, 2015, doi: 10.1007/s11771-015-2675-7.

[14] Learning Chemistry Online, “Metal in the Periodic Table,” Learning Chemistry Online.

[15] W. J. Meng, J. Faber, P. R. Okamoto, L. E. Rehn, B. J. Kestel, and R. L. Hitterman, “Neutron diffraction and transmission electron microscopy study of hydrogen-induced phase transformations in Zr3Al,” *J Appl Phys*, vol. 67, no. 3, pp. 1312–1319, 1990, doi: 10.1063/1.345683.

[16] N. Boudalia, J. M. Raulot, E. Patoor, and C. Esling, “Phase Stability Study of the Shape Memory Alloy CuAl-X (X: Be, Zn, Ti, Ni, Ag and Au) by Ab Initio Calculations,” *Materials Science Forum*, vol. 879, pp. 250–255, 2017, doi: 10.4028/www.scientific.net/MSF.879.250.

[17] M. Draissia, M. Y. Debili, N. Boukhris, M. Zadam, and S. Lallouche, “Metastable Ordered Cu3Al Phase in Sputter-Deposited Al-Cu Alloys System,” *Copper: Better Properties for Innovative Products*, pp. 65–70, 2006, doi: 10.1002/9783527610327.ch8.

[18] F. Heusler, W. Starck, and E. Haupt, “Magnetisch-chemische studien,” *Verh. Dtsch. Phys. Ges*, vol. 5, pp. 219–232, 1903.

[19] D. P. Oxley, R. S. Tebble, and K. C. Williams, “Heusler alloys,” *J Appl Phys*, vol. 34, no. 4, pp. 1362–1364, 1963, doi: 10.1063/1.1729511.

[20] A. N. Titenko, L. D. Demchenko, A. O. Perekos, and O. Y. Gerasimov, “Effect of Thermomagnetic Treatment on Structure and Properties of Cu–Al–Mn Alloy,” *Nanoscale Res Lett*, vol. 12, no. 1, 2017, doi: 10.1186/s11671-017-2052-6.

[21] A. Jazideh, A. Boochani, and B. Arghavani Nia, “Half-metallic, magneto-optic, and thermoelectric properties of CoRuVZ (Z=Al, Ga),” *Phys Lett A*, vol. 414, p. 127622, 2021, doi: https://doi.org/10.1016/j.physleta.2021.127622.

[22] C. Felser, G. H. Fecher, and B. Balke, “Spintronics: A challenge for materials science and solid-state chemistry,” *Angewandte Chemie - International Edition*, vol. 46, no. 5, pp. 668–699, 2007, doi: 10.1002/anie.200601815.

[23] H. Zabel, “Progress in spintronics,” *Superlattices Microstruct*, vol. 46, no. 4, pp. 541–553, 2009, doi: 10.1016/j.spmi.2009.07.008.

[24] X. Wang, Z. Cheng, H. Khachai, R. Khenata, and T. Yang, “Electronic, magnetic, and thermodynamic properties of rhombohedral Dysprosium Manganite and discussions of effects of uniform strain, spin-orbit coupling, hole and electron doping on its electronic structures,” *J Solid State Chem*, vol. 276, pp. 352–360, 2019, doi: 10.1016/j.jssc.2019.05.030.

[25] Z. Chen *et al.*, “First-Principles Study on a New All- d -Metal Full-Heusler-Based Shape-Memory Alloy Cd2MnPd,” *Spin*, vol. 9, no. 3, pp. 1–7, 2019, doi: 10.1142/S2010324719500127.

[26] R. Bentata *et al.*, "New p-type sp-based half-Heusler compounds LiBaX(X = Si, Ge) for spintronics and thermoelectricity via ab-initio calculations," *J Comput Electron*, vol. 20, no. 3, pp. 1072–1082, 2021, doi: 10.1007/s10825-021-01702-x.

[27] S. Parsamehr *et al.*, "Thermodynamic phase diagram and thermoelectric properties of LiMgZ (Z = P, As, Bi): ab initio method study," *Philosophical Magazine*, vol. 101, no. 3, pp. 369–386, Feb. 2021, doi: 10.1080/14786435.2020.1839138.

[28] A. Wederni, J. Daza, W. Ben Mbarek, J. Saurina, L. Escoda, and J.-J. Suñol, "Crystal Structure and Properties of Heusler Alloys: A Comprehensive Review," *Metals (Basel)*, vol. 14, no. 6, 2024, doi: 10.3390/met14060688.

[29] V. Milman *et al.*, "Electronic Structure, Properties, and Phase Stability of Inorganic Crystals: A Pseudopotential Plane-Wave Study," *Int J Quantum Chem*, vol. 77, no. 5, pp. 895–910, 2000, doi: 10.1002/(SICI)1097-461X(2000)77:5<895::AID-QUA10>3.0.CO;2-C.

[30] W. Zhou, L. Liu, B. Li, Q. Song, and P. Wu, "Structural, elastic, and electronic properties of Al-Cu intermetallics from first-principles calculations," *J Electron Mater*, vol. 38, no. 2, pp. 356–364, 2009, doi: 10.1007/s11664-008-0587-0.

[31] R. Parvin, F. Parvin, M. S. Ali, and A. K. M. A. Islam, "Band structure, Fermi surface, elastic, thermodynamic, and optical properties of AlZr3, AlCu3, and AlCu2Zr: First-principles study," *Chinese Physics B*, vol. 25, no. 8, 2016, doi: 10.1088/1674-1056/25/8/083101.

[32] A. Meng, J. Nie, K. Wei, H. Kang, Z. Liu, and Y. Zhao, "Optimization of strength, ductility and electrical conductivity of a Cu–Cr–Zr alloy by cold rolling and aging treatment," *Vacuum*, vol. 167, no. June, pp. 329–335, 2019, doi: 10.1016/j.vacuum.2019.06.027.

[33] W. Zhou, L. Liu, B. Li, Q. Song, and P. Wu, "Structural, elastic, and electronic properties of Al-Cu intermetallics from first-principles calculations," *J Electron Mater*, vol. 38, no. 2, pp. 356–364, 2009, doi: 10.1007/s11664-008-0587-0.

[34] C. D. Yang, W. Li, and W. Zhi, "Study on mechanical behavior and electronic structures of Al–Cu intermetallic compounds based on first-principles calculations," *Solid State Commun*, vol. 151, no. 18, pp. 1270–1274, 2011, doi: https://doi.org/10.1016/j.ssc.2011.05.040.

[35] L. Hao, R. Khenata, X. Wang, and T. Yang, "Ab Initio Study of the Structural, Electronic, Magnetic, Mechanical and Thermodynamic Properties of Full-Heusler Mn2CoGa," *J Electron Mater*, vol. 48, no. 10, pp. 6222–6230, 2019, doi: 10.1007/s11664-019-07417-x.

[36] X. T. Wang, J. W. Lu, H. Rozale, X. F. Liu, Y. T. Gui, and G. D. Liu, "Half-metallic state and magnetic properties versus the lattice constant in Zr2RhZ (Z= Al, Ga, In) Heusler alloys," *arXiv preprint arXiv:1505.00203*, 2015, doi: 10.48550/arXiv.1505.00203.

[37] N. Ponweiser, C. L. Lengauer, and K. W. Richter, “Re-investigation of phase equilibria in the system Al-Cu and structural analysis of the high-temperature phase η1-Al 1-δCu,” *Intermetallics (Barking)*, vol. 19, no. 11, pp. 1737–1746, 2011, doi: 10.1016/j.intermet.2011.07.007.

[38] A. Alés and F. Lanzini, “Mechanical and thermodynamical properties of β − Cu − Al − Mn alloys along the Cu3Al → Cu2AlMn compositional line,” *Solid State Commun*, vol. 319, p. 113980, 2020, doi: https://doi.org/10.1016/j.ssc.2020.113980.

[39] M. Şaşmaz, A. Bayri, and Y. Aydoğdu, “The Magnetic Behavior and Physical Characterization of Cu–Mn–Al Ferromagnetic Shape Memory Alloy,” *J Supercond Nov Magn*, vol. 24, no. 1, pp. 757–762, 2011, doi: 10.1007/s10948-010-0934-2.

[40] A. Alés, “Study of different structures derives of β−Cu3Al by means of ab-initio calculations and Quasi-Harmonic Approximation,” *Computational Condensed Matter*, vol. 31, p. e00652, 2022, doi: https://doi.org/10.1016/j.cocom.2022.e00652.

[41] R. Nityananda, P. Hohenberg, and W. Kohn, “Inhomogeneous electron gas,” *Resonance*, vol. 22, no. 8, pp. 809–811, 2017, doi: 10.1007/s12045-017-0529-3.

[42] W. Kohn and L. J. Sham, “Self-consistent equations including exchange and correlation effects,” *Physical Review*, vol. 140, no. 4A, pp. A1133–A1138, 1965, doi: 10.1103/PhysRev.140.A1133.

[43] S. J. Clark *et al.*, “First principles methods using CASTEP,” *Zeitschrift fur Kristallographie*, vol. 220, no. 5–6, pp. 567–570, 2005, doi: 10.1524/zkri.220.5.567.65075.

[44] S. Sugimoto *et al.*, “Giant magnetoresistance of Cu3Al-Cu2MnAl melt-spun ribbons,” *J Alloys Compd*, vol. 265, no. 1–2, pp. 273–280, 1998, doi: 10.1016/S0925-8388(97)00303-4.

[45] J. Soltys, “Order—disorder phase transitions in ternary alloys Cu3–xMnxAl,” *Physica Status Solidi (a)*, vol. 63, no. 2, pp. 401–406, 1981, doi: 10.1002/pssa.2210630204.

[46] H. H. Nguyen, M. T. Nguyen, W. J. Kim, and J. C. Kim, “Synthesis and analysis of nanocrystalline β1-Cu3Al and β2-NiAl intermetallic-reinforced aluminum matrix composite by high energy ball milling,” *Metals and Materials International*, vol. 23, no. 1, pp. 202–206, 2017, doi: 10.1007/s12540-017-6449-7.

[47] Y. Zhang, X. Yuan, X. Sun, B. C. Shih, P. Zhang, and W. Zhang, “Comparative study of structural and electronic properties of Cu-based multinary semiconductors,” *Phys Rev B Condens Matter Mater Phys*, vol. 84, no. 7, 2011, doi: 10.1103/PhysRevB.84.075127.

[48] H. S. Kim, M. Patel, P. Yadav, J. Kim, A. Sohn, and D. W. Kim, “Optical and electrical properties of Cu-based all oxide semi-transparent photodetector,” *Appl Phys Lett*, vol. 109, no. 10, pp. 1–6, 2016, doi: 10.1063/1.4961692.

[49] J. Gui *et al.*, “Embedded-atom method study of the effect of the order degree on the lattice parameters of Cu-based shape memory alloys,” *Journal of Physics: Condensed Matter*, vol. 6, no. 24, pp. 4601–4614, 1994, doi: 10.1088/0953-8984/6/24/019.

[50] H. Okumura, K. Sato, K. Suzuki, and T. Kotani, “Electronic Structure and Spin-wave Dispersion of Cu 2 MnAl, Ni 2 MnSn, and Pd 2 MnSn Based on Quasi-particle Self-consistent GW Calculations,” *J Physical Soc Japan*, vol. 89, no. 3, p. 034704, 2020, doi: 10.7566/jpsj.89.034704.

[51] A. Chatterjee, “First-principles investigation of the structural and electronic properties of Cu based intermetallics,” *10th Electronics Packaging Technology Conference, EPTC 2008*, no. 15, pp. 132–136, 2008, doi: 10.1109/EPTC.2008.4763423.

[52] M. Zou *et al.*, “First-Principles Investigation of Elasticity, Thermal and Electronic Properties of Intermetallics Formed at the Interface of Al-Cu Composites,” *J Electron Mater*, vol. 51, no. 7, pp. 3782–3797, 2022, doi: 10.1007/s11664-022-09612-9.

[53] Y. Z. Liu, B. C. Zheng, Y. X. Jian, L. Zhang, Y. L. Yi, and W. Li, “Anisotropic in elasticity, sound velocity and minimum thermal conductivity of Al–Cu intermetallic compounds,” *Intermetallics (Barking)*, vol. 124, p. 106880, 2020, doi: https://doi.org/10.1016/j.intermet.2020.106880.

[54] A. Szabo and N. S. Ostlund, *Modern Quantum Chemistry: Introduction to Advanced Electronic Structure Theory*, First. Mineola: Dover Publications, Inc., 1996.

[55] M. Born and J. R. Oppenheimer, “‘Zur Quantentheorie der Molekeln,’” *Ann Phys*, vol. 84, pp. 457–484, 1927.

[56] Monica Ţuţuianu, “Quantum mechanical modeling of surface reactions in storage catalytic converters,” Heidelberg, Univ., Diss., 2007, 2007. doi: 10.11588/heidok.00007477.

[57] R. G. Parr, “Density Functional Theory of Atoms and Molecules,” in *Horizons of Quantum Chemistry*, B. Fukui Kenichi and Pullman, Ed., Dordrecht: Springer Netherlands, 1980, pp. 5–15.

[58] P. Hohenberg and W. Kohn, “Inhomogeneous Electron Gas,” *Physical Review*, vol. 136, no. 3B, pp. B864–B871, Nov. 1964, doi: 10.1103/PhysRev.136.B864.

[59] J. P. Perdew *et al.*, “Atoms, molecules, solids, and surfaces: Applications of the generalized gradient approximation for exchange and correlation,” *Phys Rev B*, vol. 46, no. 11, pp. 6671–6687, Sep. 1992, doi: 10.1103/PhysRevB.46.6671.

[60] J. P. Perdew, K. Burke, and M. Ernzerhof, “Generalized gradient approximation made simple,” *Phys Rev Lett*, vol. 77, no. 18, pp. 3865–3868, 1996, doi: 10.1103/PhysRevLett.77.3865.

[61] B. Hammer, L. B. Hansen, and J. K. Nørskov, “Improved adsorption energetics within density-functional theory using revised Perdew-Burke-Ernzerhof functionals,” *Phys Rev B*, vol. 59, no. 11, pp. 7413–7421, Mar. 1999, doi: 10.1103/PhysRevB.59.7413.

[62] M. Segall, R. Shah, C. Pickard, and M. Payne, “Population analysis of plane-wave electronic structure calculations of bulk materials,” *Phys Rev B Condens Matter Mater Phys*, vol. 54, no. 23, pp. 16317–16320, 1996, doi: 10.1103/PhysRevB.54.16317.

[63] N. W. Ashcroft and N. D. Mermin, “Solid State Physics (Saunders College, Fort Worth, 1976),” *GD Mahan, Many-Particle Physics (Kuwer Academic, New York, 2000)*, 1976.

[64] M. C. Payne, M. P. Teter, D. C. Allan, T. A. Arias, and J. D. Joannopoulos, “Iterative minimization techniques for ab initio total-energy calculations: Molecular dynamics and conjugate gradients,” *Rev Mod Phys*, vol. 64, no. 4, pp. 1045–1097, Oct. 1992, doi: 10.1103/RevModPhys.64.1045.

[65] W. A. Harrison, *Electronic structure and the properties of solids: the physics of the chemical bond*. Courier Corporation, 2012.

[66] E. Karaca, “Hacim merkezli tetragonal yaplarda süperiletkenliğin yoğunluk fonksiyonel teorisi kullanlarak incelenmesi,” Sakarya Universitesi (Turkey), 2017.

[67] G. P. Srivastava, “The Physics of Phonons, Adam Hilger, Bristol 1990.,” *There is no corresponding record for this reference*, 1990.

[68] P. Pavone, “Lattice Dynamics of Semiconductors from Density-functional perturbation theory,” ISASPhd Thesis, ISASPhd Thesis, 1991.

[69] J. D. Pack and H. J. Monkhorst, “‘special points for Brillouin-zone integrations’-a reply,” *Phys Rev B*, vol. 16, no. 4, pp. 1748–1749, 1977, doi: 10.1103/PhysRevB.16.1748.

[70] R. S. Mulliken, “Electronic population analysis on LCAO-MO molecular wave functions. I,” *J Chem Phys*, vol. 23, no. 10, pp. 1833–1840, 1955, doi: 10.1063/1.1740588.

[71] A. S. Atalay, “The effects of chromium (Cr) and vanadium (V) substitutions on the material properties of AlFe2B2 MAB phase: An experimentally supported modelling study.,” PhD Thesis, Istanbul Technical University, Istanbul, 2024. Accessed: Mar. 21, 2025. [Online]. Available: https://akademi.itu.edu.tr/search-results?st=krom

[72] Md. M. Hossain, “First-principles study on the structural, elastic, electronic and optical properties of LiNbO3,” *Heliyon*, vol. 5, no. 4, p. e01436, 2019, doi: https://doi.org/10.1016/j.heliyon.2019.e01436.

[73] C. Gatti and P. Macchi, “A Guided Tour Through Modern Charge Density Analysis,” in *Modern Charge-Density Analysis*, C. Gatti and P. Macchi, Eds., Dordrecht: Springer Netherlands, 2012, pp. 1–78. doi: 10.1007/978-90-481-3836-4_1.

[74] Md. F. Rahman *et al.*, “A computational study of electronic, optical, and mechanical properties of novel Ba3SbI3 perovskite using DFT,” *Opt Quantum Electron*, vol. 56, no. 2, p. 206, 2023, doi: 10.1007/s11082-023-05738-0.

[75] R. J. D. Tilley, *Understanding solids: the science of materials*. John Wiley & Sons, 2004.

[76] M. Peng, R. Wang, Y. Wu, A. Yang, and Y. Duan, “Elastic anisotropies, thermal conductivities and tensile properties of MAX phases Zr2AlC and Zr2AlN: A first-principles calculation,” *Vacuum*, vol. 196, p. 110715, 2022, doi: https://doi.org/10.1016/j.vacuum.2021.110715.

[77] Sankalp Kota, Maxim Sokol, and Michel W Barsoum, “A progress report on the MAB phases: atomically laminated, ternary transition metal borides,” *International Materials Reviews*, vol. 65, no. 4, pp. 226–255, May 2020, doi: 10.1080/09506608.2019.1637090.

[78] M. Dikici, “Kristallerin Fiziksel Özellikleri,” *Ankara: Seçkin Yayıncılık*, 2014.

[79] F. Mouhat and F. X. Coudert, “Necessary and sufficient elastic stability conditions in various crystal systems,” *Phys Rev B Condens Matter Mater Phys*, vol. 90, no. 22, 2014, doi: 10.1103/PhysRevB.90.224104.

[80] M. Born, “On the stability of crystal lattices. I,” *Mathematical Proceedings of the Cambridge Philosophical Society*, vol. 36, no. 2, pp. 160–172, 1940, doi: 10.1017/S0305004100017138.

[81] M. Born and K. Huang, “Dynamical theory of crystal lattices Oxford University Press,” *London, New York*, pp. 160–173, 1954.

[82] J. Long, L. Yang, and X. Wei, “Lattice, elastic properties and Debye temperatures of ATiO3 (A=Ba, Ca, Pb, Sr) from first-principles,” *J Alloys Compd*, vol. 549, pp. 336–340, 2013, doi: https://doi.org/10.1016/j.jallcom.2012.08.120.

[83] F. D. Murnaghan, “The Compressibility of Media under Extreme Pressures,” *Proceedings of the National Academy of Sciences*, vol. 30, no. 9, pp. 244–247, 1944, doi: 10.1073/pnas.30.9.244.

[84] S. Yalameha, Z. Nourbakhsh, and D. Vashaee, “ElATools: A tool for analyzing anisotropic elastic properties of the 2D and 3D materials,” *Comput Phys Commun*, vol. 271, p. 108195, 2022, doi: https://doi.org/10.1016/j.cpc.2021.108195.

[85] R. Hill, “The Elastic Behaviour of a Crystalline Aggregate,” *Proceedings of the Physical Society. Section A*, vol. 65, no. 5, p. 349, 1952, doi: 10.1088/0370-1298/65/5/307.

[86] L. Sun, L. Miao, Y. Xu, Y. Cao, and S. Zhou, “First-principals research to mechanical, electronic, thermodynamic, and optical properties of Al–Cu intermetallics,” *Physica B Condens Matter*, vol. 689, p. 416163, 2024, doi: https://doi.org/10.1016/j.physb.2024.416163.

[87] R. Zhang, X. Gu, K. Zhang, X. Gao, C. Liu, and C. Chen, “Core Electron Count as a Versatile and Accurate New Descriptor for Sorting Mechanical Properties of Diverse Transition Metal Compounds,” *Advanced Materials*, vol. 35, no. 44, p. 2304729, Nov. 2023, doi: https://doi.org/10.1002/adma.202304729.

[88] Ş. Uğur, M. Güler, G. Uğur, and E. Güler, “Elastic, mechanical, optical and magnetic properties of Ru2MnX (X = Nb, Ta, V) Heusler alloys,” *J Magn Magn Mater*, vol. 523, p. 167614, 2021, doi: https://doi.org/10.1016/j.jmmm.2020.167614.

[89] A. S. Atalay, B. Derin, and M. F. Khanghah, “First-principles investigation of optical properties of AlFe(2-x)MxB2 (x= 0–1), (M= Cr, V) intermetallic compounds,” *Computational Condensed Matter*, vol. 32, p. e00731, 2022, doi: https://doi.org/10.1016/j.cocom.2022.e00731.

[90] D. Vanderbilt, “Soft self-consistent pseudopotentials in a generalized eigenvalue formalism,” *Phys Rev B*, vol. 41, no. 11, p. 7892, 1990, doi: 10.1103/PhysRevB.41.7892.

[91] B. G. Pfrommer, M. Côté, S. G. Louie, and M. L. Cohen, “Relaxation of Crystals with the Quasi-Newton Method,” *J Comput Phys*, vol. 131, no. 1, pp. 233–240, 1997, doi: 10.1006/jcph.1996.5612.

[92] L. D. LANDAU, A. I. AKHIEZER, and E. M. LIFSHITZ, “CHAPTER VI - THE THEORY OF SYMMETRY,” in *General Physics*, L. D. LANDAU, A. I. AKHIEZER, and E. M. LIFSHITZ, Eds., Oxford: Pergamon, 1967, pp. 115–143. doi: https://doi.org/10.1016/B978-0-08-009106-8.50009-1.

[93] C. Liu, F. Yun, and H. Morkoc, “Ferromagnetism of ZnO and GaN: a review,” *Journal of Materials Science: Materials in Electronics*, vol. 16, pp. 555–597, 2005.

[94] X. Zhou, H. Cao, Z. Zhou, J. Cao, and J. Yu, “Structural, electrical and optical properties of InGaZnO 4 and In 29Sn 3O 48 : a first-principles study,” *J Comput Electron*, vol. 16, no. 2, pp. 280–286, 2017, doi: 10.1007/s10825-017-0977-8.

[95] J. M. Vandenberg and R. A. Hamm, “An in situ X-ray study of phase formation in CuAl thin film couples,” *Thin Solid Films*, vol. 97, no. 4, pp. 313–323, 1982, doi: 10.1016/0040-6090(82)90523-5.

[96] B. Benichou, Z. Nabi, B. Bouabdallah, and H. Bouchenafa, “Structural, elastic, electronic and magnetic properties of quaternary Heusler alloy Cu2MnSi1-xAlx (x = 0 - 1): First-principles study,” *Revista Mexicana de Fisica*, vol. 64, no. 2, pp. 135–140, 2018, doi: 10.31349/revmexfis.64.135.

[97] K. Tanaka, T. Saito, and M. Yasuda, “Soft X-Ray Emission Spectra of Aluminium in β-Phase Cu-Ni-Al and Cu-Mn-Al Alloys,” 1983. doi: 10.1143/JPSJ.52.1718.

[98] A. S. Atalay and B. Derin, “Mechanical effects of Cr and V substitutions in AlFe2B2 by first-principles calculations,” *Comput Mater Sci*, vol. 239, p. 112960, 2024, doi: https://doi.org/10.1016/j.commatsci.2024.112960.

[99] Y. Zhang, Q. Li, and Y. He, “ReaxFF Molecular Dynamics Simulation of Hydrostatic and Uniaxial Compression of Nitrate Energetic Materials,” *ACS Omega*, vol. 5, no. 29, pp. 18535–18543, 2020, doi: 10.1021/acsomega.0c02829.

[100] F. Birch, “Finite elastic strain of cubic crystals,” *Physical Review*, vol. 71, no. 11, pp. 809–824, 1947, doi: 10.1103/PhysRev.71.809.

[101] S. Hayat, R. M. Arif Khalil, M. I. Hussain, A. M. Rana, and F. Hussain, "Ab-initio study of the structural, optoelectronic, magnetic, hydrogen storage properties and mechanical behavior of novel combinations of hydride perovskites LiXH3 (X = Cr, Fe, Co, & Zn) for hydrogen storage applications," *J Comput Electron*, vol. 20, no. 6, pp. 2284–2299, 2021, doi: 10.1007/s10825-021-01807-3.

[102] J. Jalilian, "Comment on 'study of electronic, magnetic, optical and elastic properties of Cu2MnAl a gapless full heusler compound,'" *J Alloys Compd*, vol. 626, pp. 277–279, 2015, doi: 10.1016/j.jallcom.2014.12.039.

[103] S. E. Kulkova, S. V. Eremeev, T. Kakeshita, S. S. Kulkov, and G. E. Rudenski, "The electronic structure and magnetic properties of full- And half-heusler alloys," *Mater Trans*, vol. 47, no. 3, pp. 599–606, 2006, doi: 10.2320/matertrans.47.599.

[104] Y. Tian, W. Zeng, Q. J. Liu, and Z. T. Liu, "Theoretical Study of the Structural, Electronic, Chemical Bonding and Optical Properties of the A21 am Orthorhombic SrBi2Ta2O9," *Brazilian Journal of Physics*, vol. 48, no. 1, pp. 25–30, 2018, doi: 10.1007/s13538-017-0544-6.

[105] M. Segall, R. Shah, C. Pickard, and M. Payne, "Population analysis of plane-wave electronic structure calculations of bulk materials," *Phys Rev B Condens Matter Mater Phys*, vol. 54, no. 23, pp. 16317–16320, 1996, doi: 10.1103/PhysRevB.54.16317.

[106] B. Caroli and A. Blandin, "Champs hyperfins dans les alliages d'heusler," *Journal of Physics and Chemistry of Solids*, vol. 27, no. 3, pp. 503–508, 1966, doi: https://doi.org/10.1016/0022-3697(66)90193-4.

[107] H. Takata, "Magnetic Form Factor of Cu2MnAl," *J Physical Soc Japan*, vol. 20, no. 9, pp. 1743–1744, Sep. 1965, doi: 10.1143/JPSJ.20.1743.

[108] G. P. Felcher, J. W. Cable, and M. K. Wilkinson, "The magnetic moment distribution in Cu2MnAl," *Journal of Physics and Chemistry of Solids*, vol. 24, no. 12, pp. 1663–1665, 1963, doi: 10.1016/0022-3697(63)90112-4.

[109] K. Tajima, Y. Ishikawa, P. J. Webster, M. W. Stringfellow, D. Tocchetti, and K. R. A. Zeabeck, "Spin Waves in a Heusler Alloy Cu2MnAl*," *J Physical Soc Japan*, vol. 43, no. 2, pp. 483–489, Aug. 1977, doi: 10.1143/JPSJ.43.483.

[110] Y. Kurtulus, M. Gilleben, and R. Dronskowski, "Electronic structure, chemical bonding, and finite-temperature magnetic properties of full heusler alloys," *J Comput Chem*, vol. 27, no. 1, pp. 90–102, 2006, doi: 10.1002/jcc.20308.

[111] R. Cheng and X. Y. Wu, "Structural stability and electronic properties of AlCu3, AlCu2zr and AlZr3," *Materiali in Tehnologije*, vol. 47, no. 1, pp. 65–69, 2013.

[112] S. Xu, Y. Duan, M. Peng, and L. Shen, "Effects of Vacancies on the Structural, Elastic, Electronic and Thermodynamic Properties of C11b-VSi2 by First-Principles Calculations," *Metals (Basel)*, vol. 12, no. 10, 2022, doi: 10.3390/met12101625.

[113] K. Wang *et al.*, “First-principles investigations on the electronic structures, polycrystalline elastic properties, ideal strengths and elastic anisotropy of U3Si2,” *The European Physical Journal Plus*, vol. 136, no. 4, p. 409, 2021, doi: 10.1140/epjp/s13360-021-01347-6.

[114] M. Rougab and A. Gueddouh, “First-principles insights into structural stability, elastic anisotropies, mechanical and thermodynamic properties of the Hf2GeX (X=C, N, and B) 211 MAX phases,” *Journal of Physics and Chemistry of Solids*, vol. 176, p. 111251, 2023, doi: https://doi.org/10.1016/j.jpcs.2023.111251.

APPENDICES

APPENDIX A. Figures

3D illustration of Directional dependencies

Elastic Anisotropy of Compressibility Modulus (β, the inverse of the Bulk modulus)

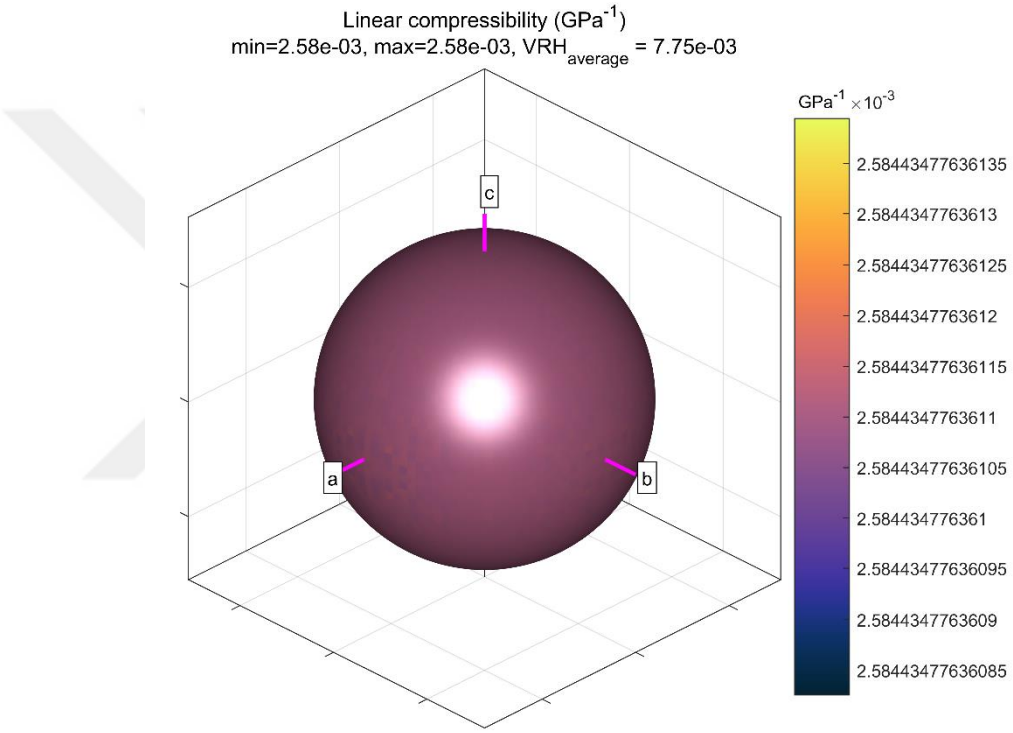

Figure A.1. Three-dimensional direction-dependent compressibility modulus of the $L1_2$ type structure.

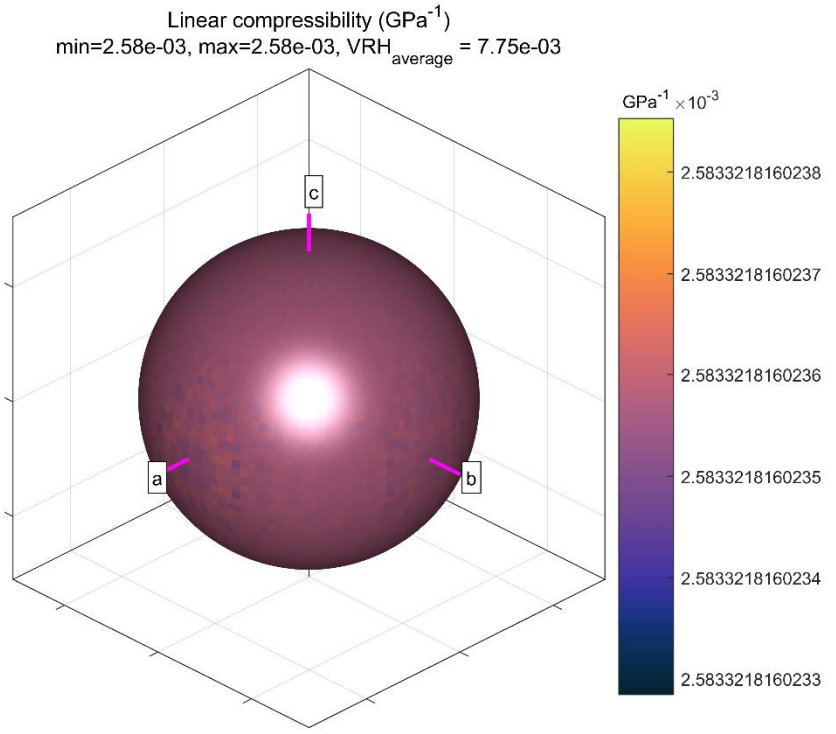

Figure A.2. Three-dimensional direction-dependent compressibility modulus of the $D0_3$ type structure.

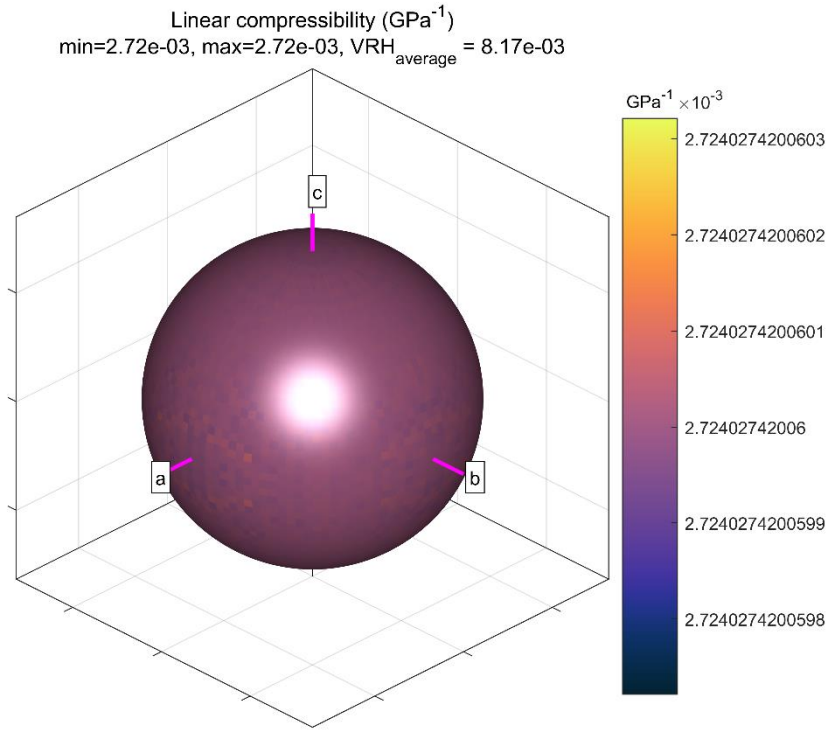

Figure A.3. Three-dimensional direction-dependent compressibility modulus of the $L2_1$ type structure.

Elastic Anisotropy of Shear Modulus

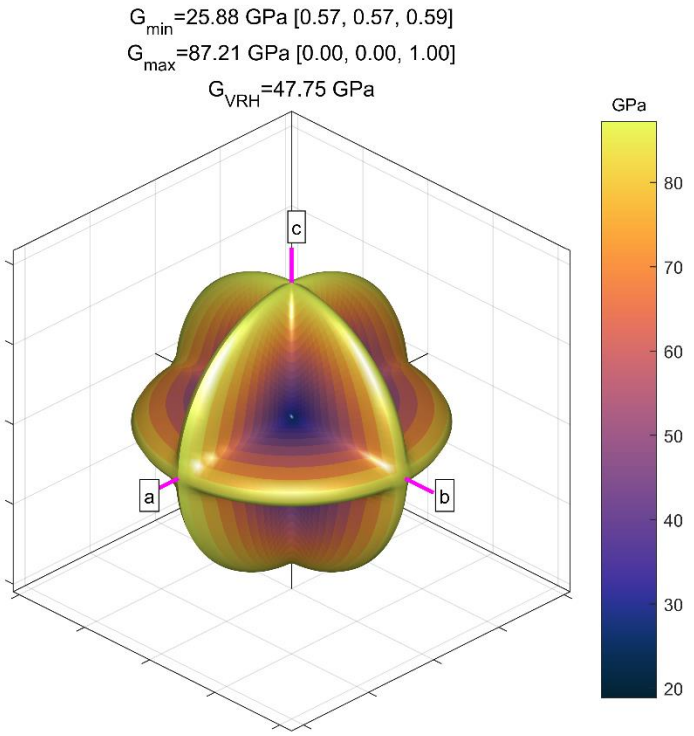

Figure A.4. Three-dimensional direction-dependent shear modulus of the $L1_2$ type structure.

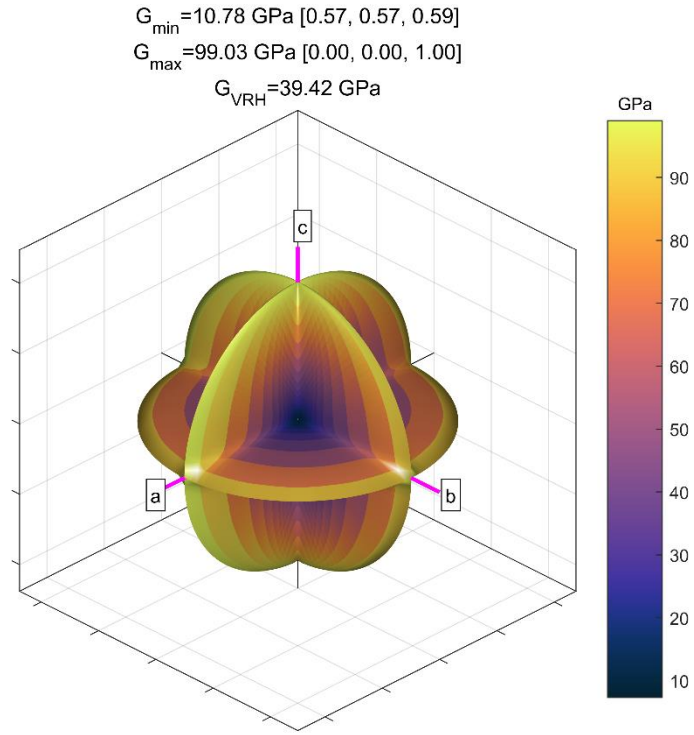

Figure A.5. Three-dimensional direction-dependent shear modulus of the $D0_3$ type structure.

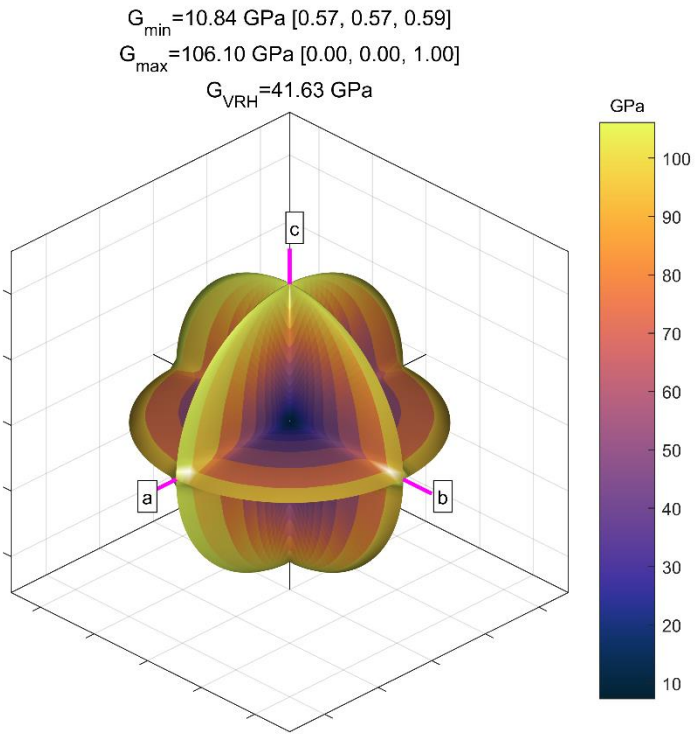

Figure A.6. Three-dimensional direction-dependent Compressibility modulus of the $L2_1$ type structure.

Elastic Anisotropy of Poisson Ratio

Materials with a Poisson ratio between -1 and 0.5 are generally relatively stable against shear deformation [112]. For covalently bonded materials the Poisson ratio is ν = 0.1 and for ionic bonded materials ν is approximately 0.25, while for metallic bonded materials ν usually ranges from 0.25 to 0.45 [71], [113]. The Poisson ratio can also be used to classify materials in terms of ductility or brittleness: a value of ν greater than 0.26 indicates that the material is ductile, whereas the opposite is brittle [71], [114].

The Poisson ratio can be used for flexibility. If the Poisson ratio of the material is V>1/3, the material can behave as flexible, and if V<1/3, it can behave as brittle . The Poisson ratio (v) = 0.25 and (v) = 0.5 values are the lower and upper limits of the force at the center of the solids[113] .

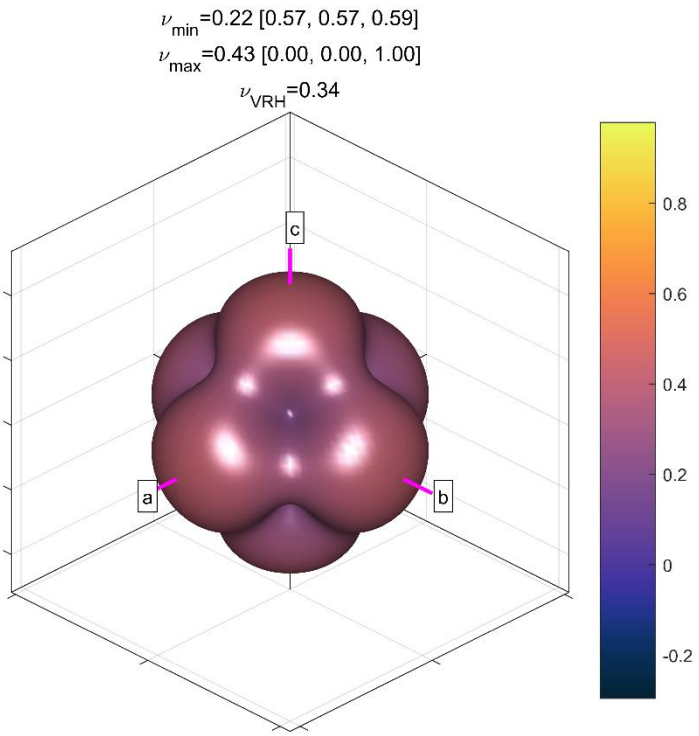

Figure A.7. Three-dimensional direction-dependent shear modulus of the $L1_2$ type structure.

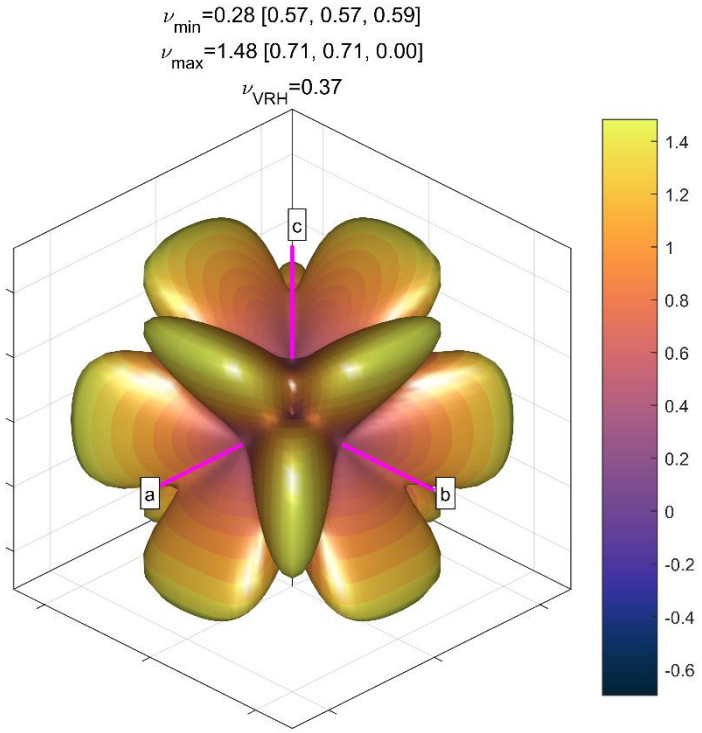

Figure A.8. Three-dimensional direction-dependent shear modulus of the $D0_3$ type structure.

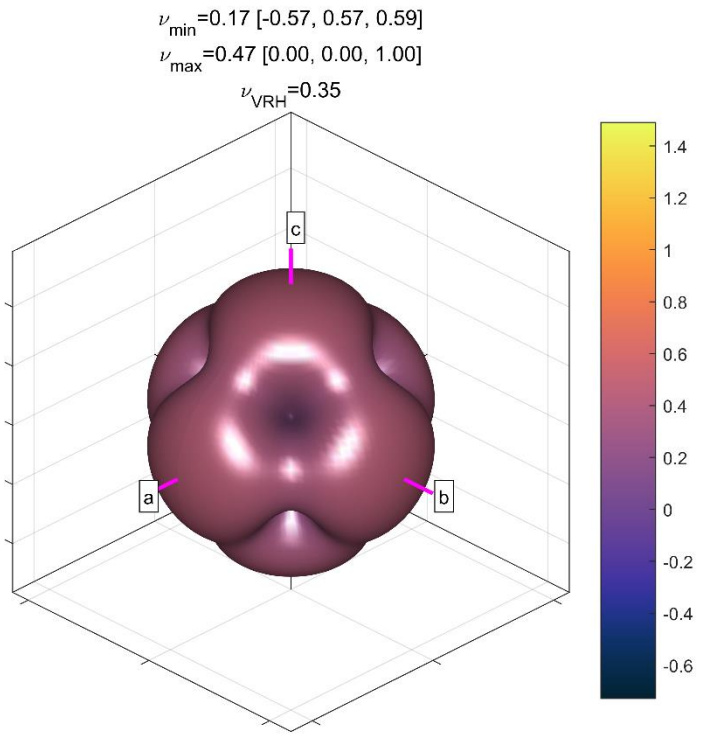

Figure A.9. Three-dimensional direction-dependent Poisson ratio of the $L2_1$ type structure.

From APPENDIX figures the anisotropic degree of $L2_1$ is higher than other types of structures. Anisotropic degree of $L2_1$ greater than $D0_3$ and $D0_3$ greater than $L1_2$ in all crystal type structure of $Cu_{(3-x)}Mn_xAl$ (x = 0, 1) intermetallic compound.

CURRICULUM VITAE

Name Surname : Marefat FEIZI KHANGHAH

EDUCATION:

- **Undergraduate** (B.Sc) : 2010, Tohid University, Faculty of Engineering, Electronic Eng.
- **Graduate** (M.Sc) : 2014, Ataturk University, Institute of Nature science, Department of Nanoscience and Nanoengineering

AWARDS AND PROFESSIONAL EXPERIENCE:

- He worked as a Turkish Teacher at the sevral education Center between 2009-2017.
- He is still working as a Official Turkish Translator at the Pashazadeh Translation Center since 2019.
- He has also been serving as an Attaché at the Ministry of Foreign Affairs since 2020.

ARTICLES PUBLICATIONS, PATENTS AND PRESENTATIONS ON THE THESIS:

- Khanghah M.F., Kurnaz S. C. 2025. First principles investigation of structural and electronic properties and spin polarizability of $Cu_{(3-x)}Mn_xAl$ (X = 0, 1) intermetallic compounds, *Archives of Metallurgy and Materials*, 48(17), 5195-5220. 10.24425/amm.2025.152569

OTHER PUBLICATIONS, PRESENTATIONS AND PATENTS:

- A. S. Atalay, B. Derin, and M. F. Khanghah, "First-principles investigation of optical properties of $AlFe_{(2-x)}M_xB_2$ (x= 0–1), (M= Cr, V) intermetallic compounds," *Computational Condensed Matter*, vol. 32, p. e00731, 2022, doi: https://doi.org/10.1016/j.cocom.2022.e00731.